

Efficient syntheses of functional inorganic materials by interzeolite conversion method

(ゼオライト転換法による機能性無機物質の効率的な合成)

Koutaro Honda

Submitted to Hiroshima University

In partial fulfillment of the requirements for the degree of
Philosophy of Doctor

Supervisor: Professor Dr. Tsuneji Sano

Department of Applied Chemistry,
Graduate School of Engineering,
Hiroshima University

March 2015

Referee in Chief: Professor Tsuneji Sano

Referees: Professor Takeshi Shiono

Professor Kikuo Okuyama

Associate Professor Masahiro Sadakane

Department of Applied Chemistry,
Graduate School of Engineering,
Hiroshima University

Contents

Chapter 1: Introduction

1. Introduction to zeolite.....	1
2. Zeolite synthesis.....	6
2.1 History of zeolite synthesis.....	6
2.2 Zeolite synthesis with and without organic structure-directing agents (OSDAs).....	9
2.3 Conversion of one zeolite into another.....	13
3. Introduction to layer silicate.....	17
3.1 Layer silicate.....	17
3.2 Zeolitic layer silicate.....	20
3.3 Layer structure as transients and precursors.....	22
4. Application of zeolite.....	26
5. Overview of the thesis.....	29
References.....	31

Chapter 2: Influence of seeding on FAU-*BEA interzeolite conversion

1. Introduction.....	37
2. Experimental.....	39
2.1 Synthesis.....	39
2.2 Characterization.....	40
3 Results and discussion.....	41
3.1 Influence of addition of seed crystals on FAU-*BEA interzeolite conversion in the presence of TEAOH.....	41
3.2 Influence of OSDAs on FAU-*BEA interzeolite conversion in the presence of seed crystals.....	46
3.3 OSDA-free synthesis of *BEA zeolite from FAU zeolite.....	51
4 Conclusions.....	56
References.....	58

Chapter 3: Hydrothermal conversion of FAU zeolite into LEV zeolite in the presence of non-calcined seed crystals

1. Introduction.....	60
2 Experimental.....	62
2.1 Synthesis of LEV zeolite.....	62
2.2 Characterization.....	63
3 Results and discussion.....	64
4. Conclusions.....	74
References.....	76

Chapter 4: Hydrothermal conversion of FAU and *BEA zeolites into MAZ zeolites in the presence of non-calcined seed crystals

1. Introduction.....	78
2. Experimental.....	81
2.1 Preparation of starting zeolites and MAZ seed crystals.....	81
2.2 OSDA-free synthesis of MAZ zeolite in the presence of non-calcined seed crystals.....	82
2.3 Characterization.....	83
3. Result and discussion.....	84
3.1 Preparation and characterization of starting zeolites and seed crystals.....	84
3.2 OSDA-free synthesis of MAZ zeolite from FAU zeolite.....	84
3.3 OSDA-free synthesis of MAZ zeolite from *BEA and MFI zeolites.....	93
4. Conclusions.....	97
References.....	98

Chapter 5: Role of structural similarity between starting zeolite and product zeolite in the interzeolite conversion process	
1. Introduction.....	100
2. Experimental.....	103
2.1. Hydrothermal conversion of FAU- and *BEA zeolites.....	103
2.2 Characterization.....	103
3. Result and discussion.....	104
3.1 Hydrothermal conversion of FAU zeolite in the presence of alkaline metal cations.....	104
3.2 Hydrothermal conversion of *BEA zeolite in the presence of alkaline metal cations.....	107
3.3 *BEA–MFI interzeolite conversion.....	109
4. Conclusions.....	114
References.....	116
Chapter 6: Transformation of LEV zeolite into less dense CHA zeolite	
1. Introduction.....	118
2. Experimental.....	121
2.1 Synthesis of starting LEV.....	121
2.2 Hydrothermal conversion of LEV to CHA.....	121
2.3 Characterization.....	122
3. Result and discussion.....	123
3.1 Transformation of LEV into CHA.....	123
3.2 Effects of NaOH/SiO ₂ and H ₂ O/SiO ₂ ratios on transformation of LEV —Comparison with amorphous materials.....	129
4. Conclusions.....	131
References.....	133
Chapter 7: Synthesis and crystal structure of a layered silicate HUS-1 with a halved sodalite-cage topology	
1. Introduction.....	135
2. Experimental.....	138
2.1 Synthesis of HUS-1.....	138
2.2 Physicochemical analysis.....	139
2.3 Structural analysis.....	140
3. Result and discussion.....	143
3.1 XRPD, SEM, and TG-DTA analysis.....	143
3.2 Solid-State NMR.....	146
3.3 Structural Analysis.....	150
3.4 Structural comparison of HUS-1 and β-HLS.....	155
4. Conclusions.....	158
References.....	159

Chapter 8: An efficient way to synthesize Hiroshima University Silicate-1 (HUS-1) and the selective adsorption property of Ni²⁺ from seawater	
1. Introduction.....	163
2. Experimental.....	165
2.1 Synthesis of HUS-1.....	165
2.2 Preparation of Other Adsorbents.....	166
2.3 Preparation of seawater-mimicking mixed electrolyte Solution.....	166
2.4 Adsorption tests.....	166
2.5 Characterization.....	167
3. Result and discussion.....	168
3.1 Synthesis of HUS-1.....	168
3.2 Concentration of Ni ²⁺	173
4. Conclusions.....	178
References.....	180
 Chapter 9: Summary	 183
 List of publications	 192
Presentations in international conference	193
Acknowledgements	194

Chapter 1

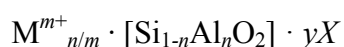
Introduction

1. Introduction to zeolite

Many zeolites with different structures and compositions are commercially available. The zeolitic micropores are of molecular size, which give them adsorption, catalytic and ion exchange properties. These features are very important in both the chemical industrial field and the new applications related to process intensification, green chemistry, hybrid materials, medicine, cosmetic, animal food uses, optical and electrical materials, reaction and sensing microsystems, and nanotechnology. There have been considerable academic and industrial research efforts carried out in the field of zeolite so far.

Strictly defined, zeolites are crystalline aluminosilicates having microporous ($2.0 \text{ nm} \geq d_p$) with tetrahedrally-connected framework structure based on corner-sharing TO_4 tetrahedra ($T = \text{Si}, \text{Al}$). For a completely siliceous structure, combination of TO_4 units in this fashion leads to silica (SiO_2), which is an uncharged solid. To substitute Si^{4+} to Al^{3+} in the pure silica frameworks gives an overall negative charge to the framework. This is balanced by the presence of extra-framework charge-balancing cations located within the pore space, coordinated to framework O atoms, which is also able to take in neutral atoms and molecules small enough to enter via the pore windows.

A simplified empirical formula for an aluminosilicate zeolite is



where n can vary from 0–0.5 and M represents extraframework inorganic or organic

cations. In the as-made zeolites they are typically alkali or alkali earth metal cations or alkylammonium cations. The extraframework cations are ion exchangeable and give rise to the rich ion-exchange chemistry of these materials. X represents neutral guest molecules or included species such as H₂O. The novelty of zeolites arises from their microporosity and is a result of the topology of the framework.

The primary building blocks of the framework are the tetrahedral. Typically, Al–O and Si–O bond distances are 1.73 and 1.61 Å, respectively, with O–T–O angles close to the tetrahedral angle, 109.4°. There is more variation in the Si–O–Si bond angles between tetrahedral, where the average angle is 154° with a range of 135–180° and a mode of 148° [1]. Variation of T–O–T angles enables a wide diversity of frameworks to exist.

The amount of Al within the framework can vary over a wide range, with Si/Al = 1 to ∞, the completely siliceous form being polymorphs of SiO₂. Löwenstein proposed that the lower limit of Si/Al = 1 of a zeolite framework arises i.e. Al–O–Al linkages are not observed in hydrothermally-synthesized zeolite, because the negative charge associated with aluminate tetrahedra interact unfavorably, an observation expressed as Löwenstein's rule. The framework composition depends on the synthesis conditions. Post-synthesis modifications that insert/remove Si or Al into the framework have also been searched well. By increasing the Si/Al ratio of the framework, the hydrophobicity and the hydrothermal stability rise.

Typically, in as-synthesized zeolites, water molecules are present in the internal voids of zeolite. The sorbed phase and organic non-framework cations can be removed by thermal treatment/oxidation, making the intracrystalline space available. The crystalline nature of the framework ensures that the pore openings are uniform throughout the crystal and can readily discriminate against molecules with dimensional differences less

than 1 Å, giving rise to the name molecular sieves.

Although aluminosilicate zeolites are by far the best studied and most widely applied materials that have tetrahedrally-coordinated porous frameworks, many compositional variants (including pure silica forms) have been prepared, and some 20 elements have been reported to be included via substitution into framework cation sites. These can be aliovalent, with a different valency from silicon or isovalent. The inclusion of some elements has stronger effects on chemical characteristics than on structural features whereas the inclusion of high levels of elements such as Ga or Ge can result in the crystallization of frameworks with distinctly different structural features. In their ease of substitution, stability in the tetrahedral site and structure directing properties depend on cationic radius and electron negatively.

Since the first description of hydrothermal synthesis of zeolites was achieved in the laboratory by Barrer in 1940s, the scientific and industrial interest in the field increased [2]. A large number (218) of different structures for tetrahedral frameworks of all compositions have been discovered since 1940s [3]. The Structure Commission of the International Zeolite Association identifies each framework with a three-letter mnemonic code (e.g. LTA for Linde zeolite A, MFI for ZSM-5, etc.) [3]. Figure 1-1 shows the framework projections for commonly studied zeolites.

Figure 1-2 shows structures of four selected zeolites from top to bottom: zeolites X/Y (FAU), ZSM-12 (MTW), ZSM-5 (MFI), and Theta-1 (TON). In these commonly used representations, the T-atoms are located at the vertices, and the lines connecting them stand for T–O–T bonds. For example, if 24 tetrahedra are linked together as shown in the top line of Figure 1-2, the cubo-octahedron, also referred to as a sodalite unit or β -cage, results. It is important to derive zeolite structures with secondary building units (SBU).

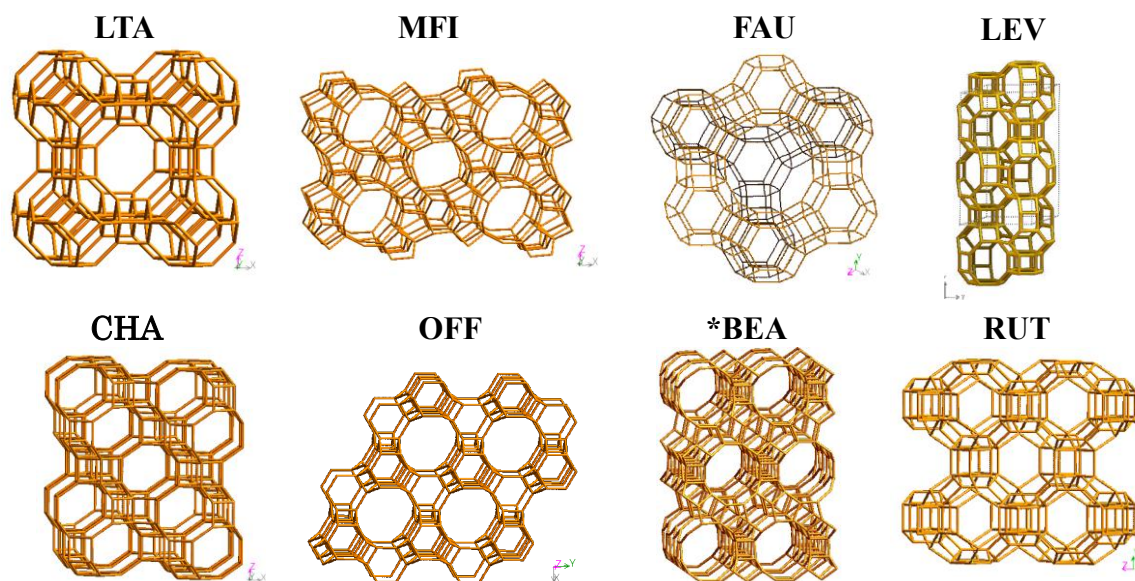


Fig. 1-1 Various framework structures of the zeolites.

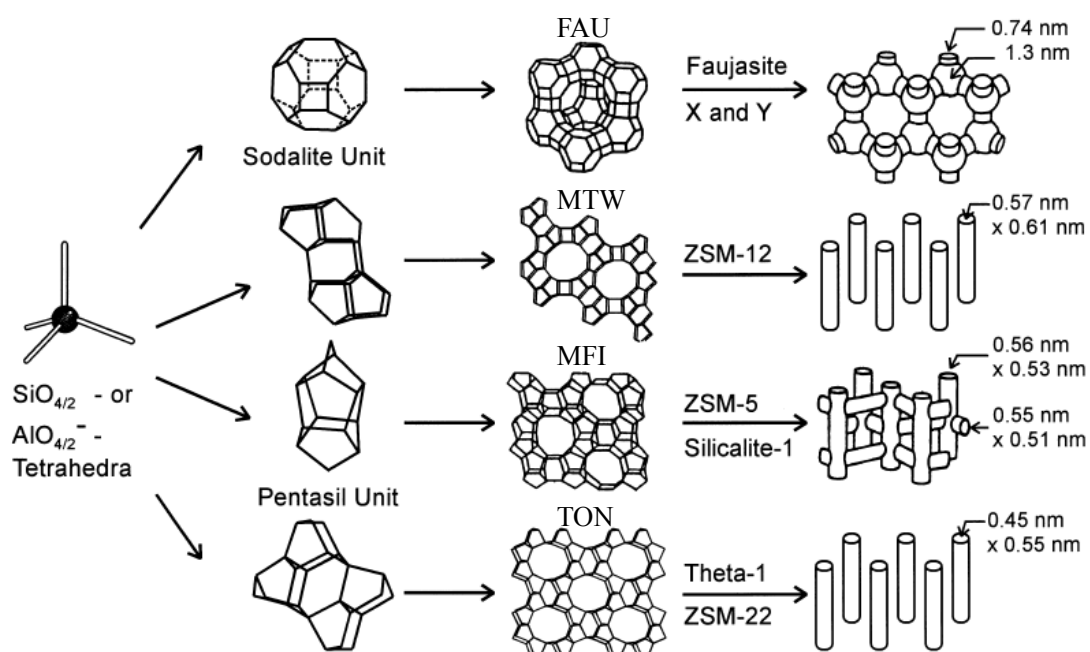


Fig. 1-2 Structures of four selected zeolites from top to bottom: faujasite or zeolites X, Y (FAU); ZSM-12 (MTW); ZSM-5 or silicalite-1 (MFI); Theta-1 or ZSM-22 (TON) and their micropore systems and dimensions [4]. In a less cluttered representation, the oxygen atoms are omitted and straight lines are drawn connecting the T atoms.

As shown in Figure 1-3, the structure of the mineral sodalite consists of β -cages face sharing six-membered rings (6MRs). Instead, if they linked through their 4MRs via double four-membered ring (D4R) units, the zeolite A framework results (topology type

LTA). Sodalite cage can also be linked through D6Rs on their 6MR faces. Whereas there is only one way of arranging the cages for sodalite and zeolite A, there are different ways of linking layers of sodalite cages through D6Rs. The two end member variants are cubic zeolites with the faujasite (FAU) structure type, where FAU refers to the mineral form of this material, faujasite, and its hexagonal polytype EMC-2 (structure type EMT).

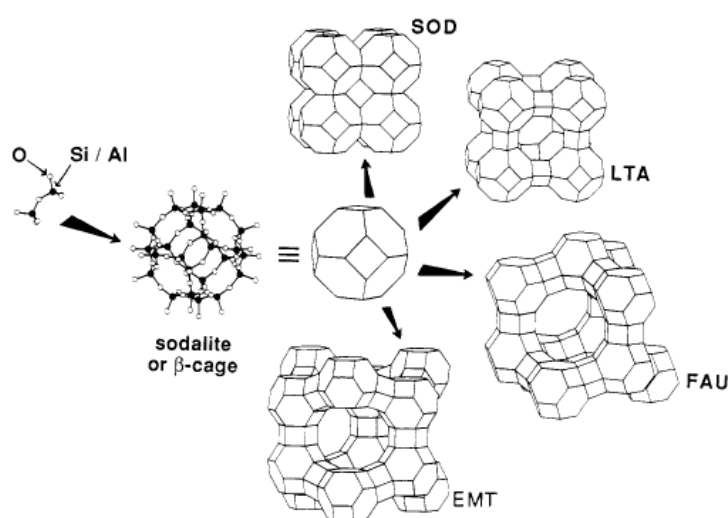


Fig. 1-3 The construction of four different zeolite frameworks with sodalite or β cages. A pair of TO_4 tetrahedra is linked to a single sodalite cage by T-O-T bonds. The sodalite cage unit is found in SOD, LTA, FAU, and EMT frameworks [5].

There is no doubt of the great importance of zeolites in the general subject of materials science. Zeolites, and in a broader sense zeolitic materials, are today studied and applied in many different ways and fields, even though some of their essential features are not wholly understood, and many challenges remain for the now and future.

2. Zeolite synthesis

2.1 History of zeolite synthesis

The history of man-made zeolites can be traced back to the claimed laboratory preparation of levynite by St Claire Deville in 1862 [6]. However, zeolite synthesis as we know it today had its origins in the work of Barrer, commencing in 1940s [2]. Barrer began his work by investigating the conversion of known mineral phases under the action of strong salt solutions at fairly high temperatures (170–270 °C). Obtained KFI zeolite displayed unique characteristics and represented the first synthetic zeolite [7-10] determined subsequently for zeolite ZK-5 [11,12]. Milton pioneered the use of more reactive starting materials (freshly precipitated aluminosilicate gels), enabling reactions to be carried out under milder conditions and leading to the discovery of zeolite A [13] and X [14]. By 1953, Milton and his colleagues had synthesized 20 zeolites, including 14 unknown as natural minerals [15]. These zeolites, prepared using inorganic cations, tend then to have relatively high Al contents, because their pore space contains many exchangeable cations.

Above-mentioned syntheses were conducted only in the presence of inorganic cations. Using organic cations such as quaternary ammonium cations to obtain new structure types became common following pioneering work in 1961 by Barrer et al. [16-18]. The introduction of organic constituents was to have a major impact upon zeolite synthesis. Among the most important new structure types prepared with tetraethyl- and tetrapropylammonium cations were Beta and ZSM-5, respectively. [19,20]. More recently, these organic constituents have been called organic structure-directing agents (OSDA). They can be bulky, so fewer can be included in the zeolite pores than would be the case for inorganic cations. This necessitates a lower density of framework negative

charge and consequently a lower Al content.

There has subsequently been a large rise in the number of known synthetic zeolite and also the discovery of new families of zeolite-like or zeolite-related materials [21].

The discovery of aluminophosphate (AIPO) zeotype by UOP in 1982 heralded a major expansion of the compositional range of this type of microporous solid [22]. They can be thought of as derived from pure silica zeolites by the ordered substitution Al and P to 2Si, is that their framework composition is AlPO_4 and Al and P show strict alternation in tetrahedral framework sites. There are strong similarities between AIPO zeotypes and zeolites in their structure and a more importantly, in chemistry. The most obvious structure difference is that the strict alternation of Al and P in framework sites rules out the presence of odd numbered rings in AIPO structure. VPI-5 is the 18MR AIPO, this framework structure observed in only AIPO structure [23]. Silicoaluminophosphates (SAPOs) are derived from AIPOs by two mechanisms. In the first, P is replaced by Si, leaving a net negative charge on the framework that is charge-balanced by a proton after template removal ($\text{H}_x\text{AlP}_{1-x}\text{Si}_x\text{O}_4$). This bridging hydroxyl Si–OH–Al is usually less strongly acidic than those found in the H^+ form of aluminosilicate zeolites. The second mechanism of substitution involves the coupled replacement of Al and P by two Si atoms. This cannot happen in isolation, due to the unfavorability of Si surrounded by nearest neighbor P atoms, but can be considered to occur when direct Si–P substitution has resulted in the formation of Si–O–P linkage. This second type of substitution results in the formation of aluminosilicate islands.

These isovalent substitutions are of importance in zeotypic silicates of Ti^{4+} and Ge^{4+} . The titanosilicates is primarily of significance for their catalytic properties whereas germanosilicates are remarkable for the novel topologies they exhibit.

Titanium-containing high silica zeotypes such as TS-1 [24] contain a few mole percent of Ti in framework cation sites. Although the Ti is tetrahedral in the template-free, dehydrated form, it readily acts as a Lewis acid to expand its coordination sphere in the presence of water of, with important application in selective oxidation, peroxide species. Other zeotypic titanosilicates have been reported including the large pore Ti- β [25] and Ti-Y [26]. The inclusion of germanium in silicates has resulted in the crystallization of remarkable zeotypic structures including ITQ-17, IM-12, and ITQ-33 [27–29]. The fully tetrahedral frameworks of these structures are characterized by D4R units, 3MRs and even D3Rs, giving rise to framework with low tetrahedral site densities and large pores. The tendency for the inclusion of germanium in tetrahedral sites to favor the formation of small ring SBUs is attributed to the larger non-bonding radius of Ge vs. Si and consequently the ability to form smaller O–T–O angles that stabilize 3MRs and 4MRs.

Investigative work aimed at gaining an understanding of the synthesis mysterious process has its origins in the 1960s. These studies have continued up to the present day, spurred on at various points by discoveries of new materials, advances in synthetic techniques, innovations in theoretical modeling methods and, especially, by the development of new techniques for the investigation of reaction mechanisms and characterization of products.

2.2 Zeolite synthesis with and without organic structure-directing agents (OSDAs).

The first synthesis of zeolites was started in alkaline media. It crystallized as aluminum-rich zeolites ($\text{Si}/\text{Al} = \text{close to } 1$) due to the presence of large amount of extra-framework alkali-metal cations. Nevertheless, in 1961, the OSDA is introduced for the first time in zeolite synthesis by Barrer et al. [16]. The use of tetraalkylammonium cations allowed increasing the framework Si/Al ratio, determined by the OSDA incorporated into the zeolite. As it can be seen in Figure 1-4 [5], less positive charges are introduced by the organic molecule than by the small inorganic cations in the SOD cage, requiring less anionic charges in the zeolite framework. Therefore, the organic molecule can determine the amount of trivalent elements in the zeolite framework, but also the structural characteristics, such as pore dimensions and cavities, depending in shape, size, hydrophobicity, and number of charges of the OSDA molecule.

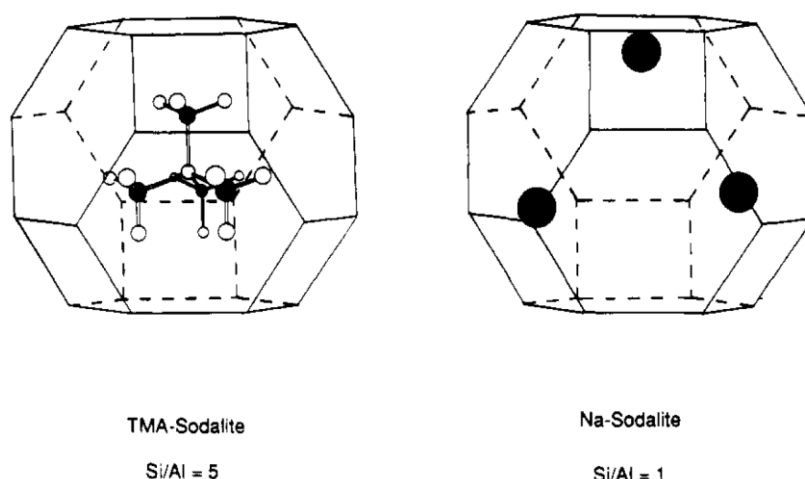


Fig. 1-4 Scheme of tetramethylammonium cation (left) or sodium cations (right) into the sodalite cage [5].

Amines and quaternary ammonium ions are the most frequently used OSDA in zeolite synthesis. The OSDA increases the thermodynamic stability in the organic-inorganic system during the nucleation step, by means of interactions with the zeolitic framework. There are no covalent bonds between organic and inorganic in this composite, but the assembly process occurs by weak interactions such as van der Waals forces, showing the structural directing effect [30]. The ideal correlation between the shape and size of the OSDA and the framework cavity is known as “template” effect. Two excellent examples of template structure-direction are the synthesis of ZSM-18 using tris(quaternary ammonium) cation as OSDA [31], and MCM-61 synthesis using the 18-Crown-6 molecule [32]. The relationship between OSDA properties and the characteristics of cages and pores of formed zeolites have been studied [33]. Gies and Marler found that sixty-one molecules can be used to control the structure of the clathrasils. They showed that large molecules direct the formation of clathrasils with large cages, while small molecules direct the crystallization of clathrasils with small cages [34]. Moreover, Nakagawa and Zones increased the size of the structure-directing agent, showing that when the size of the OSDA is increased, the product selectivity changes from a clathrasil to a microporous, large-pore zeolite. Furthermore, if the geometry is changed from cyclic to linear molecules, there is a transition from clathrasils to microporous molecular sieve with 10-ring pores, and the evolution from linear to branched organic molecule allows getting three-dimensional 10-ring (MFI) instead of one-dimensional 10-ring (ZSM-48) [33,35]. In general, the selectivity of the OSDA towards a zeolite is correlated with the size of molecule. If the number of carbon and nitrogen atoms in the structure-directing molecule increases, the quantity of structures obtained is reduced [33], therefore, the specificity as “template” increases

when it evolves from small and flexible to large and rigid molecules. The synthesis of extra-large pore zeolites (pores with more than 12 T atoms) is highly desired in catalysis for their potential application in the reactivity of large molecules. The use of relatively large and rigid OSDAs was thought to be the adequate strategy to synthesize extra-large pore zeolites. Following this methodology, some extra-large pore zeolites with 14 MR openings were synthesized, UTD-1, CIT-5, SSZ-53, and SSZ-59 [36–39].

A new molecular sieve, ITQ-37, has been described in 2009 showing a chiral extra-large framework [40]. For the preparation of this zeolite, an organic molecule with four chiral centers has been used (Figure 1-5). However, in this case, the enormous helical channels are achieved by the presence of connectivity defects in the structure, and therefore the “true organic-template effect” cannot be claimed. There is an example in the investigation towards the design of chiral molecular sieve. The scientists have to increase the efforts in the preparation of this type of solids by their enormous potential impact fields, as chemistry, pharmacy, and biology.

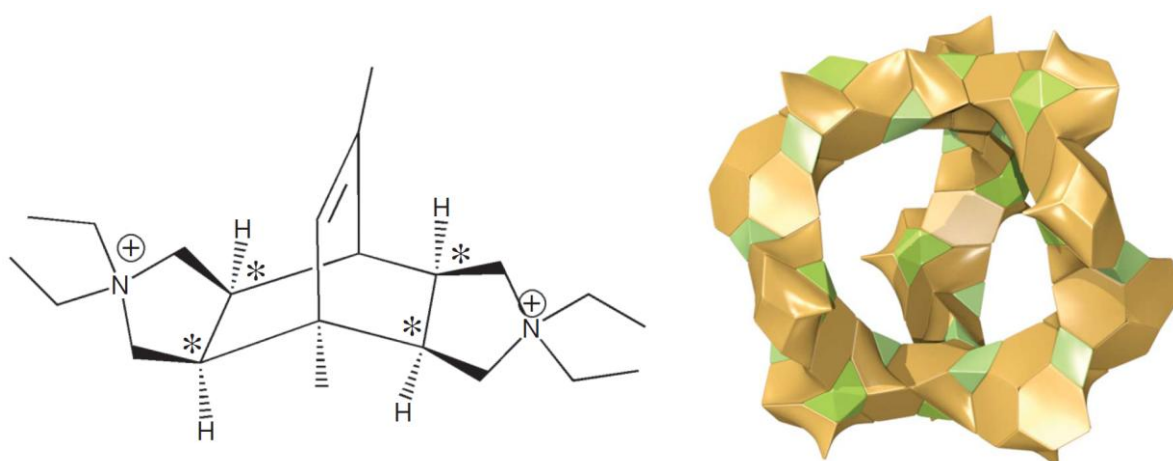


Fig. 1-5 (Left) OSDA used for the ITQ-37 zeolite showing four chiral centers (asterisks), (right) chiral structure of the ITQ-37 [40].

As described above, using OSDAs on a zeolite synthesis is interesting. Zeolites that are synthesized with using OSDAs have unique characteristics such as high $\text{SiO}_2/\text{Al}_2\text{O}_3$ ratio, extra-large pore, and are sometimes novel zeolites. But OSDAs are very costly, because they are synthesized by complex process. So, obtained zeolites are costly too. Additionally, OSDAs have to be removed from within zeolite pores by calcination. There are some problem such as the consumption of energy and emission of harmful gases. Therefore, OSDAs-free synthesis is desired. Recently, the seed-assisted OSDAs-free syntheses have been reported by several groups.

The seed-adding method was known in the late 1960s. The seed crystal of the same target type zeolite is adding into the raw material mixture gel to shorten the crystallization time [41–43], improve the phase selectivity [41–44] and control the particle size [45]. The seed crystal provides the reaction field with crystal surface for the crystal growth. If the crystal surface can incorporate the growing species sufficiently, the obtainable product comes from the seed crystal zeolite. By applying this phenomenon, the synthesis of zeolites without OSDAs has been studied by several groups. Xiao et al. succeeded in seed-assisted OSDAs-free synthesis of *BEA zeolite in 2008[46]. All over the world researchers hurried up and studied the repeatability and the mechanism of the seed-assisted OSDAs-free synthesis. Mintova et al. reported that the repeatability was improved by using non-calcined seeds in place of calcined seeds [47]. In a few years, Okubo et al. reported the hypothesis that the key factor in the successful synthesis of zeolites in the absence of OSDAs was the common composite building unit contained both in the seeds and in the zeolite obtained from the gel after heating without seeds [48].

2.3 Conversion of one zeolite into another

Just as lamellar phases are sometimes transiently observed during the course of zeolite preparations, the formation of one zeolite phase may be preceded by another. In early work on the synthesis of ZSM-5, Erdem and Sand observed the intermediate appearance of mordenite and analcime during the synthesis of Na, TPA-ZSM-5 as the TPA/Na ratio was lowered [49]. For the TPA, K system, metastable harmotome was observed. However, zeolite metastability is most commonly encountered in the phenomenon of reaction over-run, in which the zeolite product decomposes under the reaction conditions to afford a more dense phase. In this way, aluminous zeolites transform into dense silica phases, usually quartz or cristobalite. Intermediate cases maintain the materials balance by undergoing a type of disproportionation, so that aluminous ZSM-5 products decompose to quartz and a more aluminous zeolite such as mordenite or (for high-Al samples) analcime. These latter cases provide examples of the conversion of one zeolite into another. Whilst these instances are more likely to be troublesome than helpful, there are cases in which zeolite interconversions can be of practical use, or interesting from a mechanistic point of view.

One of the earliest successful zeolite syntheses –and the first synthesis of a zeolite not found in nature– was the conversion of analcime into two KFI phases by Barrer in 1948 [7–9]. This synthesis was not of the OH^- -mediated type but involved heating the starting phase in strong solutions of barium salts at 170-270 °C. The same generic procedure was the subject of a more recent detailed study of the hydrothermal conversion of zeolite LTA into zeolite Li-A(BW) using aqueous LiCl at temperature of 180-260 °C [50]. The crystallisation was followed by in-situ time resolved synchrotron XRD combined with ex-situ SEM of partially converted samples. These combined

techniques clearly showed that the inter-zeolite conversion was a solution-mediated process, the Li-A(BW) product growing radially from nucleation sites on the parent LTA crystals.

A complex and interesting system of transformations surrounds the synthesis of zeolite omega, the synthetic analogue of the mineral zeolite mazzite and also isostructural with the synthetic phase ZSM-4. Many syntheses of zeolite Na-Y will over-run to give zeolite Na-P. However, in the presence of tetramethylammonium (TMA) ions, this transition does not occur, the faujasite decomposing instead to zeolite ZSM-4. In the study by Dwyer and Chu [51], no ZSM-4 was formed until the faujasite crystallisation was complete and there was no evidence for any amorphous or crystalline intermediate, the ZSM-4 appearing to nucleate on the surface of the dissolving faujasite crystals. Broadly similar results were reported for zeolite omega [52]. A more recent investigation found that faujasite appeared as an intermediate in Na, TMA-omega synthesis at 100 °C but was not observed at 135 °C. Depending upon the choice of reagents and the reaction conditions, sodalite, analcime, mordenite and cristbalite were also observed as co-products [53]. Other transformations which have been reported include pseudomorphic transformation of zeolite Na-A into nepheline by the action of water vapor at 600 °C [54].

Two research groups have made particular studies of zeolite-zeolite transformation. Subotić and coworkers carried out a detailed investigation of the conversion of zeolite A into hydroxyl sodalite which occurs in concentrated (>10%) sodium hydroxide solutions [55,56]. Working in the temperature range 70-85 °C, they monitored the reaction mixture and particle populations present in the reaction mixture and measured the concentrations of silica and alumina in solution. From a detailed analysis of the reaction

kinetics, they concluded that the reaction was a solution-mediated process in which the zeolite A dissolved and the sodalite product nucleated heterogeneously. The growth of the sodalite crystals (by surface addition of monomeric silicate and aluminate ions) was the rate-limiting step of the conversion. No intermediate phases were detected and the transformation rate increased strongly with increasing NaOH concentration. Similar conclusions were reached in parallel study of the conversion of zeolite A into zeolite P which occurs under comparable conditions but at lower base concentrations [57].

The other team to investigate zeolite-zeolite transformations in detail is that of Zones et al. The work initially set out along the lines of the faujasite \rightarrow omega conversion, exploiting the unusual organo-cations which were to become such a characteristic feature of this group's work. In this way, cubic zeolite P (Na-P_C) was transformed into zeolite SSZ-13 (a high-silica chabazite) by the action of the *N,N,N*-trimethylammonium-1-adamantane cation, although the presence of further silica was necessary to satisfy the mass balance [58]. By using Na-P_C as starting material, other templates gave sodalite (from TMA) and (from quaternaries containing cyclic units) the zeolite SSZ-16, SSZ-17 (NU-3) and SSZ-19 [59]. In all cases, the organocations were incorporated into the crystalline products. With the extension of this work to faujasites as starting reagents [60], an interesting synthetic method began to develop, since it was found that the reactivity of the system could be modified by treating the primary zeolites in different ways, for example by steaming, calcination or ion exchange. The synthetic utility of inter-zeolite conversions was subsequently well demonstrated by the versatility discovered for boron-beta zeolite, which gave enhanced nucleation, increased reaction rates, greater flexibility in choice of template and new possibilities for lattice substitution. In later studies, it was also found that, for a given

template, product selectivities could be altered by changing the initial B/SiO₂ ratio, for example by adding extra borate to the reaction mixture [61].

These new synthesis strategies for zeolite to zeolite transformations have subsequently been adopted by other workers [62]. Their utility stems from the additional degree of control attainable in these crystalline products. In addition, a crystalline precursor may have unusual surface reactivity, e.g. for the generation of heterogeneous nucleation sites.

Sano et al. have also investigated the synthesis of zeolites using another zeolite. They termed this methodology the “interzeolite conversion method” and have succeeded in the syntheses of *BEA- [63], RUT- [64], and MTN zeolites [65] from FAU zeolite. Although these zeolites were obtained from amorphous materials under the same condition, the use of FAU zeolite as the starting material resulted in a crystallization rate superior to that achieved with conventional zeolite synthesis, in which amorphous aluminosilicate gel is used as the starting material. The enhanced crystallization rate was due to the decomposition/dissolution of the starting zeolite species, which generated locally ordered aluminosilicate species (nanoparts), which in turn assembled and transformed into a different type of zeolite [66].

As mentioned above, the interzeolite conversion method affords the design synthesis of a zeolite, which cannot be obtained via a conventional hydrothermal technique from amorphous materials, and explaining the formation mechanism of zeolite structure.

3. Introduction to layer silicate

3.1 Layer silicate

Layer materials have tetrahedral sheets composed of tetrahedrally-bidimensionally-connected frameworks and octahedral sheets composed of net-like-connected frameworks such as Al–O or Mg–O etc. Figure 1-6 shows the tetrahedral sheets and octahedral sheets [67]. The tetrahedral and octahedral sheets make the 1:1 layers or 2:1 layers which are called multiple silicate layers. The layers compose three dimensional structures by piling up themselves. They are piled up by van der waals interaction, and 1:1 layers and 2:1 layers make 1:1 type structure and 2:1 type structure, respectively.

In generally, the chemical formula for layer silicate is $M_2O \cdot xSiO_2 \cdot yH_2O$ (M = alkali or alkali earth metal, $x = 2-40$, $y = 1-20$). Alkali metal cations are presence between the bidimensional sheets, therefore the cations can be exchanged with other kinds of cations. The classification of types of layer silicates is conducted by kinds of cations, composition ratio and crystal structures. The material character of a layer silicate such as the thermal stability and acidity is different among the kinds of layer silicates, because the thickness and condensation degree of layer silicate change with a change of types.

The layer silicate has a variety of performances such as an ion-exchange property and a reactive property of sililation and esterification with using surface silanol. Therefore layer silicates are expected as industrial materials.

It is known that intercaration of the organic or inorganic cations makes progress reversibly by an ion-exchange property [68]. It is also known that the layer silicate is able to be intercarated with polar organic molecules after the protnation of interlayer [69]. These layer silicates introduced organic molecules come to be able to be

introduced organic polymers into interlayer [70]. These layer silicate–polymer nano complexes have interesting properties, so they are expected for applying the nano complex materials.

The layer silicate is also using as a silane coupling agent with surface silanol on the layer. The silanol groups react with alcohol and immobilize compounds with covalent bonds in interlayer. The characteristics of the layer silicate reacting reactants can change by selecting the reactant organic molecules. The organic molecules are selected by different sizes or organophilicities, because they are selected by adsorption targets the same as dissolved catalysts or harmful materials. To adjust the adsorption properties, layer silicates are expected for depleting agents of deadwood in water [71].

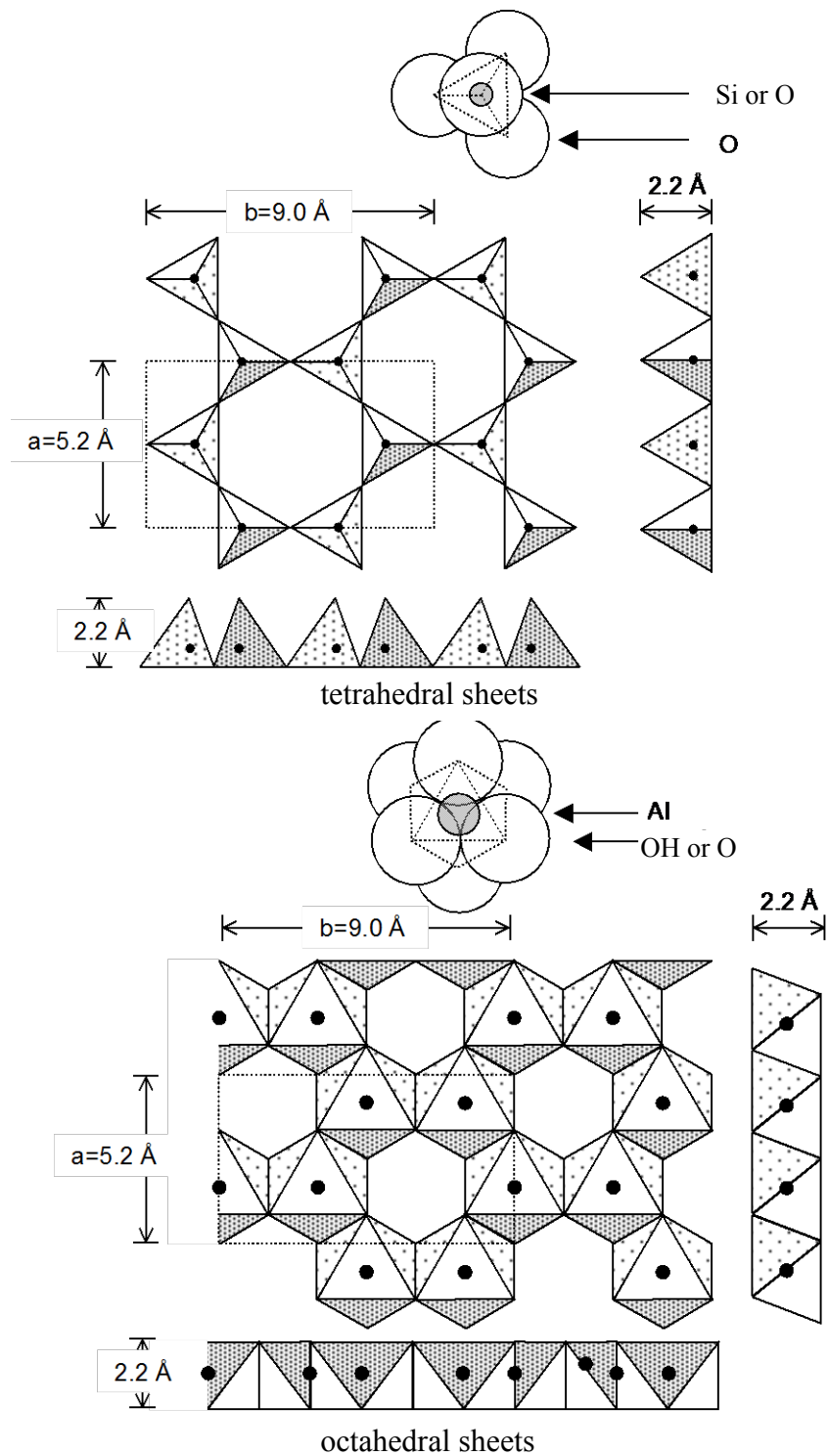


Fig.1-6 Structures of sheets[67]

3.2 Zeolitic layer silicate

Layer silicates (magadiite, octasilicate et al.) discovered as clay minerals are able to be synthesized by hydrothermal treatment of aqueous gel mixed SiO_2 sources and alkali metal hydroxide. On the other hand, zeolitic layer silicates are able to be synthesized with OSDA the same as zeolite. β -HLS and RUB-15 are synthesized with using tetramethylammonium, it is used as OSDA of SOD zeolite, therefore they have topology like SOD zeolite [72,73]. Figure 1-7 shows model structures of β -HLS, RUB-15 and SOD zeolite. It is understood anew that β -HLS and RUB-15 have topology like SOD zeolite from the model structures. Table 1-1 shows various zeolitic layer silicates. Recently many scientists research the synthesis of a novel layer silicate with using organic ammonium. The synthesis of RUB-51 [74] having a topology like a zeolite with using benzyltrimethyl- ammonium hydroxide and the synthesis of SSZ-70 [75,76] having micropores with using imidazolium derivative were reported.

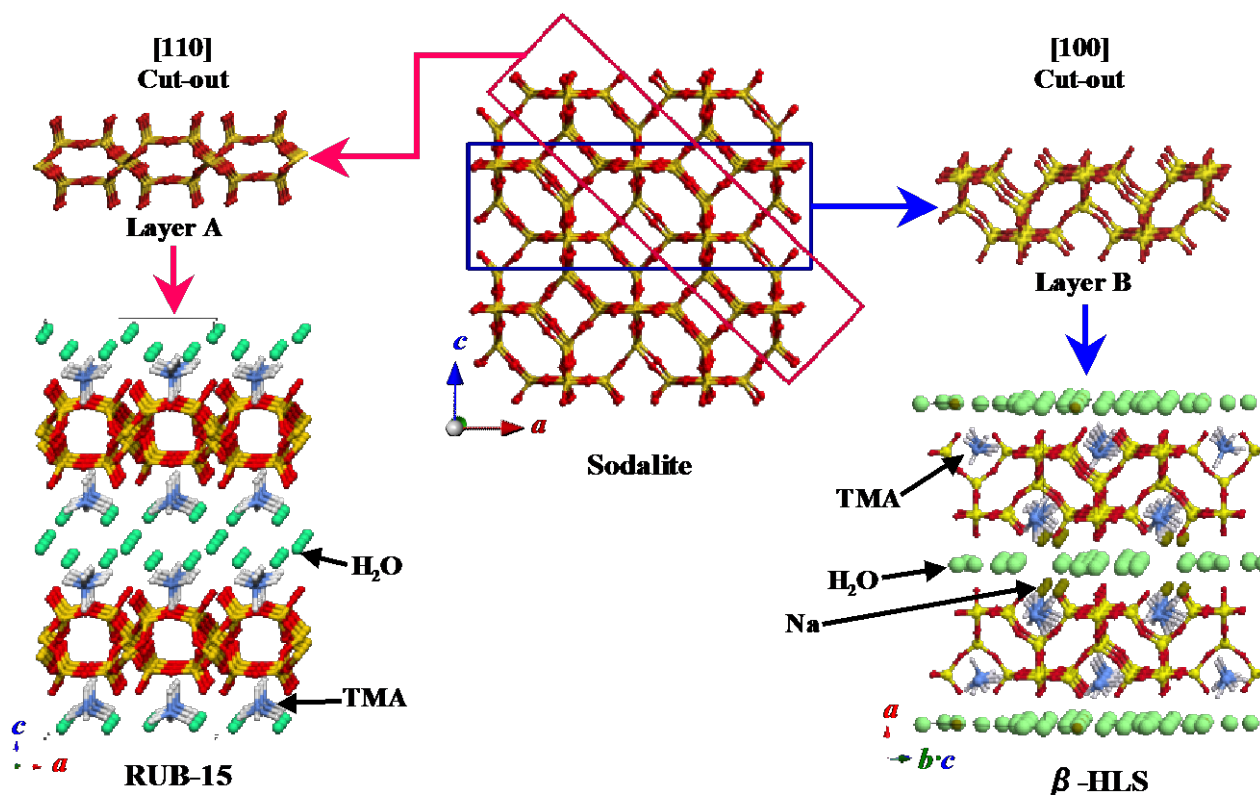


Fig. 1-7 Structures of RUB-15, β -HLS and sodalite.

Table 1-1 Layered silicates possessing zeolitic frameworks

Topology	Layered silicate
SOD	RUB-15, DLM-2, β -HLS, RUB-51
FER	PREFER, PLS-3
CDO	PLS-1, PLS-4, RUB-36, UZM-13, MCM-65
RWR	R-RUB-18
NSI	Nu-6(1)
RRO	RUB-39

3.3 Layer structure as transients and precursors

Zeolites are three-dimensional (3-D) crystalline materials containing tetrahedral framework atoms, while clays are two-dimensional (2-D) materials containing both tetrahedral and octahedral atoms. The 2-D building units can be regarded as layers that are aligned the third dimension by ionic or hydrogen bonds. About four decade ago, researchers found that the interlayer inorganic cations of smectite clays are converted to oxide pillars such as alumina, titania and zirconia, which keep the layers separated from each other to build 3-D interlayer microporous network structures.

There have been several different instances of the appearance of lamellar materials during the course of zeolite syntheses. Materials with layer structure such as the silicates kanemite, magadiite or ilerite (sodium *octasilicate*) have been used as starting materials [77]. A number of such syntheses fall into the category of apparent *solid state transformations*. In some cases, amorphous micro-precipitates have been observed in the form of lamellae, upon which the zeolite product appeared to nucleate [78]. In other situations, crystalline intermediates having layer structures have been observed before zeolite crystallization and have been regarded as precursors to the subsequent three-dimensional microporous networks [79-81]. In the crystallization of TEA-beta, a similar observation led Lohse et al. to conclude that the zeolite was formed via a direct transformation of a layered aluminosilicate [82]. In none of these cases is there proof of the suggested 2D \rightarrow 3D transformation. Some possible structural relationships between layered alkali metal silicates and the mordenite and pentasil-group zeolites have been discussed by Garcés et al. [83].

Tuel has made a detailed study of the synthesis of zeolites ZSM-48 and beta with hexamethonium and tetraethylammonium cations, respectively [84]. In both cases, high

crystalline layered organo-silicates or organo-aluminosilicates were formed at short synthesis times but gradually decomposed to amorphous materials. The zeolite products started to form only after the complete degradation of the layered structures. The two layered compounds, although from different reaction systems, seemed to possess very similar structures, whereas there were no elements common to the XRD patterns of the final zeolite products. It was concluded that the layered materials dissolved in the reaction medium, providing nutrients which were reused in the crystallization of the zeolites, the structure of which depended only on the nature of the quaternary ammonium OSDA cation present in the liquid phase.

On the other hand, a different situation on converting methods of layer silicates to zeolites exists. It is using isolation and high-temperature calcination. In general, the initial structure is that of a two-dimensional, layered complex which, on removal of the organic *–spacers*”, becomes converted into a three-dimensional framework by the condensation of silanol groups. The first example of a zeolite formed by calcination of a layer-structured precursor appears to be that of NU-6 [85]. Later examples include the silica polymorph EU-20 [86] and the borosilicate ERB-1 [87]. Most detail is available in the case of *–PREFER*”, where the transformation of this two-dimensional aluminosilicate into the zeolite ferrierite on calcination at 550°C has been carefully studied [88]. The XRD pattern of PREFER contains diffraction lines similar to those of the derived zeolite, reflecting the structural conformity between the two materials. The precursor appears to consist of ferrierite-type sheets in the *bc* plane, separated by molecules of the bulky OSDA (4-amino-2,2,6,6-tetramethylpiperidine). On burning out the occluded organic molecule, the ferrierite layers progressively link together in the α -direction as new T–O–T linkages are formed by condensation reactions.

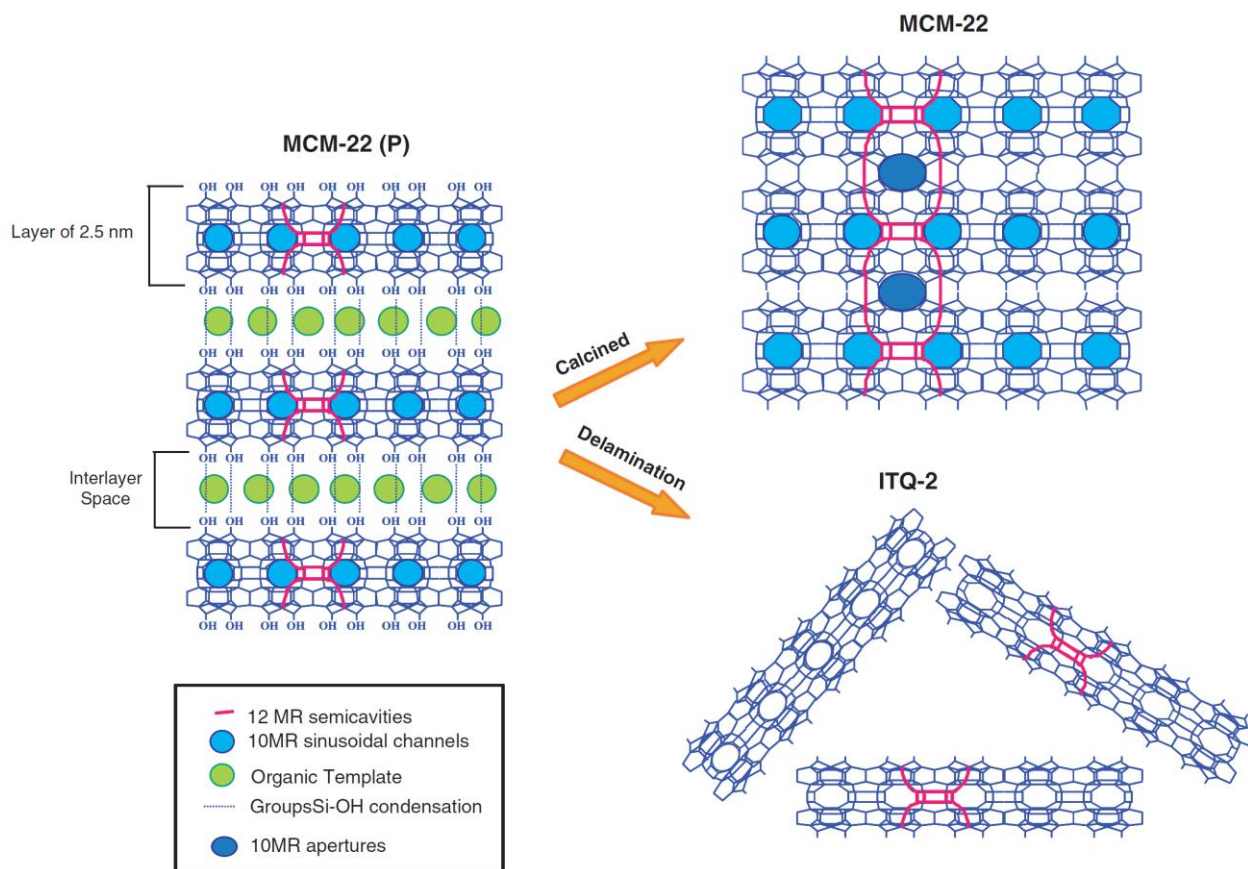


Fig. 1-8 Scheme for the preparation of various materials from the MWW-type zeolite precursor MCM-22 (P) and ITQ-2 [97].

However, it is also possible to modify this process. PREFER and related materials can be delaminated and reassembled in a number of ways to give a series of high surface area derivatives with catalytically active sites accessible to bulky reactants. Examples from the Valencia school are ITQ-2 [88], ITQ-6 and ITQ-36 [89]. Similar relationships characterize the noble MCM-22 family [90,91] which already form the basis for a new and commercially operating process for the manufacture of ethyl benzene [92]. The synthesis of MCM-22 was claimed to occur through a lamellar zeolitic precursor, MWW (P), formed by individual sheets (thickness of 2.5 nm), which are ordered perpendicularly to axis *c* and separated one to each other by the OSDA. After

calcination, the layers condense, and the tridimensional structure of MWW is obtained. This is composed of two independent pore systems: one formed by 12MR cages connected by 10MR apertures, and the other is defined by a well differentiated 10MR circular channel (Fig. 1-8) [93-97].

Tatsumi et al. have applied a similar strategy to layered zeolite precursors to obtain crystalline microporous materials, which were named interlayer expanded zeolites (IEZ) [98]. Treatment of the zeolitic layered precursor of Al-MWW (MCM-22(P)) with diethoxydimethylsilane (DEDMS) in acid media gave an aluminosilicate-type interlayer-expanded zeolite MWW (Al-IEZ-MWW) with expanded 12MR micropores (Fig. 1-9). By the interlayer-silylation of Al-MWW (P), the micropore diameter of

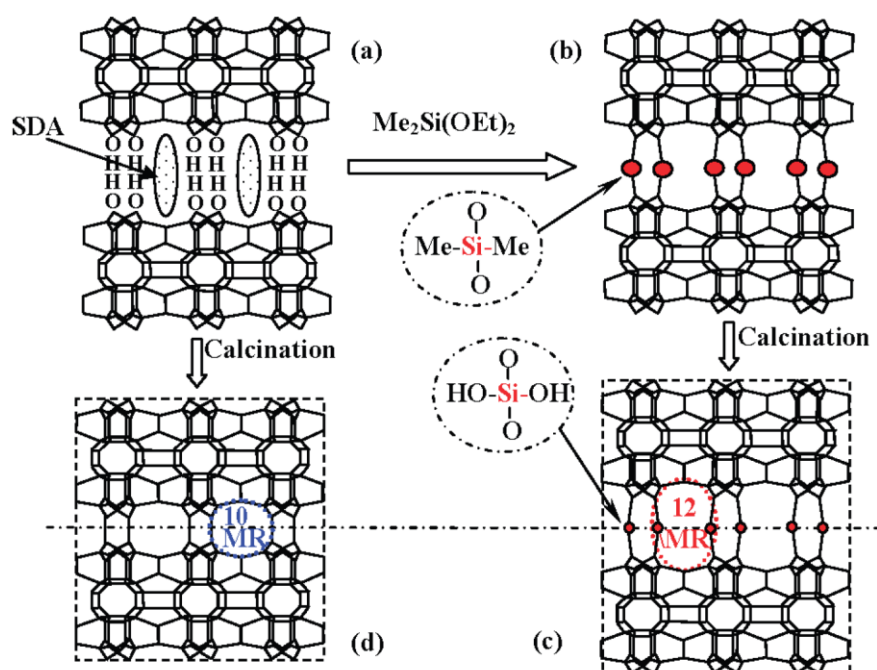


Fig.1-9 Formation of interlayer-expanded zeolite (IEZ) of Al-MWW as an example.

interlayer with 12MR supercages enlarged from ca. 7.0 to 8.0 Å, verifying the formation of the interlayer-expanded structure. Thus prepared Al-IEZ-MWW serves as a useful

acid catalyst for large molecules, e.g. the Friedel-Crafts acylation of anisole with acetic anhydride [99], and the Beckmann rearrangement of cyclohexanone oxime [98], being superior to Al-MWW with only 10MR micropores. This novel methodology for preparing IEZ materials can be widely applied to various layered zeolitic precursors such as Ti- and Ga-MWW(P), PREFER, PLS-1, and MCM47 in addition to Al-MWW(P) [98].

4. Application of zeolite

Zeolites are important industrial materials that have a broad range of applications. Many zeolites with different structures and compositions are commercially available and used in refining and chemical processing. In addition, natural zeolites because of their lower cost are used in bulk mineral applications.

In Table 1-2, a summary of the typical commercial zeolite adsorbent product is presented, together with short descriptors of the chemical composition and example applications. A brief study of the information in Table 1-1 will quickly draw attention to the fact that majority of the key adsorbents for the industrial gas business are essentially low silica zeolites, in general processing $\text{SiO}_2/\text{Al}_2\text{O}_3$ ratios < 5 . The higher $\text{SiO}_2/\text{Al}_2\text{O}_3$ ratio zeolites, which are commonplace amongst industrial zeolite catalysts, have found niche applications in adsorption processes, with the focus being in hydrocarbon and/or desulfurization applications. In commercially available low silica zeolite family, those belonging to the A and X types have the greatest number of currently available products. The primary differentiator between these different products is the type of extra-framework cation, and for the zeolite X family, the $\text{SiO}_2/\text{Al}_2\text{O}_3$ ratio. The use of ion-exchange techniques to alter the adsorption properties of these A and X, and to a

lesser extent zeolite Y adsorbents, has proven to be the most successful method of adsorbent modification, in current commercial use [100].

Table 1-2 Important industrial adsorbents and example applications^a.

Framework code	Commercial products	SiO ₂ /Al ₂ O ₃	Cations	Application Examples
LTA	3A	2	K > 70%	EtOH dehydration, Drying
	4A	2	Na > 99%	Desiccant, Medical O ₂ , other PSA, Natural gas processing
	5A	2	Ca > 70%	H ₂ PSA, Medical O ₂ , VPSA O ₂ , Natural gas processing
FAU (Zeolite X)	13X	2-2.5	> 99% Na	Air prepurification
	LiX	2-2.5	> 88% Li	VPSA O ₂ , Medical O ₂
	AgX	2-2.5	> 80% Ag	CO, H ₂ adsorbent
	BaX		Ba, K	<i>p</i> -xylene recovery
	CaX	2-2.5	> 70% Ca	H ₂ PSA, N ₂ O removal, VPSA
FAU (Zeolite Y)	NaY	3-5	> 99% Na	Desulfurization, HC separation
	HY	20-1000	H ⁺	Desulfurization, HC separation
MOR	Small/Large Port	5	Na	Desulfurization, HC separation
HEU	TSM-140/CS400	6	Mixed (Na, K, Ca, Mg)	N ₂ O removal

^a: PSA: pressure swing adsorption, VPSA: vacuum pressure swing adsorption, HC: hydrocarbon

Catalysis is one of the most important fields of application of zeolites. In 1999, Tanabe and Holderich have published an interesting survey of the industrial processes based on the use of solid acid-base catalysts, highlighting the primary role played by zeolites. They found that a total of 127 industrial processes employ 180 solid catalysts, of which 74 include at least a zeolite phase. A more detailed view of the survey results indicated that only a few framework types are effectively used, being MFI, FAU, MOR, and *BEA the most extensively employed [101]. Oil refining and petrochemistry are important industrial sectors where zeolites find a widespread use as heterogeneous acid catalysts and molecular sieves. The role and the increasing importance of zeolite

catalysts is examined through the Fluid Catalytic Cracking (FCC), one of the most important process in the modern refinery, and the synthesis of cumene, the intermediate in the production of phenol. Advantages of zeolites that are being exploited include heterogenization of catalysts for easy separation framework, doping with metals for selective oxidation chemistry, and ease of regeneration of catalysts. Among the most important properties of zeolites with respect to their use as catalyst is their surface acidity. Both Brønsted and Lewis acid sites occur in zeolites. To describe the acidity of zeolites in an adequate manner, it is mandatory to clearly distinguish between (i) the nature of acid sites (i.e. Brønsted vs. Lewis acidity), (ii) the density or concentration of these sites, (iii) their strength of strength distribution and, last but not least, (iv) the precise location of the acid sites.

By their negatively charged porous framework and the small and mobile cations sitting in the pores, zeolites are typical ion exchangers. In fact, zeolites are widely used as builders in laundry detergents where their role is to take up calcium and magnesium ions in exchange for sodium ions, thereby softening the washing water. Obviously, as high as possible cation exchange capacity and, hence the highest possible aluminum content in the framework (Si/Al ratio = 1) are desired for this application. This is the domain of zeolite A, and as a whole, the use of zeolites as ion-exchangers in detergents represents their largest market in terms of tonnage with a worldwide production rate close to 1 million t/year [4].

Over the past twenty years the development of zeolite-based membrane has attracted considerable research efforts [102,103]. The great expectations related with zeolites as separation media are based on their selectivity that could be used to separate molecules with difference in size below 1 Å [104]. Besides the unraveled selectivity, the particular

properties of zeolite membranes that attracted the attention of academic and application scientists are: (i) long-term stability at high temperature, (ii) resistance to harsh environments, (iii) resistance to high pressure drop, (iv) inertness of microbiological degradation, (v) easy cleanability and catalytic activation. The interest in zeolite membrane is also related with the nowadays requirements for the minimization of energy consumption and cleaner technologies [105,106].

Other niche applications include sensor, photochemical organic transformations, and conversion of solar energy. Bulk applications for zeolite powders have emerged for odor removal and as plastic additives.

5. Brief of this thesis

As described the previous sections, zeolites are employed in various industrial processes. However, types of employed zeolites are specified due to the complex synthesis process of OSDAs, which makes the production cost up. On the basis of the problem, an alternative synthesis route should be considered and investigated. Therefore, in this thesis, I studied efficient syntheses of zeolites by interzeolite conversion method. Namely, three syntheses methods, seed-assisted synthesis, OSDA-free synthesis and seed-free-OSDA-free synthesis are investigated in detail; In addition, I investigated the synthesis of layered silicates by the interzeolite conversion. Research areas I focused on are follows;

1. Seed-assisted OSDA-free syntheses of various zeolites by interzeolite conversion (Chapter 2, 3, 4)
2. Interzeolite conversion process on seed-assisted OSDA-free synthesis (Chapter 5)
3. OSDA-free interzeolite conversion without seeding (Chapter 6)

4. A novel layer silicate synthesis by interzeolite conversion and the structural analysis
(Chapter 7)

5. An efficient way to synthesize the novel layer silicate and its application (Chapter 8)

Through my study, I succeeded in developing the efficient synthesis routes of zeolite and layer silicate by the interzeolite conversion method. The my findings will contribute to a more efficient alternative method for synthesizing new zeolites and layered silicates.

References

- [1] D.S. Wragg, R.E. Morris, A. W. Burton, *Chem. Mater.* 20 (2008) 1561.
- [2] R.M. Barrer, *J. Chem. Soc.* (1948) 127.
- [3] Database of Zeolite Structures, Structure Commission of the International Zeolite Association, <http://www.izastructure.org/databases/>
- [4] J. Weitkamp, *Solid State Ionics.* 131 (2000) 175.
- [5] M.E. Davis, R.F. Lobo, *Chem. Mater.* 4 (1992) 756.
- [6] H. de St Claire Deville, *Compt. Rend. Séances Acad. Sci.* 54 (1862) 324.
- [7] R.M. Barrer, *J. Chem. Soc.* (1948) 127.
- [8] R.M. Barrer, L. Hinds, E.A. White, *J. Chem. Soc.* (1953) 1466.
- [9] R.M. Barrer, C. Marcilly, *J. Chem. Soc. (A)* (1970) 2735.
- [10] Ch. Baerlocher, W.M. Meier, D.H. Olson, *Atlas of Zeolite Structure Types*, fifth ed., Elsevier, Amsterdam, (2001).
- [11] G.T. Kerr, *Science* 140 (1963) 1412.
- [12] G.T. Kerr, *Inorg. Chem.* 5 (1966) 1539.
- [13] R.M. Milton, US Patent 2,882,243 (1959).
- [14] R.M. Milton, US Patent 2,882,244 (1959).
- [15] R.M. Milton, M.L. Ocelli, H.E. Robson (Eds.), *Zeolite Synthesis*, ACS Symp. Ser. 398 (1989) 1.
- [16] R.M. Barrer, P.J. Denny, *J. Chem. Soc.* (1961) 971.
- [17] G.T. Kerr, G.T. Kokotailo, *J. Am. Chem. Soc.* 83 (1961) 4675.
- [18] G.T. Kerr, *Inorg. Chem.* 5 (1966) 1537.
- [19] R.L. Wadlinger, G.T. Kerr, E.J. Rosinski, US Patent 3,308,069 (1967).
- [20] R.J. Argauer, G.R. Landolt, US Patent 3,702,886 (1972).

- [21] R. Szostak, *Molecular Sieves—Principles of Synthesis and Identification*, Van Nostrand Reinhold, New York, 1989, second ed., Blackie, London, (1998).
- [22] S.T. Wilson, B.M. Lok, C.A. Messina, T.R. Cannan, E.M. Flanigen, *J. Am. Chem. Soc.* 104 (1982) 1146.
- [23] M.E. Davis, C. Saldarriaga, C. Monte, J. Garces, C. Crowder, *Nature* 331 (1988) 698.
- [24] S.M. Kuznicki, US Patents 4,853,202 (1989), 4,938,939 (1990).
- [25] T. Blasco, M.A. Cambor, A. Corma, P. Esteve, A. Martinez, C. Prieto, S. Valencia, *Chem. Commun.* (1996) 2367.
- [26] Y. Oumi, T. Manabe, H. Sasaki, T. Inuzuka, T. Sano, *Appl. Catal. A* 388 (2010) 256.
- [27] A. Corma, M.T. Navarro, F. Rey, J. Rius, S. Valencia, *Angew. Chem. Int. Ed.* 40 (2001) 2277.
- [28] J.-L. Paillaud, B. Harbuzaru, J. Patarin, and N. Bats, *Science* 304 (2004) 990.
- [29] A. Corma, M.J. Diaz-Cabanas, J.L. Jorda, C. Martinez, M. Moliner, *Nature* 443 (2006) 842.
- [30] S. L. Burkett, M. E. Davis, *Chem. Mater.* 7 (1995) 920.
- [31] J. Ciric, US Patent 3,950,496 (1976).
- [32] D.F. Shantz, A. Burton, R.F. Lobo, *Micropor. Mesopor. Mater.* 31 (1999) 61
- [33] R. Lobo, S. I. Zones, M. E. Davis, *J. Inclus. Phenom. Mol. Rec. Chem.* 21 (1995) 47.
- [34] H. Gies, B. Marler, *Zeolites*, 12 (1992) 42.
- [35] A. Moini, K.D. Schmitt, R.F. Polomski, *Zeolites*, 18 (1997) 2.
- [36] C.C. Freyhardt, M. Tsapatsis, R.F. Lobo, K.J. Bulkus, M.E. Davis, *Nature* 295 (1996) 381.

- [37] P. Wagner, M. Yoshikawa, M. Lovallo, K. Tsuji, M. Taspatsis, M.E. Davis, *Chem. Commun.*, (1997) 2179.
- [38] S.A. Elomari, S.I. Zones, *Stud. Surf. Sci. Catal.* 135 (2001) 479.
- [39] A. Burton, S. Elomari, C.-Y. Chen, R.C. Medrud, I.Y. Chan, L.M. Bull, C. Kibby, T.V. Harris, S. I. Zones, E.S. Vittoratos, *Chem. Eur. J.* 9 (2003) 5737.
- [40] J. Sun, C. Bonneau, Angel Cantin, A. Corma, M.J. Diaz-Cabanas, M. Moliner, D. Zhang, M. Li, X. Zou, *Nature* 458 (2009) 1154.
- [40] B.-W. Lu, T. Tsuda, Y. Oumi, K. Itabashi, T. Sano, *Micropor. Mesopor. Mater.*, 76, 1 (2007).
- [41] G.T. Kerr, *J. Phys. Chem.*, 70 (1966) 1047.
- [42] G.T. Kerr, *J. Phys. Chem.*, 72 (1968) 1385.
- [43] Y. V. Mirskii, V.V. Pirozhkov, *Russ. J. Phys. Chem.*, 74 (1970) 1508.
- [44] J. Warzywoda, R.W. Thompson, *Zeolites*, 11 (1991) 577.
- [45] G. Majano, A. Darwiche, S. Mintova, V. Valtchev, *Ind. Eng. Chem. Res.* 48 (2009) 7084.
- [46] B. Xie, J. Song, L. Ren, Y. Ji, F.-S. Xiao, *Chem. Mater.* 20 (2008) 4533.
- [47] G. Majano, L. Delmotte, V. Valtchev, S. Mintova, *Chem. Mater.* 21 (2009) 4184.
- [48] K. Itabashi, Y. Kamimura, K. Iyoki, A. Shimojima, T. Okubo, *J. Am. Chem. Soc.* 134 (2012) 11542.
- [49] A. Erdem, L.B. Sand, *J. Catal.* 60 (1979) 241.
- [50] P. Norby, *J. Am. Chem. Soc.* 119 (1997) 5215.
- [51] F.G. Dwyer, P. Chu, *J. Catal.* 59 (1979) 263.
- [52] A.J. Perrotta, C. Kibby, B.R. Mitchell, E.R. Tucci, *J. Catal.* 55 (1978) 240.
- [53] F. Fajula, M. Vera-Pacheco, F. Figueras, *Zeolites* 7 (1987) 203.

- [54] J. Richter-Mendau, W. Lutz, A. Grossmann, *Cryst. Res. Technol.* 23 (1988) 1245.
- [55] B. Subotić, D. Škrčić, I. Šmit, L. Sekanović, *J. Cryst. Growth* 50 (1980) 498.
- [56] B. Subotić, L. Sekanović, *J. Cryst. Growth* 75 (1986) 561.
- [57] B. Subotić, I. Šmit, O. Madžija, L. Sekanović, *Zeolites* 2 (1982) 135.
- [58] S.I. Zones, R.A. Van Nordstand, *Zeolites* 8 (1988) 166.
- [59] S.I. Zones, R.A. Van Nordstand, *Zeolites* 8 (1988) 409.
- [60] S.I. Zones, *J. Chem. Soc. Faraday Trans.* 87 (1991) 3709.
- [61] S.I. Zones, Y. Nakagawa, *Micropor. Mater.* 2 (1994) 557.
- [62] R.K. Ahedi, Y. Kubota, Y. Sugi, *J. Mater. Chem.* 11 (2001) 2922.
- [63] H. Jon, K. Nakahata, B. Lu, Y. Oumi, T. Sano, *Micropor. Mesopor. Mater.* 96 (2006) 72.
- [64] H. Jon, S. Takahashi, H. Sasaki, Y. Oumi, T. Sano, *Micropor. Mesopor. Mater.* 113 (2008) 56.
- [65] H. Sasaki, H. Jon, M. Itakura, T. Inoue, T. Ikeda, Y. Oumi, T. Sano, *J. Porous Mater.* 16 (2009) 465.
- [66] H. Jon, N. Ikawa, Y. Oumi, T. Sano, *Chem. Mater.*, 20 (2008), 4135.
- [67] 白水春雄, 粘土鉱物学—粘土科学の基礎—, 朝倉書店, (1988)
- [68] 村石治人, 粘土科学, 44 (2004) 62.
- [69] W. Schwieger, W. Herer, K. H. Bergk, *Z. Anorg. Allg. Chem.*, 600 (1991) 139.
- [70] S. S. Ray, M. Kato, *Prog. Polym. Sci.*, 28 (2003) 1539.
- [71] I. Fujita, K. Kuroda, M. Ogawa, *Chem. Mater.*, 15 (2003) 3134.
- [72] T. Ikeda, Y. Akiyama, F. Izumi, Y. Kiyozumi, F. Mizukami, T. Kodaira, *Chem. Mater.*, 13 (2001) 1286.
- [73] U. Oberhagemann, P. Bayat, B. Marler, H. gies, J. Rius, *Angew. Chem. Int. Ed.*, 35

- (1996) 2869.
- [74] Z. Li, B. Marler, H. Gies, *Chem. Mater.*, 20 (2008) 1896.
- [75] R. H. Archer, S. I. Zones, M. E. Davis, *Micropor. Mesopor. Mater.*, 130 (2010) 255.
- [76] R. H. Archer, J. R. Carpenter, S.-J. Hwang, A. W. Burton, C.-Y. Chen, S. I. Zones, M. E. Davis, *Chem. Mater.*, 22 (2010) 2563.
- [77] F. Feng, K.J. Balkus Jr., *Micropor. Mesopor. Mater.* 69 (2004) 85.
- [78] C.S. Cundy, B.M. Lowe, D.M. Sinclair, *J. Cryst. Growth* 100 (1990) 189.
- [79] U. Oberhagemann, P. Bayat, B. Marler, H. Gies, J. Rius, *Angew. Chem. Int. Ed.* 35 (1996) 2869.
- [80] S. Vortmann, J. Rius, S. Siegmann, H. Gies, *J. Phys. Chem. B* 101 (1997) 1292.
- [81] S. Vortmann, J. Rius, B. Marler, H. Gies, *Eur. J. Mineral.* 11 (1999) 125.
- [82] U. Lohse, B. Altrichter, R. Fricke, W. Pilz, E. Schreier, Ch. Garkisch, K. Jancke, *J. Chem. Soc. Faraday Trans.* 93 (1997) 505.
- [83] J.M. Garcés, S.C. Roche, C.E. Crowder, D.L. Hasha, *Clays Clay Miner.* 36 (1988) 409.
- [84] A. Tuel, *Chem. Mater.* 11 (1999) 1865.
- [85] T.V. Whittam, *Eur. Patent* 0054364 (1982).
- [86] A.J. Blale, K.R. Franklin, B.M. Lowe, *J. Chem. Soc. Dalton Trans.* (1988) 2513.
- [87] R. Millini, G. Perego, W.O. Parker, Jr., G. Bellussi, L. Carluccio, *Micropor. Mater.* 4 (1995) 221.
- [88] L. Schreyeck, P. Caullet, J.-C. Mougénel, J.-L. Guth, B. Marler, *Micropor. Mater.* 6 (1996) 259.
- [89] A. Corma, V. Fornes, S.B. Pergher, Th.L.M. Maesen, J.G. Buglass, *Nature* 396 (1998) 353.

- [90] A. Corma, U. Diaz, M.E. Domine, V. Fornes, *J. Am. Chem. Soc.* 122 (2000) 2804.
- [91] M.K. Rubin, P. Chu, US Patent 4, 954, 325 (1990).
- [92] S.L. Lawton, A.S. Fung, G.J. Kennedy, L.B. Alemany, C.D. Chang, G.H. Hatzikos, D.N. Lissy, M.K. Rubin, H.-K.C. Timken, S. Steuernagel, D.E. Woessner, *J. Phys. Chem.* 100(1996) 3788.
- [93] L. Puppe, J. Weisser, US Patent 4,439,409 (1984).
- [94] M.K. Rubin, P. Chu, US Patent 4,954,325 (1990).
- [95] S.I. Zones, Eur. Patent 231860 (1987).
- [96] R. Millini, G. Perego, W.O. Parker, G. Bellussi, L. Carluccio, *Microporous Mater.* 4 (1995) 221.
- [97] U. Diaz, V. Fornés, A. Corma, *Micropor. Mesopor. Mater.* 90 (2006) 73.
- [98] P. Wu, J. Ruan, L. Wang, L. Wu, Y. Wang, Y. Liu, W. Fan, M. He, O. Terasaki, T. Tatsumi, *J. Am. Chem. Soc.* 130 (2008) 8178.
- [99] S. Inagaki, H. Imai, S. Tsujiuchi, H. Yakushiji, T. Yokoi, T. Tatsumi, *Micropor. Mesopor. Mater.* 142 (2011) 354.
- [100] C. Martinez, J. Perez-Pariente eds., *Zeolites and Ordered Porous Solids: Fundamentals and Applications* (2011).
- [101] K. Tanabea, W.F. Holderich, *Appl. Catal. A*, 181 (1999) 399.
- [102] R.D. Noble, J.L. Falconer, *Catal. Today* 25 (1995) 209.
- [103] T. Bein, *Chem. Mater.* 8 (1996) 1636.
- [104] M. Matsukata, E. Kikuchi, *Bull. Chem. Soc. Jpn.* 70 (1997) 2341.
- [105] E.E. McLeary, J.C. Jansen, F. Kapteijn, *Micropor. Mesopor. Mater.* 90 (2006) 198.
- [106] J. Caro, M. Noack, *Micropor. Mesopor. Mater.* 115 (2008) 215.

Chapter 2

Influence of seeding on FAU-*BEA interzeolite conversion

1. Introduction

Zeolites are microporous aluminosilicate minerals comprised of aluminum, silicon, and oxygen. Since their discovery in the 1700s, they have been applied to various purposes such as water purification, catalysts, laundry detergents, and nuclear processing. Zeolites with unique properties such as solid acidity, large internal surfaces, molecular sieving and ion-exchange abilities are conventionally synthesized by the hydrothermal treatment of amorphous aluminosilicate gel as the starting material in the presence of organic and/or inorganic structure-directing agents (SDAs).

In most zeolite syntheses, an amorphous phase is directly converted to a given type of zeolite; however, the transformation is usually gradual and has the following sequence: amorphous phase → less stable zeolite → most stable zeolite. On this basis, several research groups have pointed out the high potential of an alternative method for zeolite formation, i.e., the hydrothermal conversion of one zeolite type into another (interzeolite conversion). For example, Subotić et al. investigated the hydrothermal conversion of A type zeolite (LTA) into P type zeolite (GIS) and sodalite (SOD) in detail [1-3]. Zones et al. reported the conversion of various zeolites: Y type zeolite (FAU) to SSZ-13; B-*BEA to B-SSZ-24, B-SSZ-31, and B-SSZ-33; and Al-*BEA to Al-SSZ-24 and Al-SSZ-31 in the presence of adamantammonium cation and its derivatives [4-6].

Kubota et al. also successfully converted Al-*BEA and Ti-*BEA into Al-SSZ-31 and Ti-SSZ-24, respectively [7,8]. Recently, we have also succeeded in the synthesis of several types of zeolites such as RUT, *BEA, CHA, MTN, LEV, and OFF zeolites using FAU zeolite as the starting material in the presence various SDAs such as tetramethylammonium hydroxide (TMAOH), tetraethylammonium hydroxide (TEAOH), benzyltrimethylammonium hydroxide (BTMAOH), and choline hydroxide [9-11]. The crystallization rate with FAU zeolite as the starting material is better than with aluminosilicate gel (the conventional synthesis) [12,13]. This is because the decomposition/dissolution of the starting zeolite generates locally ordered aluminosilicate species (nanoparts) that assemble and evolve into another zeolite.

Further, the crystallization rate can also be increased by adding seed crystals of the desired zeolite phase to the starting synthesis gel; obviously, the time required for the crystallization to be completed also decreases [14-17]. Moreover, it is also possible to control the crystal size distribution in this manner [18,19]. The mechanism of the crystallization rate enhancement has not been clearly clarified, but two different explanations have been offered [20]: (i) the increase in the surface area due to the addition of seed crystals results in faster consumption of reagents, or (ii) seeds promote nucleation by some secondary nucleation mechanism.

Organic SDAs (OSDAs) such as organic amine and quaternary ammonium cation are employed in the zeolite syntheses using seed crystals. However, the OSDAs occluded in zeolite cages/pores are generally removed by calcination at high temperatures, and this generates harmful gaseous pollutants. In addition, the use of expensive OSDAs also increases the cost of zeolite. Very recently, the synthesis of zeolites using seed crystals without OSDAs has attracted considerable attention, and several research groups have

already succeeded in the OSDA-free syntheses of ECR-1 [21], ZSM-34 [22], beta [23-25], RUB-13 [26], and ZSM-12 [27] zeolites.

Hence, in this study, in order to obtain detailed information on the interzeolite conversion method, FAU-*BEA interzeolite conversions were performed in the presence of seed crystals under two different synthesis conditions — with and without OSDA. To my knowledge, this is the first report on the OSDA-free FAU-*BEA interzeolite conversions using alkaline metal hydroxides.

2. Experimental

2.1 Synthesis

The starting FAU zeolites and *BEA zeolite seed crystals with various Si/Al ratios were prepared from NH₄-Y zeolite (Si/Al = 2.8, Tosoh Co., Japan) and H-*BEA zeolite (Si/Al = 21, Tosoh Co., Japan) through a dealumination treatment that involved steaming at 700 °C and/or H₂SO₄ (0.42–0.86 M) treatment at 75 °C for 4 h.

The reagents used in this work were TMAOH (20 wt%, Aldrich), TEAOH (35 wt%, Aldrich), BTMAOH (40 wt%, Aldrich), choline hydroxide (50 wt%, Aldrich), lithium hydroxide monohydrate (LiOH·H₂O, >99%, High Purity Chemical Inc. Japan), sodium hydroxide (NaOH, >99%, High Purity Chemical Inc. Japan), potassium hydroxide (KOH, >99%, High Purity Chemical Inc. Japan), rubidium hydroxide aqueous solution (RbOH, 50%, Aldrich), and cesium hydroxide (CsOH, 99.9%, High Purity Chemical Inc. Japan).

The FAU-*BEA interzeolite conversion was performed as follows. The dealuminated FAU zeolite was added into an aqueous solution containing TMAOH, BTMAOH, or choline hydroxide as an OSDA, and 6–33 wt % of the seed crystals (*BEA zeolite)

based on the weight of silica were added. Homogenization was continued until a uniform gel was obtained, and the mixture was then placed into a 30 cm³ Teflon-lined stainless steel autoclave. For the OSDA-free FAU-*BEA interzeolite conversion, alkaline metal hydroxides were used instead of OSDAs. The hydrothermal conversion was conducted at 100–140 °C for 2 h–7 d in a convection oven. After crystallization, the solid product was collected by centrifugation and washed thoroughly with deionized water until it was nearly neutral, and it was then dried overnight at 70 °C. For comparison, starting gels from the following Si and Al sources were also prepared: (a) amorphous silica Nipsil (SiO₂ = 88 wt%, Al₂O₃ = 0.27 wt%, Nippon silica Ind. Japan), and (b) Cab-o-sil M-5 (SiO₂ = 99.8 wt%, Fluka) and either Al(OH)₃ (Wako Pure Chemical Ind. Ltd. Japan), NaAlO₂ (Al₂O₃ = 70 wt%, Kishida Chemical Inc. Japan), or γ -Al₂O₃ (JGC Catalysts and Chemicals Ltd. Japan).

2.2 Characterization

X-ray diffraction (XRD) patterns of the solid products were collected using a powder X-ray diffractometer (Bruker, D8 Advance) with graphite monochromatized Cu K α radiation at 40 kV and 30 mA. The Si/Al ratios were determined by X-ray fluorescence (XRF, Philips PW 2400). 0.5 g of a sample was fused with 5 g of dilithium tetraborate (Li₂B₄O₇) at 1100 °C. The Si/Al ratio was calculated from the Si and Al concentrations as determined by the corresponding calibration curves. The crystal morphology was observed by scanning electron microscopy (SEM, Hitachi S-4800). The thermal analysis was performed using a TG/DTA apparatus (SSC/5200 Seiko Instruments). The sample ca. 7 mg was heated in a flow of air (50 mL min⁻¹) at 5 °C min⁻¹ from room temperature to 800 °C. ¹³C cross polarized magic angle spinning nuclear magnetic resonance

(CP/MAS NMR), ^{27}Al MAS NMR, and ^{29}Si MAS NMR spectra were recorded using a 7 mm diameter zirconia rotor with Bruker Avance DRX-400 NMR at 100.6 MHz, 104.3 MHz, and 79.5 MHz, respectively. The rotor was spun at 4 kHz for ^{13}C CP/MAS and ^{29}Si MAS NMR, and 6 kHz for ^{27}Al MAS NMR. The spectra were accumulated with 6.0 μs pulses, 25 s recycle delay, and 1000 scans for ^{13}C CP/MAS NMR, 2.3 μs , 1 s and 1000 scans for ^{27}Al MAS NMR, and 5 μs , 20 s and 2000 scans for ^{29}Si MAS NMR. $\text{Al}(\text{NO}_3)_3 \cdot 9\text{H}_2\text{O}$ was used as a chemical shift reference for ^{27}Al MAS NMR and $\text{Si}(\text{CH}_3)_4$ was used as a chemical shift reference for ^{13}C CP/MAS NMR and ^{29}Si MAS NMR. Prior to the ^{27}Al MAS NMR measurements, the samples were moisture-equilibrated over a saturated solution of NH_4Cl for 24 h. Nitrogen adsorption isotherms at $-196\text{ }^\circ\text{C}$ were obtained using a conventional volumetric apparatus (Bel Japan, BELSORP 28SA). Prior to the adsorption measurements, the calcined samples (ca. 0.1 g) were evacuated at $400\text{ }^\circ\text{C}$ for 10 h.

3. Results and discussion

3.1 Influence of addition of seed crystals on FAU-*BEA interzeolite conversion in the presence of TEAOH

First, the interzeolite conversion of FAU zeolite into *BEA zeolite using TEAOH as both a SDA and an alkali source was performed at $140\text{ }^\circ\text{C}$ in the absence and presence of seed crystals. The TEAOH/ SiO_2 and $\text{H}_2\text{O}/\text{SiO}_2$ ratios in the starting synthesis gel were 0.15 and 10, respectively. The Si/Al ratio of the used FAU zeolite was 23, while the seed crystals content of *BEA zeolite (Si/Al = 78) was 6 wt%. Figure 2-1 shows the XRD patterns of the products obtained from the FAU zeolite conversion in the presence and absence of seed crystals at various crystallization times. In the both cases, the

diffraction peaks corresponding to FAU zeolite completely disappeared after hydrothermal treatment for 2 h. Further, for the case wherein seed crystals were added, very weak diffraction peaks corresponding to *BEA zeolite were observed after 2 h itself; moreover, highly crystalline *BEA zeolite was obtained after hydrothermal treatment for 2.5 d. In contrast, for the case wherein seed crystals were not added, diffraction peaks corresponding to *BEA zeolite were observed only after hydrothermal treatment for 2.5 d, while highly crystalline *BEA zeolite was obtained only after 6 d of

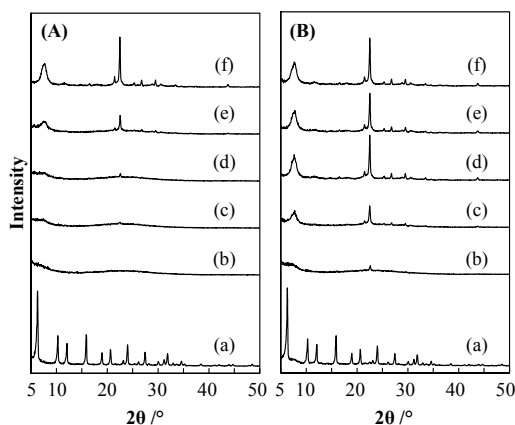


Fig. 2-1. X-ray diffraction (XRD) patterns of products obtained from FAU zeolite (Si/Al = 23) using tetraethylammonium hydroxide (TEAOH) in the (A) absence and (B) presence of 6 wt% seed crystals at various crystallization times: (a) 0 h, (b) 2 h, (c) 1 d, (d) 2.5 d, (e) 4 d, and (f) 6 d.

the treatment. The yield of *BEA zeolite obtained using seed crystals was ca. 80% based on the weight of FAU zeolite, which was larger than that obtained without seed crystals (ca. 70%). These results clearly indicate that the crystallization rate of *BEA zeolite was enhanced by addition of seed crystals into the FAU-*BEA interzeolite conversion process.

Figure 2-2 shows SEM images of the obtained *BEA zeolites and the seed crystals. Although there were no clear differences in the crystal morphology between the *BEA zeolites, the crystals of the obtained *BEA zeolites were smaller than the seed crystals. As compared to the case wherein seed crystals were not added, more smaller crystals

were observed in the SEM image of *BEA zeolite obtained using seed crystals. These smaller crystals are probably a result of the *BEA zeolite produced by the interzeolite conversion of FAU zeolite.

The chemical states of silicon and aluminum in the obtained *BEA zeolite were investigated by ^{29}Si and ^{27}Al MAS NMR. Figures 2-3 and 2-4 show the ^{29}Si and ^{27}Al NMR spectra, respectively, of the *BEA zeolite obtained in the presence of seed crystals. The ^{29}Si MAS NMR spectrum showed weak broad and strong peaks at ca. -103 and ca. -113 ppm, respectively. The NMR resonance at ca. -103 ppm was assigned to an overlap of $\text{SiOH}(\text{OSi})_3$ and $\text{Si}(\text{OAl})(\text{OSi})_3$ while the resonance at ca. -113 ppm was assigned to $\text{Si}(\text{OSi})_4$ [28]. In the CP spectrum of the *BEA zeolite, the peak intensity at

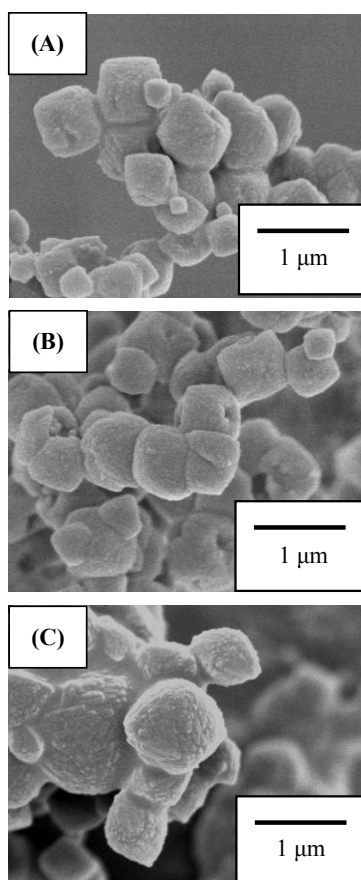


Fig. 2-2. SEM images of *BEA zeolites obtained from FAU zeolite using TEOH in the (A) presence and (B) absence of (C) seed crystals.

ca. -103 ppm was slightly enhanced. As can be observed in the ^{27}Al MAS NMR spectrum, it is clear that only one peak centered at ca. 54 ppm corresponding to tetrahedrally coordinated framework aluminum species was observed, while a peak corresponding to octahedrally coordinated aluminum species, in other words, extra-framework aluminum species, was not observed. This implies that all the aluminum species present in the *BEA zeolite obtained by the interzeolite conversion of the starting FAU zeolite existed within the zeolite framework.

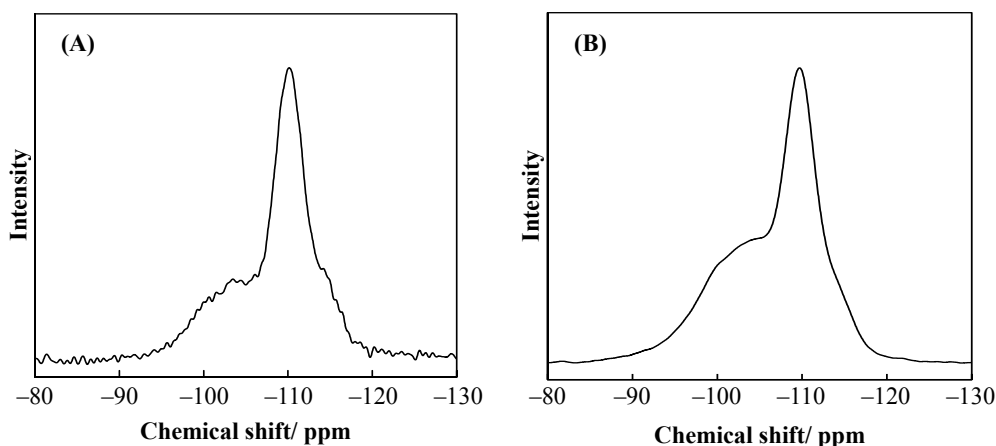


Fig. 2-3. ^{29}Si MAS NMR spectra measured (A) without and (B) with CP for as-synthesized *BEA zeolite using TEAOH in the presence of 6 wt% seed crystals.

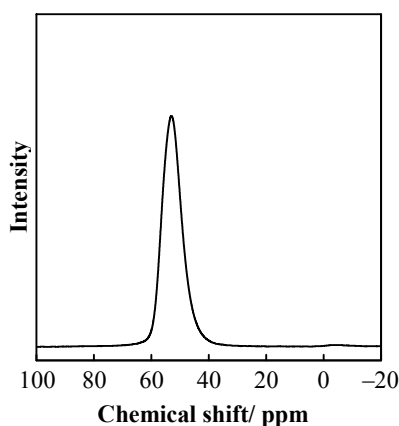


Fig. 2-4. ^{27}Al MAS NMR spectrum of as-synthesized *BEA zeolite using TEAOH in the presence of 6 wt% seed crystals.

Next, in order to clarify the role of seed crystals in the FAU-*BEA interzeolite conversion process, the content of the seed crystals was increased from 6 wt% to 33 wt%, while the hydrothermal temperature was decreased from 140 °C to 125 °C. Figure 2-5 shows the XRD patterns of the products obtained at various crystallization times in the absence and presence of seed crystals. A large difference was observed in the decomposition/dissolution behavior of the starting FAU zeolite. When no seed crystals were added, the diffraction peaks corresponding to FAU zeolite were clearly observed even after hydrothermal treatment for 2 h, and they disappeared completely after 1 d. After hydrothermal treatment for 3 d, strong diffraction peaks corresponding to *BEA zeolite were clearly observed and their intensities remained constant. On the other hand, when seed crystals were added, the diffraction peaks corresponding to FAU zeolite disappeared completely after hydrothermal treatment for 2 h. Surprisingly, the diffraction peaks corresponding to *BEA zeolite was clearly observed after 2 h, and their intensities hardly changed with an increase in the hydrothermal treatment time; this indicates that the crystallization rate of *BEA zeolite was now extremely fast. Furthermore, the enhancement in the crystallization rate strongly suggests that the rate of incorporation of locally ordered aluminosilicate species produced by the decomposition/dissolution of FAU zeolite to seed crystal surfaces or nuclei is enhanced; consequently, the decomposition/dissolution rate of FAU zeolite increases. It is reasonable to assume that the locally ordered aluminosilicate species produced in the presence of an OSDA other than TEOH contributes to the crystallization of *BEA zeolite if their chemical structures are suitable for the crystal growth. Therefore, we investigated the influence of OSDAs other than TEOH on FAU-*BEA interzeolite conversion in the following experiments.

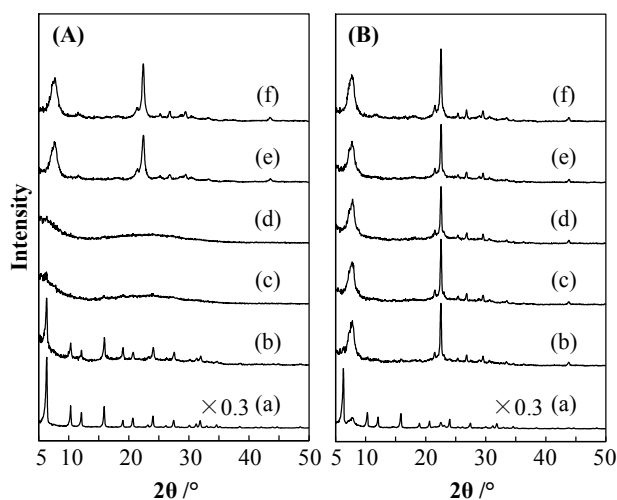


Fig. 2-5. XRD patterns of products obtained from FAU zeolite (Si/Al = 23) in the (A) absence and (B) presence of 33 wt% seed crystals at various crystallization times: (a) 0 h, (b) 2 h, (c) 1 d, (d) 2 d, (e) 3 d, and (f) 7 d.

3.2 Influence of OSDAs on FAU-*BEA interzeolite conversion in the presence of seed crystals

Interzeolite conversion of FAU zeolite was performed in the presence of seed crystals by using several OSDAs such as TMAOH, BTMAOH, and choline hydroxide instead of TEAOH; these OSDAs had already been found to be effective for the synthesis of RUT, CHA, and LEV zeolites from FAU zeolite, respectively [9-11]. As given in Table 2-1 (Run No. 3), when only BTMAOH was used, highly crystalline and pure *BEA zeolite was obtained; in other words, the FAU-*BEA interzeolite conversion effectively proceeded in the presence of seed crystals. The yield and Si/Al ratio of the obtained *BEA zeolite were ca. 70% and 21, respectively. The Si/Al ratio of the product was

Table2-1 Hydrothermal conversion of FAU zeolite using various structure-directing agents (OSDAs) in the presence of seed crystals

Run no.	Synthesis conditons ^a		Product ^b (Si/Al ratio)
	Starting Si & Al sources(Si/Al ratio)	OSDA	
1	FAU(23)	Choline hydroxide	*BEA, Un.
2	FAU(23)	TMAOH	FAU, Am.
3	FAU(23)	BTMAOH	*BEA (21)
4	Nipsil & Al(OH) ₃ (23)	BTMAOH	*BEA, Am.

^aOSDA/SiO₂ = 0.4; Time = 7 days; H₂O/SiO₂ = 10; Temp. = 125 °C;

Seed = 33 wt%; ^bAm. = Amorphous; Un. = Unknown

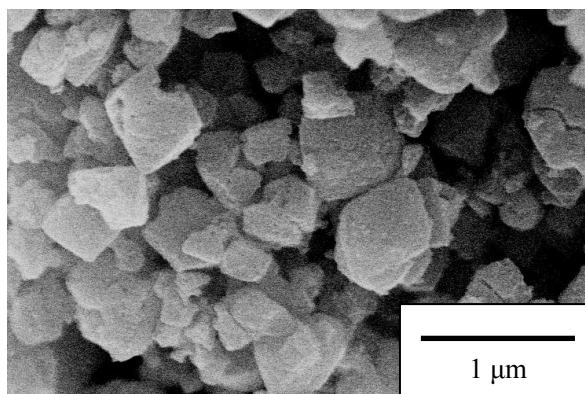


Fig. 2-6. SEM image of *BEA zeolite obtained from FAU zeolite using benzyltrimethylammonium hydroxide (BTMAOH) in the presence of seed crystals.

considerably different from that of seed crystals (Si/Al = 78). To clarify the advantage of FAU-*BEA interzeolite conversion with BTMAOH, we also attempted to synthesize *BEA zeolite from amorphous SiO₂/Al(OH)₃ (Run No. 4). However, pure *BEA zeolite was not obtained, indicating that the locally ordered aluminosilicate species produced by the decomposition/dissolution of FAU zeolite with BTMAOH are also suitable for the crystallization of *BEA zeolite. Figure 2-6 shows the SEM image of *BEA zeolite

obtained with BTMAOH. Since large amounts of seed crystals were employed, seed crystals that did not decompose/dissolve were observed. However, there were many small crystals, which appeared to have been produced by the interzeolite conversion of FAU zeolite.

The ^{29}Si MAS NMR spectra of the as-synthesized *BEA zeolite are shown in Figure 2-7. As compared to the ^{29}Si MAS NMR spectrum of the *BEA zeolite synthesized using TEAOH as an OSDA (Fig. 3), the intensity of the peak at ca. -103 ppm was slightly stronger; moreover, in the CP spectrum of the *BEA zeolite, the peak intensity at ca. -103 ppm was enhanced. The degree of enhancement was relatively larger than that of the *BEA zeolite synthesized using TEAOH, indicating more structural defects.

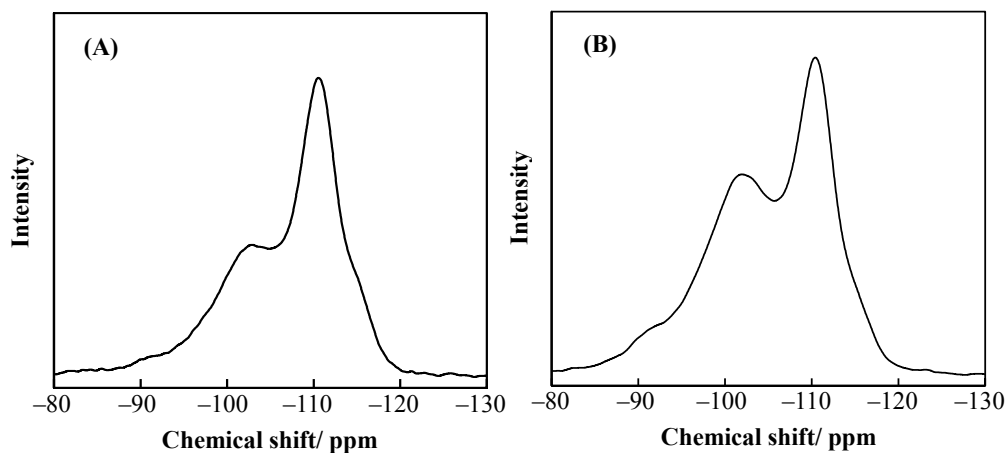


Fig. 2-7. ^{29}Si MAS NMR spectra measured (A) without and (B) with CP for as-synthesized *BEA zeolite using BTMAOH in the presence of 33 wt% seed crystals.

I do not have adequate information concerning the difference at the present time. The ^{27}Al MAS NMR spectrum showed only one peak corresponding to tetrahedrally coordinated framework aluminum species at ca. 54 ppm (not shown). This implies that all the aluminum species present in the *BEA zeolite obtained by the interzeolite

conversion of the starting FAU zeolite in the presence of BTMAOH also existed within the zeolite framework.

The characteristics of the organic molecules occluded in the zeolitic pores of *BEA zeolite were investigated by ^{13}C CP/MAS NMR and thermal analysis. From Figure 2-8, the ^{13}C CP/MAS NMR spectrum consists of three resonances centered at ca. 53, 72, and 130 ppm, which are assigned to the methyl carbon, methylene carbon, and phenyl carbon of the BTMA cation, respectively. This implies that BTMA cation was the only organic species existing in the *BEA zeolite pores. From the TG curve (not shown), the amount of BTMA cations was calculated to be ca. 16 wt%, implying the presence of ca. 5 BTMA cations/u.c. Figure 2-9 shows the nitrogen adsorption isotherm of the calcined *BEA zeolite obtained using BTMAOH. For comparison, the nitrogen adsorption isotherm of the *BEA zeolite obtained using TEAOH is also shown. Both nitrogen adsorption isotherms showed a type I. The BET surface area and micropore volume of the *BEA zeolite obtained using BTMAOH and TEAOH were calculated to be $650\text{ m}^2\text{g}^{-1}$ and $0.25\text{ cm}^3\text{g}^{-1}$, respectively, and $670\text{ m}^2\text{g}^{-1}$ and $0.26\text{ cm}^3\text{g}^{-1}$, respectively. Their values were very similar to those of the *BEA zeolite synthesized using TEAOH in the absence of seed crystals ($680\text{ m}^2\text{g}^{-1}$ and $0.27\text{ cm}^3\text{g}^{-1}$).

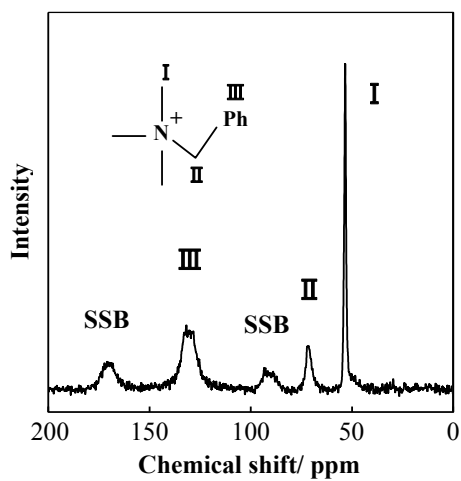


Fig. 2-8. ^{13}C CP/MAS NMR spectrum of *BEA zeolite obtained from FAU zeolite using BTMAOH in the presence of 33 wt% seed crystals.

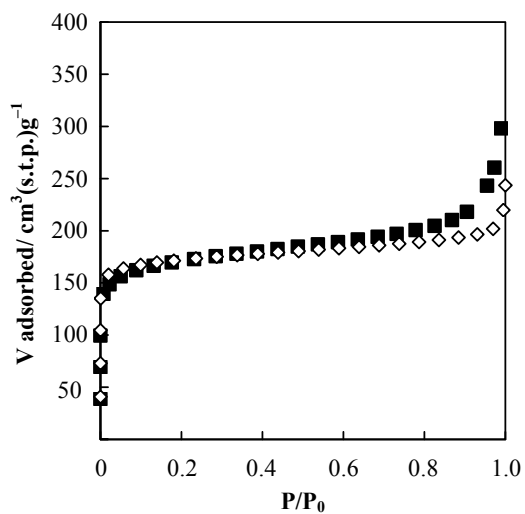


Fig. 2-9. Nitrogen adsorption isotherms of calcined *BEA zeolites obtained using \diamond : TEOH and \blacksquare : BTMAOH.

3.3 OSDA-free synthesis of *BEA zeolite from FAU zeolite

All the above results strongly suggest that it is possible to synthesize *BEA zeolite using seed crystals in the absence of OSDA if the starting FAU zeolite is decomposed/dissolved to locally ordered aluminosilicate species, whose chemical structures are suitable for the crystallization of *BEA zeolite. Therefore, I applied the interzeolite conversion method to the OSDA-free synthesis of *BEA zeolite. According to the results reported by Majano et al. [24], non-calcined *BEA zeolites can be used as seed crystals; the crystals were synthesized from amorphous Nipsil $\text{SiO}_2/\gamma\text{-Al}_2\text{O}_3$ using TEAOH as a OSDA. The Si/Al ratio of the *BEA zeolite seed crystals was 25. The BET surface area and micropore volume were $680 \text{ m}^2 \text{ g}^{-1}$ and $0.28 \text{ cm}^3 \text{ g}^{-1}$, respectively.

Detailed synthesis conditions are listed in Table 2-2. First, I investigated the influence of the NaOH/SiO₂ ratio at the low hydrothermal temperature of 100 °C. When the NaOH/SiO₂ ratio was below 0.4, the amorphous phase was observed along with the *BEA phase (Run Nos. 5 and 6). On the other hand, at higher NaOH/SiO₂ ratios (>0.8), GIS and FAU phases were observed as by-products (Run No. 8). Highly crystalline and pure *BEA zeolite was obtained only with the NaOH/SiO₂ ratio of 0.6 (Run No. 7). To our knowledge, this is the first report of FAU-*BEA interzeolite conversion at the low temperature of 100 °C; however, the yield was ca. 12%. The lower yield is probably due to the high alkalinity of the interzeolite conversion condition. For comparison, I attempted to synthesize *BEA zeolite by the conventional hydrothermal synthesis using Cab-o-sil M-5/NaAlO₂ as the starting materials (Run No. 9). Although *BEA zeolite was obtained, the yield was considerably smaller (ca. 4%), thereby indicating the advantage of the interzeolite conversion method.

Table2-2 Synthesis conditions and characteristics of *BEA zeolites obtained from FAU zeolite in the absence of organic SDAs (OSDAs)

Run no.	Synthesis conditions						Product			
	Starting Si & Al sources (Si/Al)	NaOH/SiO ₂	H ₂ O/SiO ₂	Seed level (wt%)	Temp. (°C)	Time (h)	Phase ^a	Yield (%)	BET surface area (m ² g ⁻¹)	Si/Al
5	FAU (22)	0.2	10	9.1	100	24	*BEA, Am.	-		
6	FAU (22)	0.4	10	9.1	100	24	*BEA, Am.	-		
7	FAU (22)	0.6	10	9.1	100	24	*BEA	12	540	7.3
8	FAU (22)	0.8	10	9.1	100	24	*BEA, GIS, FAU	-		
9	Cab-o-sil M-5 & NaAlO ₂ (22)	0.6	10	9.1	100	24	*BEA	4		
10	FAU (16)	0.6	10	9.1	100	24	*BEA, Am.	-		
11	FAU (42)	0.6	10	9.1	100	24	*BEA	4		
12	FAU (22)	0.6	10	9.1	125	24	*BEA, MOR	-		
13	FAU (22)	0.6	10	16.7	125	24	*BEA, GIS	-		
14	FAU (22)	0.6	10	33.3	125	24	*BEA	16		
15	FAU (22)	0.6	20	33.3	125	24	*BEA	26	650	11
16	FAU (22)	0.6	20	33.3	125	48	*BEA	16	710	11
17	FAU (22)	0.6 (LiOH)	20	33.3	125	24	*BEA, Am.	-		
18	FAU (22)	0.6 (KOH)	20	33.3	125	24	*BEA	34	460	11
19	FAU (22)	0.6 (RbOH)	20	33.3	125	24	*BEA, Am.	-		
20	FAU (22)	0.6 (CsOH)	20	33.3	125	24	*BEA, Am.	-		

^aAm. = amorphous

Figure 2-10 shows the XRD patterns for the FAU-*BEA interzeolite conversion process. It is clear that the FAU zeolite decomposed completely after hydrothermal treatment for 2 h. The intensities of the peaks corresponding to the *BEA zeolite increased with the hydrothermal treatment time, indicating the crystal growth of *BEA zeolite.

Sano et al. already reported that the interzeolite conversion was strongly dependent on the Si/Al ratio of the starting zeolite [9–12]. In order to study the influence of the Si/Al ratio of the starting FAU zeolite on OSDA-free FAU-*BEA interzeolite conversions, FAU zeolites with several Si/Al ratios were prepared by dealumination treatment and

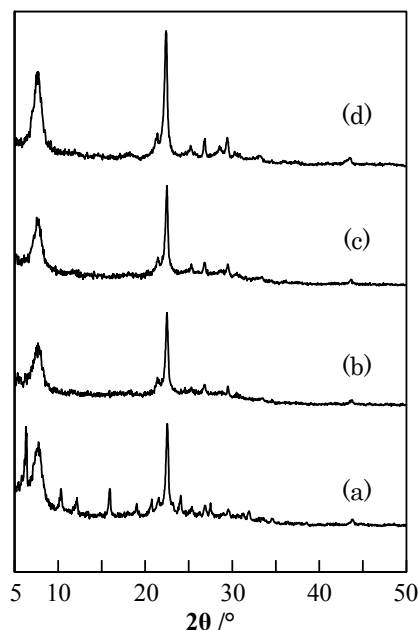


Fig. 2-10. XRD patterns of products obtained from FAU zeolite using NaOH and 9.1 wt% seed crystals at various crystallization times: (a) 0 h, (b) 2 h, (c) 12 h, and (d) 24 h.

subjected to hydrothermal treatment. For the FAU zeolite with an Si/Al ratio of 16, the interzeolite conversion did not proceed (Run No. 10). However for the Si/Al ratio of 42, pure *BEA zeolite was obtained, although the yield (ca. 4%) was very low (Run No. 11).

Therefore, to improve the *BEA zeolite yield, the interzeolite conversion of FAU zeolite was performed at the higher temperature of 125 °C. The seed crystal content was also increased from 9.1 wt% to 16.7 or 33.3 wt%. Although MOR and GIS zeolites were obtained as by-products when 9.1 and 16.7 wt% seed crystals were added (Run Nos. 12 and 13), pure *BEA zeolite with a higher yield of 16% was obtained using 33.3 wt% seed crystals (Run No. 14). However, it is possible to consider that the enhancement in the yield is due to a large amount of non-calcined seed crystals that contain TEA cations in the zeolite pores. To verify this possibility, hydrothermal treatments of FAU zeolite were performed using both calcined seed crystals and a certain amount of TEAOH,

which was determined by the TG analysis of non-calcined seed crystals. However, *BEA zeolite was not obtained. Taking into account the fact that when calcined and non-calcined *BEA seed crystals (0.25 g) were treated with a 1.6 M NaOH aqueous solution (3.0 cm³) at 125 °C for 2 h, a large different in hydrothermal stability was observed, namely non-calcined seed crystals did not decompose/dissolve, it proves that TEA cation containing *BEA seed crystals are more stable and consequently the crystal surfaces contribute to the crystal growth of *BEA zeolite.

I then studied the influence of H₂O/SiO₂ ratio. For an H₂O/SiO₂ ratio of 20, the yield increased to 26% (Run No. 15). Although the exact reason for such an increase is not clarified, we suggest that this is probably due to an increase in the solubility of locally ordered aluminosilicate species produced by the decomposition/dissolution of FAU zeolite. Prolonged synthesis times were not necessarily effective for the crystallization of *BEA zeolite (Run No. 16).

Finally, I investigated the influence of various types of alkaline metal cations. As shown in Table 2, when KOH was employed instead of NaOH as an alkali source, pure *BEA zeolite with a high yield of 34% (Run No. 18) was obtained. Furthermore, LiOH, RbOH, and CsOH did not yield pure *BEA zeolite phase (Run Nos. 17, 19, and 20, respectively). Although I do not have enough data to explain the difference, I am now speculating as follows. Smaller cations such as Na⁺ and K⁺ cations act as structure-forming cations, whereas larger cations such as Ru⁺ and Cs⁺ cations act as structure-breaking cations [29]. At the present time, however, I could not explain the less structure-forming ability of Li⁺ cation.

Figure 2-11 shows the SEM images of seed crystals and *BEA zeolites obtained using NaOH and KOH. The crystal size of the *BEA zeolite obtained using NaOH was larger

than that of seed crystals, and the surfaces were covered with small crystals (ca. 50 nm), suggesting crystal growth on the outer surfaces of seed crystals. On the other hand, in the SEM image of the *BEA zeolite obtained using KOH, two kinds of crystals, ca. 100 nm and ca. 500 nm, were observed. The larger crystals appeared to be seed crystals, and most of the smaller crystals were separated from the larger ones. However, an SEM image at high magnification showed that several small crystals were linked to the large crystals, which suggests that the smaller crystals were crystallized from the outer surfaces of the larger seed crystals. Currently, I do not have adequate information regarding the differences in the interzeolite conversion behaviors when NaOH and KOH are used as the alkali sources.

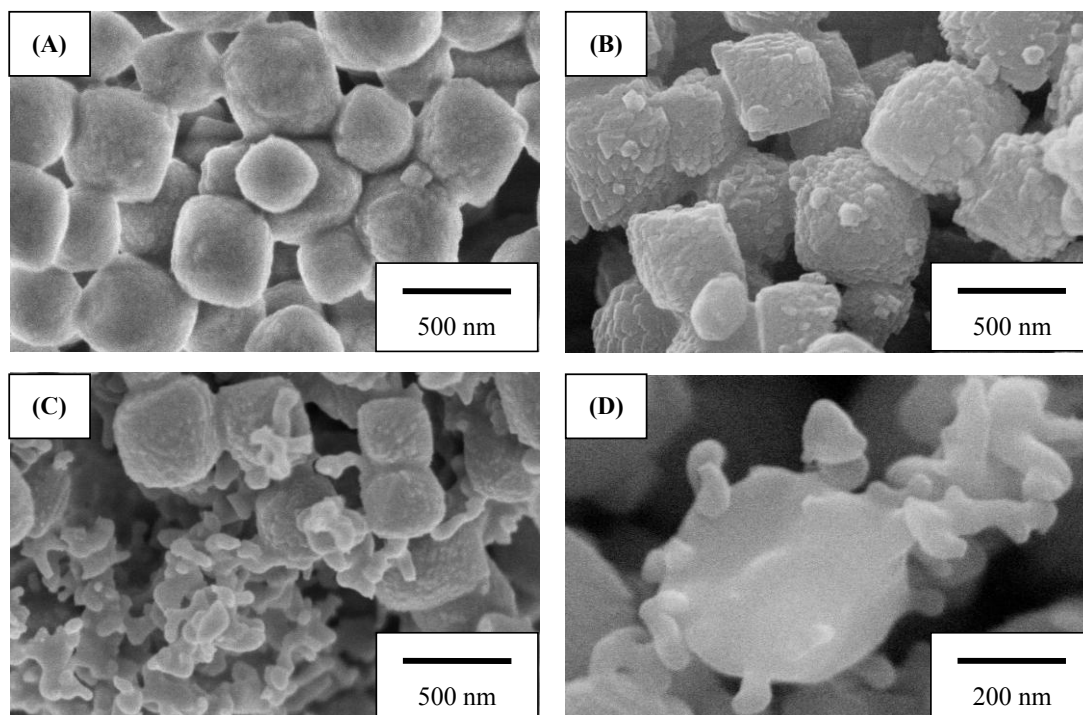


Fig. 2-11. SEM images of (A) *BEA zeolite seed crystals, (B) *BEA zeolite obtained using NaOH, (C) *BEA zeolite using KOH, and (D) high magnification of (C).

The chemical states of aluminum in the obtained *BEA zeolites were investigated by ^{27}Al MAS NMR. The ^{27}Al MAS NMR spectra of the *BEA zeolites obtained using both NaOH and KOH exhibited only one peak corresponding to tetrahedrally coordinated aluminum species at ca. 54 ppm (not shown). A peak corresponding to octahedrally coordinated aluminum species was not observed around 0 ppm. Therefore, it was found that all the aluminum species present in both the *BEA zeolites obtained by the interzeolite conversion in the absence of OSDAs also existed within the zeolite framework.

4. Conclusions

FAU-*BEA interzeolite conversions were investigated in the presence of seed crystals under various synthesis conditions. The crystallization rate of *BEA zeolite during the interzeolite conversion of FAU zeolite was significantly enhanced in the presence of seed crystals. *BEA zeolite was obtained only after hydrothermal treatment time for 2 h at 125 °C in the presence of TEAOH and 33 wt% seed crystals.

Moreover, *BEA zeolite could be synthesized by using BTMAOH in place of TEAOH; however, BTMAOH is not effective for FAU-*BEA zeolite conversions in the absence of seed crystals. Therefore, it was concluded that the locally ordered aluminosilicate species produced by the decomposition/dissolution of FAU zeolite with BTMAOH are suitable for the crystallization of *BEA zeolite in the presence of seed crystals.

On a basis of these results, OSDA-free FAU-*BEA interzeolite conversions were investigated in the presence of seed crystals. Consequently, I succeeded in interzeolite conversion of FAU zeolite into BEA zeolite in the absence of OSDAs at low

temperature. To my knowledge, this is the first report on OSDA-free FAU-*BEA interzeolite conversions. Furthermore, when KOH was employed instead of NaOH, ca. 34% yield of *BEA zeolite was achieved.

Above results suggest that these zeolite formation processes via such interzeolite conversions are more efficient with enhanced crystallization rates. Moreover, the possibility and potential of OSDA-free conversions have also been shown.

References

- [1] B. Subotić, D. Škrtić, I. Šmit, L. Sekovanić, *J. Cryst. Growth* 50 (1980) 498.
- [2] B. Subotić, L. Sekovanić, *J. Cryst. Growth* 75 (1986) 561.
- [3] B. Subotić, I. Šmit, O. Madžija, L. Sekovanić, *Zeolites* 2 (1982) 135.
- [4] S. I. Zones, *J. Chem. Soc. Faraday Trans.* 87 (1991) 3709.
- [5] S. I. Zones, L. T. Yuen, Y. Nakagawa, R. A. van Nordstrand, S. D. Toto, in: R. von Ballmoos, J. B. Higgins, M. M. J. Treacy (Eds.), *Proceedings of the ninth International Conference*, Butterworth-Heinemann, Boston, 1993, p. 163.
- [6] S. I. Zones, Y. Nakagawa, *Micropor. Mater.* 2 (1994) 543.
- [7] Y. Kubota, H. Maekawa, S. Miyata, T. Tatsumi, Y. Sugi, *Micropor. Mesopor. Mater.* 101 (2007) 115.
- [8] R. K. Ahedi, Y. Kubota, Y. Sugi, *J. Mater. Chem.* 11 (2001) 2922.
- [9] H. Jon, S. Takahashi, H. Sasaki, Y. Oumi, T. Sano, *Micropor. Mesopor. Mater.* 113 (2008) 56.
- [10] M. Itakura, T. Inoue, A. Takahashi, T. Fujitani, Y. Oumi, T. Sano, *Chem. Lett.* 37 (2008) 908.
- [11] T. Inoue, M. Itakura, H. Jon, Y. Oumi, A. Takahashi, T. Fujitani, T. Sano, *Micropor. Mesopor. Mater.* 122 (2009) 149.
- [12] H. Jon, K. Nakahata, B. Lu, Y. Oumi, T. Sano, *Micropor. Mesopor. Mater.* 96 (2006) 72.
- [13] H. Jon, N. Ikawa, Y. Oumi, T. Sano, *Chem. Mater.* 20 (2008) 4135.
- [14] G. T. Kerr, *J. Phys. Chem.* 70 (1966) 1047.
- [15] G. T. Kerr, *J. Phys. Chem.* 72 (1968) 1385.
- [16] J. Warzywoda, R. W. Thompson, *Zeolites* 11 (1991) 577.

- [17] B. Lu, T. Tsuda, Y. Oumi, K. Itabashi, T. Sano, *Micropor. Mesopor. Mater.* 76 (2004) 1.
- [18] C. S. Cundy, P. A. Cox, *Micropor. Mesopor. Mater.* 82 (2005) 1.
- [19] C. S. Cundy, J. O. Forrest, in: *Zeolites and mesoporous materials at dawn of the 21st century*. A. Galarneau, F. Di Renzo, F. Fajula, J. Védrine (Eds), *Stud. Surf. Sci. Catal.* 135 (2000) 192.
- [20] K. Nishi, R. W. Thompson, in: *Handbook of Porous Solid*, K. Schüth, S. W. Sing, J. Weitkamp, (Eds.), WILEY-VCH, Germany, vol. 2, 2002, p. 736.
- [21] J. Song, L. Dai, Y. Ji, F.-S. Xiao, *Chem. Mater.* 18 (2006) 2775.
- [22] Z. Wu, J. Song, Y. Ji, L. Ren, F.-S. Xiao. *Chem. Mater.* 20 (2008) 357.
- [23] B. Xie, J. Song, L. Ren, Y. Ji, J. Li, F.-S. Xiao. *Chem. Mater.* 20 (2008) 4533.
- [24] G. Majano, L. Delmotte, V. Valtchev, S. Mintova, *Chem. Mater.* 21 (2009) 4184.
- [25] Y. Kamimura, W. Chaikittisilp, K. Itabashi, A. Shimojima, T. Okubo, *Chem. Asian J.* 5 (2010) 2182.
- [26] T. Yokoi, M. Yoshioka, H. Imai, T. Tatsumi, *Angew. Chem. Int. Ed.* 48 (2009) 9884.
- [27] K. Iyoki, Y. Kamimura, K. Itabashi, A. Shimojima, T. Okubo, *Chem. Lett.* 39 (2010) 730.
- [28] P. Wu, T. Komatsu, T. Yashima, *J. Phys. Chem.* 99 (1995) 10923.
- [29] Z. Gabelica, N. Blom, E.G. Derouane, *Appl. Catal.* 5 (1983) 227.

Chapter 3

Hydrothermal conversion of FAU zeolite into LEV zeolite in the presence of non-calcined seed crystals

1. Introduction

Conventional zeolite synthesis utilizes the hydrothermal treatment of amorphous aluminosilicate gel as a starting material, in the presence of organic structure-directing agents (OSDAs). The use of OSDAs is, however, undesirable from a practical point of view because of their high cost as well as the high environmental impact. As a consequence of these drawbacks, the synthesis of zeolites from seed crystals without the use of OSDAs has attracted considerable attention, and several research groups have already succeeded in the OSDA-free synthesis of ECR-1 [1], ZSM-34 [2], *BEA [3–5], RTH [6], and ZSM-12 [7] zeolites.

In the synthesis of most zeolites, an amorphous phase is converted directly to a given type of zeolite; however, the transformation is usually gradual and has the following sequence: amorphous phase → less stable zeolite → most stable zeolite. On this basis, several research groups have pointed out the high potential of an alternative method for zeolite formation, i.e., the hydrothermal conversion of one zeolite type into another (interzeolite conversion)[8–10].

Recently, Sano et al. have also investigated the potential of interzeolite conversion, and succeeded in the synthesis of several types of zeolites such as *BEA, RUT, CHA,

LEV, MTN, and OFF using FAU zeolite as the starting material, in the presence of various OSDAs [11–16]. Among the zeolites synthesized, LEV zeolite, which belongs to the chabazite (CHA) zeolite group, has attracted considerable interest because of its structure with eight-membered ring pores ($4.8 \times 3.6 \text{ \AA}$) and because it shows a shape specific selectivity for the conversion of methanol or ethanol into light olefins such as ethylene and propylene. The use of FAU zeolite as a starting material for the preparation of other zeolites, in the presence of the structure directing agent choline hydroxide, results in a crystallization rate that is superior to that achieved by the conventional synthesis using aluminosilicate gel as the starting material. This enhanced crystallization rate arises because the decomposition/dissolution of the starting zeolite generates locally ordered aluminosilicate species (nanoparts) that assemble and evolve into another type of zeolite.

In addition to the successful interzeolitic conversions achieved using OSDAs, I very recently succeeded in the FAU-*BEA interzeolite conversion using non-calcined seed crystals. Although the seed crystals employed contained OSDA cations in the zeolitic pores, no additional OSDA was added into the starting gel [17]. Taking into account the fact that LEV and FAU zeolites have similar composite building units, it is possible to synthesize LEV zeolite using non-calcined seed crystals, without the use of an additional OSDA, if the starting FAU zeolite is decomposed/dissolved into locally ordered aluminosilicate species whose chemical structures are suitable for the crystallization of LEV zeolite (Figure 3-1). Therefore, I applied the interzeolite conversion method to the OSDA-free synthesis of LEV zeolite. To my knowledge, this is the first report on hydrothermal synthesis of LEV zeolite from FAU zeolite in the presence of seed crystals without the use of additional OSDA. The LEV zeolite

so-obtained has a unique core/shell structure.

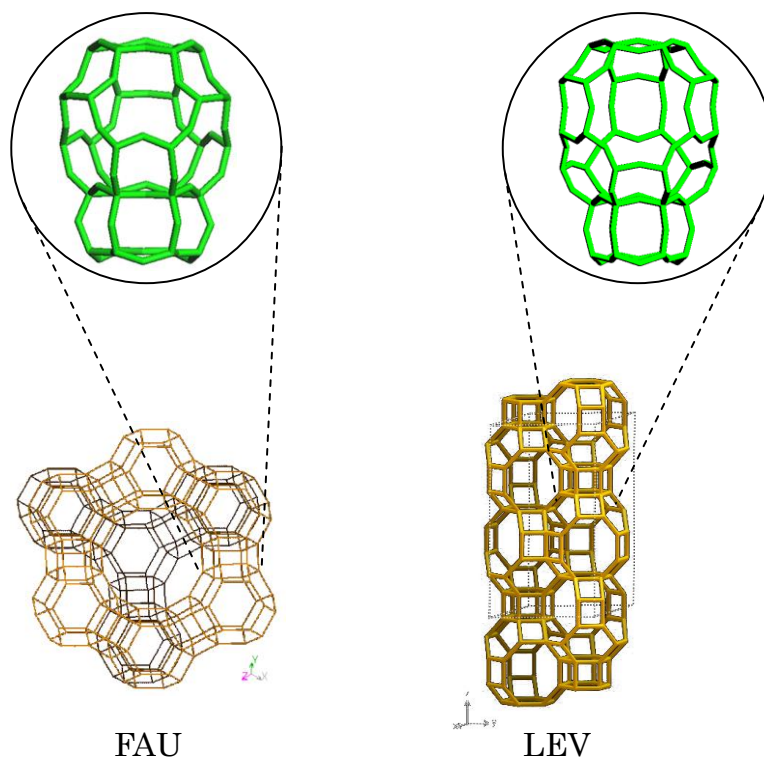


Fig. 3-1 Framework structures of FAU and LEV zeolites.

2. Experimental

2.1 Synthesis of LEV zeolite

Starting FAU zeolites with various Si/Al ratios were prepared from NH₄-Y zeolite (Si/Al = 2.8, Tosoh Co., Japan) using a dealumination treatment involving a combination of steaming at 700 °C and treatment with H₂SO₄ (0.74 M) at 75 °C for 4 h. The SEM image of the dealuminated FAU zeolite is shown in Figure 3-2A. The particle size of the dealuminated FAU zeolite was 200–600 nm. The formation of mesopores

upon dealumination was confirmed. Hydrothermal conversion of FAU zeolite into LEV zeolite was carried out by adding the dealuminated FAU zeolite to an aqueous solution of MOH (M: alkaline metal). Due to the fact that GIS zeolite was obtained in the absence of the non-calcined seed crystals of LEV zeolite, 5–17 wt% (based on silica) of non-calcined seed crystals (Si/Al = 10.7) was added to the starting gel. The non-calcined seed crystals were synthesized from FAU zeolite using choline hydroxide as a OSDA according to the method used in the previous report [16]. Although the calcined seed crystals having no choline cations in the zeolitic pores also yield pure LEV zeolite, the reproducibility was very low, which suggests that the quality of the seed crystals employed is a crucial factor in the FAU–LEV interzeolite conversion without the use of OSDA. Therefore, subsequent experiments were carried out with the addition of non-calcined seed crystals to the starting gel. The mixture was placed into a 30 cm³ Teflon-lined stainless steel autoclave. Hydrothermal conversion was conducted at 125 °C for 24–72 h in a convection oven. The solid product was collected by centrifugation and washed thoroughly with deionized water until the pH was near neutral, followed by drying overnight at 70 °C.

2.2 Characterization

X-ray diffraction (XRD) patterns of the solid products were collected using a powder X-ray diffractometer (Bruker, D8 Advance) with graphite monochromatized Cu K α radiation at 40 kV and 30 mA. The Si/Al ratios were determined by X-ray fluorescence (XRF, Philips PW 2400). 0.5 g of a sample was fused with 5 g of dilithium tetraborate (Li₂B₄O₇) at 1100 °C. The Si/Al ratio was calculated from the Si and Al concentrations as determined from the corresponding calibration curves that were prepared using high

purity SiO_2 (99.9995 %) and $\gamma\text{-Al}_2\text{O}_3$ (99.999 %). The crystal morphology was observed by scanning electron microscopy (SEM, Hitachi S-4800). Thermal analysis was performed using a TG/DTA apparatus (SSC/5200 Seiko Instruments). The sample (ca. 7 mg) was heated from room temperature to 800 °C in a flow of air (50 mL min^{-1}), at a rate of $5 \text{ }^\circ\text{C min}^{-1}$. ^{13}C cross polarized magic angle spinning nuclear magnetic resonance (CP/MAS NMR), ^{27}Al MAS NMR, and ^{29}Si MAS NMR spectra were recorded at 100.6 MHz, 104.3 MHz, and 79.5 MHz, respectively, on a Bruker Avance DRX-400 NMR spectrometer, using a 7 mm diameter zirconia rotor. The rotor was spun at 4 kHz for ^{13}C CP/MAS and ^{29}Si MAS NMR, and at 6 kHz for ^{27}Al MAS NMR. The spectra were acquired using 6.0 μs pulses, a 25 s recycle delay, and 1000 scans for ^{13}C CP/MAS NMR, 2.3 μs , 1 s and 1000 scans for ^{27}Al MAS NMR, and 5 μs , 20 s and 2000 scans for ^{29}Si MAS NMR. $\text{Al}(\text{NO}_3)_3 \cdot 9\text{H}_2\text{O}$ was used as a chemical shift reference for ^{27}Al MAS NMR and $\text{Si}(\text{CH}_3)_4$ was used as a chemical shift reference for ^{13}C CP/MAS NMR and ^{29}Si MAS NMR. Prior to the ^{27}Al MAS NMR measurements, the samples were moisture-equilibrated over a saturated solution of NH_4Cl for 24 h. Nitrogen adsorption isotherms at $-196 \text{ }^\circ\text{C}$ were obtained using a conventional volumetric apparatus (Bel Japan, BELSORP 28SA). Prior to the adsorption measurements, the calcined samples (ca. 0.1 g) were evacuated at 400 °C for 10 h.

3. Results and discussion

Initially, the influence of alkaline metal cations on the product obtained from the hydrothermal conversion of FAU zeolite in the presence of non-calcined seed crystals (without additional OSDA) was investigated by several preliminary experiments which were carried using various alkaline metal hydroxides as an alkali source (Table 3-1,

Sample nos. 1–5). Pure LEV zeolite was only obtained in the presence of the Na^+ cation. Therefore, subsequent experiments were carried out using NaOH as the alkali source. Detailed synthesis conditions are listed in Table 3-1. Investigation of the effect of the alkalinity (OH^-/SiO_2) of the starting gel on the product showed that at a NaOH/SiO_2 ratio of 0.4, an amorphous phase was observed along with the LEV phase (Sample no. 6); and for a NaOH/SiO_2 ratio of 0.8, a co-existing unidentified phase was observed along with the LEV phase (Sample no. 7). Pure LEV zeolite was obtained only at a NaOH/SiO_2 ratio of 0.6 although the yield was low (12%) (Sample no. 2). The hydrothermal conversion of FAU zeolite into LEV zeolite was also dependent upon the $\text{H}_2\text{O}/\text{SiO}_2$ ratio of the starting gel. Pure LEV zeolite was obtained only with $\text{H}_2\text{O}/\text{SiO}_2$ ratios in the range of 15–20 (Sample nos. 2 and 9). The yield of LEV zeolite increased slightly with hydrothermal treatment time (Sample no. 11). Figure 3-2 shows the XRD patterns of the starting FAU zeolite and the obtained LEV zeolite. The diffraction pattern of the product is typical of LEV zeolite and contains no impurity peaks from unconverted starting FAU zeolite or co-crystallized phases. Decreasing the seed crystal content from 16.7 to 4.8 wt%, resulted in a decrease in the yield (Sample no. 13). For comparative purposes, the synthesis of LEV zeolite by the conventional hydrothermal method, using amorphous $\text{SiO}_2/\text{Al}(\text{OH})_3$ as the starting material in the presence of non-calcined seed crystals, was attempted. However, MOR zeolite was obtained as the major product (Sample no. 19), indicating the advantage of the interzeolite conversion method for the production of pure LEV zeolite.

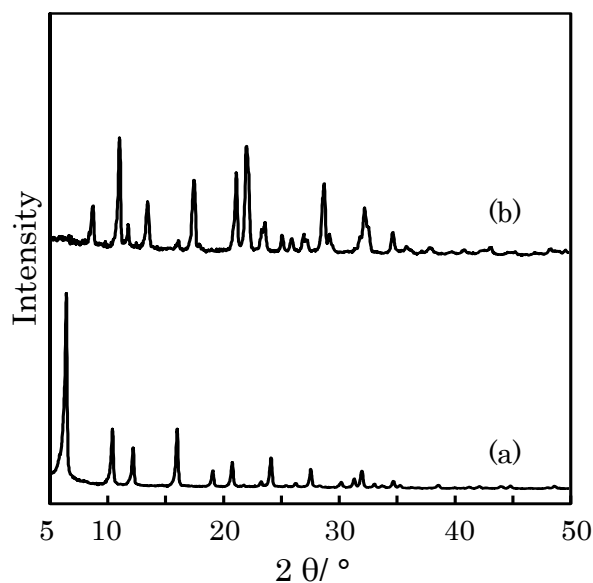


Fig. 3-2 XRD patterns of (a) starting FAU zeolite and (b) LEV zeolite obtained from the FAU zeolite (Sample no. 11).

Previous studies undertaken by Sano's group indicated that interzeolite conversion was strongly dependent on the Si/Al ratio of the starting FAU zeolite [12–18]. The influence of the Si/Al ratio of the starting FAU zeolite on LEV zeolite synthesis was, therefore, investigated herein using FAU zeolites with various Si/Al ratios (Si/Al = 4–37), which were prepared by dealumination treatment and were subjected to hydrothermal treatment. The results presented in Table 3-1 (Sample nos. 2, 9, 11, 13, 14, and 17), indicate that FAU zeolites with Si/Al ratios in the range of 19–26 could be converted into pure LEV zeolites by employing synthesis times of 1–3 days. Relative to the other samples within this range which gave yields of 11–18%, when the FAU zeolite with a Si/Al ratio of 19 was used, the yield of LEV zeolite increased to ca.26% (Sample no.17).

Table 3-1 Synthesis conditions and characteristics of LEV zeolites obtained by hydrothermal conversion of FAU zeolite in the presence of non-calcined seed crystals without the use of additional OSDA.

Sample no.	Synthesis conditions							Product		
	Starting Si& Al source(Si/Al)	MOH /SiO ₂	M	H ₂ O /SiO ₂	Seed (wt%)	Temp. (°C)	Time (day)	Phase ^a	Yield ^b (%)	Bulk Si/Al
1	FAU(25)	0.6	Li	15	16.7	125	1	LEV, Am.		
2	FAU(25)	0.6	Na	15	16.7	125	1	LEV	12	5.5
3	FAU(25)	0.6	K	15	16.7	125	1	OFF, ERI		
4	FAU(25)	0.6	Rb	15	16.7	125	1	OFF, ERI		
5	FAU(25)	0.6	Cs	15	16.7	125	1	Am. (LEV)		
6	FAU(25)	0.4	Na	15	16.7	125	1	LEV, Am.		
7	FAU(24)	0.8	Na	15	16.7	125	1	LEV, Un.		
8	FAU(26)	0.6	Na	10	16.7	125	1	LEV, Un.		
9	FAU(26)	0.6	Na	20	16.7	125	1	LEV	18	6.0
10	FAU(25)	0.6	Na	30	16.7	125	1	LEV, Am.		
11	FAU(25)	0.6	Na	15	16.7	125	3	LEV	18	5.3
12	FAU(25)	0.6	Na	15	16.7	125	5	LEV, MOR		
13	FAU(25)	0.6	Na	15	4.8	125	3	LEV	11	4.6
14	FAU(24)	0.6	Na	15	16.7	110	3	LEV	16	5.4
15	FAU(24)	0.6	Na	15	16.7	140	3	MOR, LEV		
16	FAU(4)	0.6	Na	15	16.7	125	3	GIS, Un.		
17	FAU(19)	0.6	Na	15	16.7	125	3	LEV	26	4.9
18	FAU(37)	0.6	Na	15	16.7	125	3	LEV, MOR		
19	SiO ₂ &Al(OH) ₃ (25)	0.6	Na	15	16.7	125	3	MOR, LEV		

^a Am.=Amorphous, Un.=Unknown

$$^b \text{Yield (\%)} = \frac{\text{Product (g)} - \text{Seeds (g)}}{\text{Starting Si\&Al sources}} \times 100$$

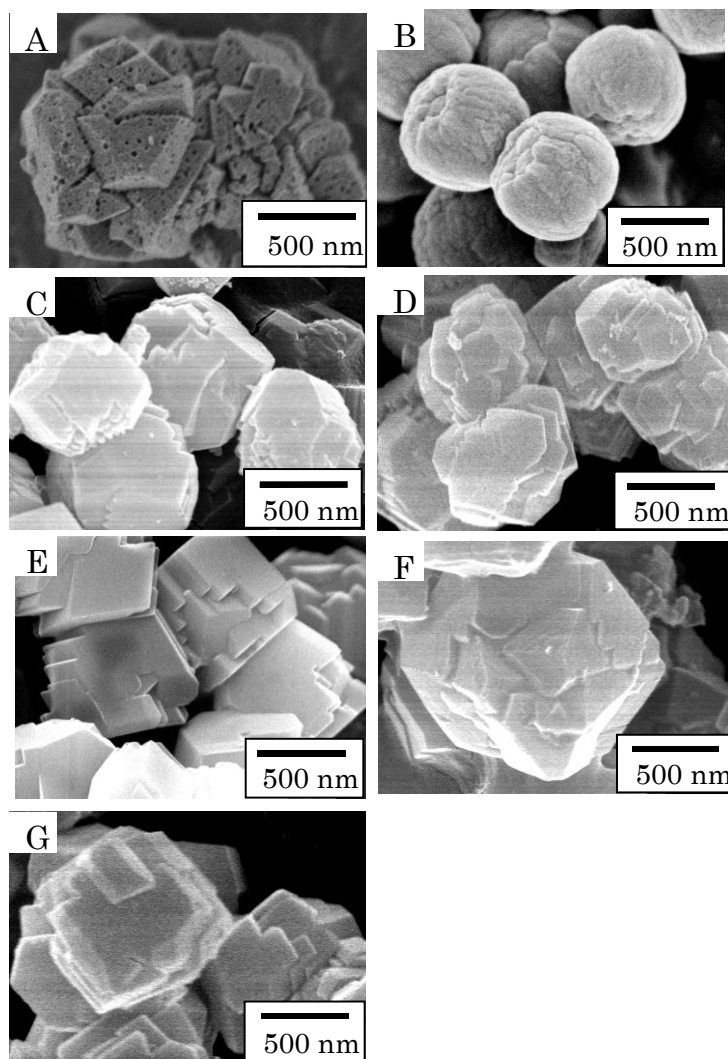


Fig. 3-3 SEM images of (A) FAU zeolite, (B) seed crystals and (C–G) LEV zeolites obtained from FAU zeolite (C: Sample no. 2, D: Sample no. 9, E: Sample no. 11, F: Sample no. 13, G: Sample no. 17).

Figure 3-3 shows the SEM images of the seed crystals employed in the synthesis and the LEV zeolites obtained by hydrothermal conversion of the FAU zeolites (Sample nos. 2, 9, 11, 13, and 17). The seed crystals exhibited a round shape with an average diameter of approximately 500 nm (Fig. 3 B). However, the obtained LEV zeolite crystals had an angular shape as observed in Figs. 3 C–G. No crystals of the starting

FAU zeolite or impurity crystals were observed in the samples. The crystal size of the LEV zeolite was larger than that of the seed crystals and increased with the synthesis time (Figs. 3 C and E). The bulk Si/Al ratio (5.3) of the product was considerably lower than that of the starting FAU zeolite (25), probably as a result of the highly alkaline conversion conditions. The crystal size of LEV zeolite, which was obtained using 4.8 wt% seed crystals, was larger than that obtained using 16.7 wt% seed crystals (Figs. 3 E and F). These results strongly indicate that the crystal growth of LEV zeolite takes place on the crystal surfaces of the seed crystals.

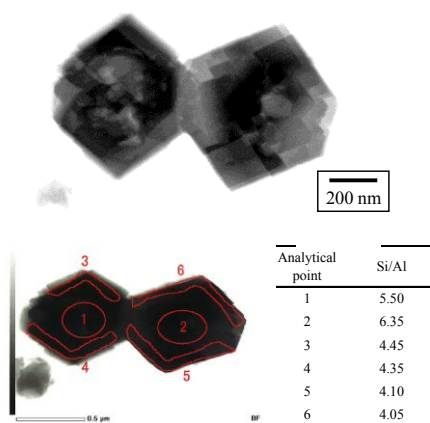


Fig. 3-4 TEM/EDX analysis of LEV zeolite crystals obtained from FAU zeolite (Sample no. 11).

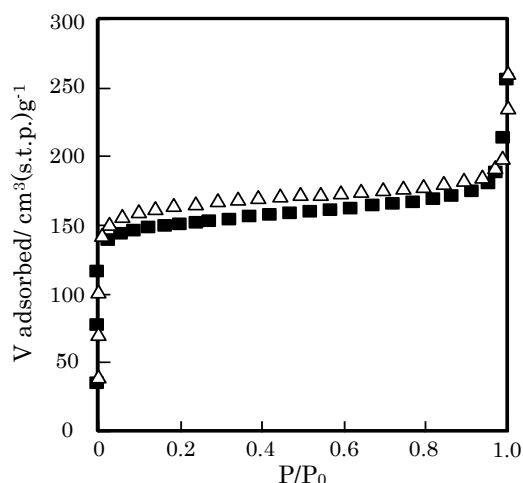


Fig. 3-5 Nitrogen adsorption isotherms of calcined (Δ) seed crystals and (\blacksquare) LEV zeolite obtained from FAU zeolite (Sample no. 11).

Figure 3-4 displays the typical results of TEM/EDX analysis of the LEV zeolite crystals, which were obtained from the conversion of FAU zeolite (Sample no. 11). The TEM image shows the presence of smaller crystals within the larger crystals of LEV zeolite, indicating that the LEV zeolite possesses a peculiar core/shell structure. The smaller crystals are possibly partially decomposed/dissolved seed crystals. The EDX analysis revealed that the Si/Al ratio of the shell (4.1–4.4) was lower than that of the

core (5.5–6.4), i.e., a thin Al-rich shell is wrapped around the core. The Al-rich shell is considered to be fabricated from the aluminosilicate species produced by the decomposition/dissolution of the FAU zeolite with a Si/Al ratio of 25. The nitrogen adsorption isotherm of the calcined LEV zeolite can be classified as type I based on the IUPAC classification, as shown in Figure 3-5, and the BET surface area and micropore volume were calculated to be $530 \text{ m}^2\text{g}^{-1}$ and $0.27 \text{ cm}^3\text{g}^{-1}$, respectively. These values were similar to those of the calcined seed crystals, $548 \text{ m}^2\text{g}^{-1}$ and $0.26 \text{ cm}^3\text{g}^{-1}$.

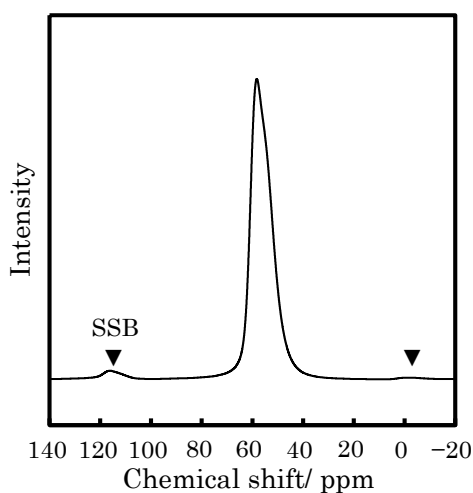


Fig. 3-6 ^{27}Al MAS NMR spectrum of LEV zeolite obtained from FAU zeolite (Sample no. 11). SSB denotes spinning sideband.

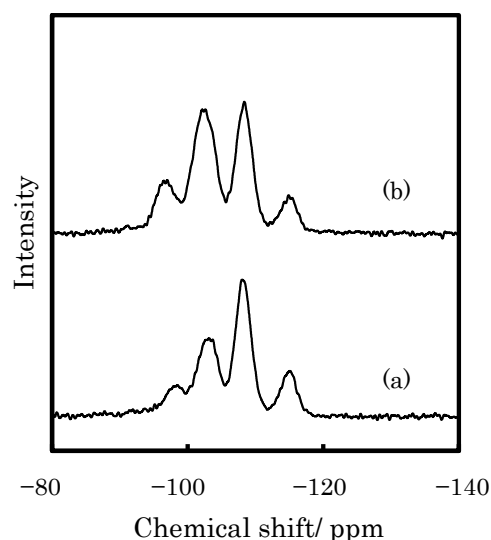


Fig. 3-7 ^{29}Si MAS NMR spectra of (a) non-calcined seed crystals and (b) LEV zeolite obtained from FAU zeolite (Sample no. 11).

The chemical state of aluminum in the obtained LEV zeolite was investigated by ^{27}Al MAS NMR spectroscopy. As shown in Figure 3-6, the ^{27}Al MAS NMR spectrum of the as-synthesized LEV zeolite showed only the peak at approximately 54 ppm, corresponding to the tetrahedrally-coordinated framework aluminum species. No peak corresponding to octahedrally-coordinated aluminum species (which is indicative of extra-framework aluminum species) was observed at around 0 ppm. This implies that all

of the aluminum species present in the LEV zeolite obtained by the interzeolite conversion of FAU zeolite without the use of an additional OSDA, existed within the zeolite framework. The ^{29}Si MAS NMR spectra of the obtained LEV zeolite and the seed crystals presented in Figure 3-7, showed four peaks at approximately -98 , -103 , -108 , and -115 ppm. The LEV structure contains two crystallographically dissimilar tetrahedral sites, 36 T_1 and 18 T_2 . The peak at -115 ppm is assigned to the Si (0Al) configuration of the T_2 sites. The other peaks can be assigned as follows: -98 ppm (SiOM + Si(2Al) $_{T1}$ + Si(3Al) $_{T2}$); -103 ppm (SiOM + Si(1Al) $_{T1}$ + Si(2Al) $_{T2}$); and -108 ppm (Si(0Al) $_{T1}$ + Si(1Al) $_{T2}$) where (M = Na and H) [19]. The difference in the relative intensities of the peaks at -98 and -103 ppm between the LEV zeolite (Si/Al = 5.3) and the seed crystals (Si/Al = 10.7) is due to the difference in the aluminum content.

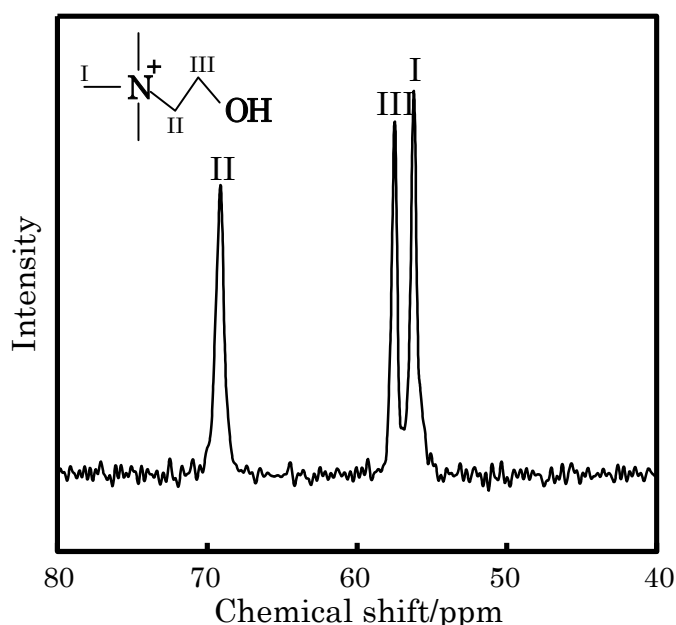


Fig. 3-8 ^{13}C CP/MAS NMR spectrum of as-synthesized LEV zeolite (Sample no. 11).

Figure 3-8 depicts the ^{13}C CP/MAS NMR spectrum of the as-synthesized LEV

zeolite. The spectrum revealed the presence of three peaks, which were centred at 56, 57 and 69 ppm. The peak at 56 ppm is indicative of methyl groups attached to N, namely $-\text{CH}_3$ of $\text{N}-\text{CH}_3$, whereas the peaks at 69 and 57 ppm correspond to the methylene groups of $\text{N}-\text{CH}_2-$ and $-\text{CH}_2-\text{OH}$, respectively. The data indicate that the choline cation was the only organic species existing in the LEV zeolite pores. The amount of choline cation in the zeolitic pores was investigated by thermal analysis.

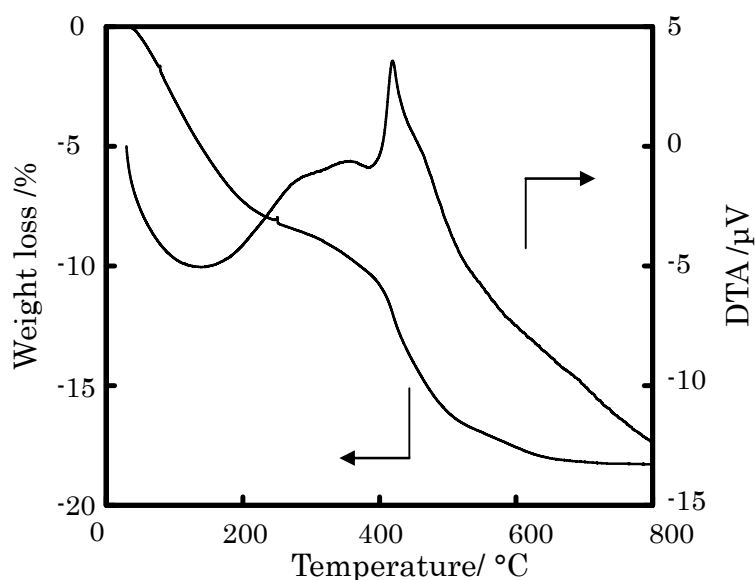


Fig. 3-9 TG/DTA curves of as-synthesized LEV zeolite (Sample no. 11).

The TG/DTA curves of the as-synthesized LEV zeolite (Sample no.11) are presented in Figure 3-9. The thermal profile of the DTA curve was categorized into two zones: (I) 25–200 °C and (II) 200–600 °C. The first zone, which exhibits an endothermic profile, corresponds to the desorption of adsorbed water. The second zone centred at 423 °C, with an exothermic profile, may possibly be attributed to the decomposition and the oxidation of the choline cation, which balances the negative

charge of the framework aluminium species. The weight loss between 200 and 600 °C, which corresponds to the total decomposition of organic moieties, was about 10 wt%. The corresponding weight loss between 200 and 600 °C for the non-calcined seed crystals was ca.19 wt%. Based on these results, a comparison of the amount of choline cation in the as-synthesized LEV zeolite with that in the non-calcined seed crystals which were added to the starting gel shows that there was no difference in the amount of choline cation between the two samples; $0.10 \text{ g (weight of added seed content)} \times 19 \text{ wt\%(TG)} = 0.019 \text{ g}$ for the non-calcined seed crystals and $0.193 \text{ g (total weight of sample collected after crystallization)} \times 10 \text{ wt\%(TG)} = 0.0193 \text{ g}$ for the obtained LEV zeolite. Therefore, it was found that the choline cation did not decompose or dissolve into the solution, i.e., the choline cation remained within the zeolitic pores of the seed crystals during the conversion process.

Given that pure LEV zeolite was reproducibly obtained only when non-calcined seed crystals were used, it was very interesting to understand the role of the choline cation in the zeolitic pores of the seed crystals in the conversion process. It is well known that the crystallization rate of a zeolite can be increased by adding seed crystals and that the enhancement is due to an increase in the surface area and/or promotion of nucleation through some secondary nucleation mechanism, suggesting that the hydrothermal stability of seed crystals is very important. The hydrothermal stability of the seed crystals was, therefore, investigated by a comparison of the XRD pattern of the product obtained from interzeolite conversion of FAU zeolite in the presence of non-calcined seed crystals (after only 30 min of hydrothermal treatment time) with the XRD pattern of the product obtained using calcined seed crystals. The XRD patterns are shown in Figure 3-10. In the case where the non-calcined seed crystals were employed,

diffraction peaks typical of LEV zeolite were clearly observed, whereas the peaks due to FAU zeolite disappeared completely. In contrast, when the calcined seed crystals were employed, no distinctive peaks were observed. These results demonstrate that the choline cation-containing LEV seed crystals are more stable than the calcined crystals and consequently, the crystal surfaces of the non-calcined seed crystals contribute to the crystal growth of LEV zeolite.

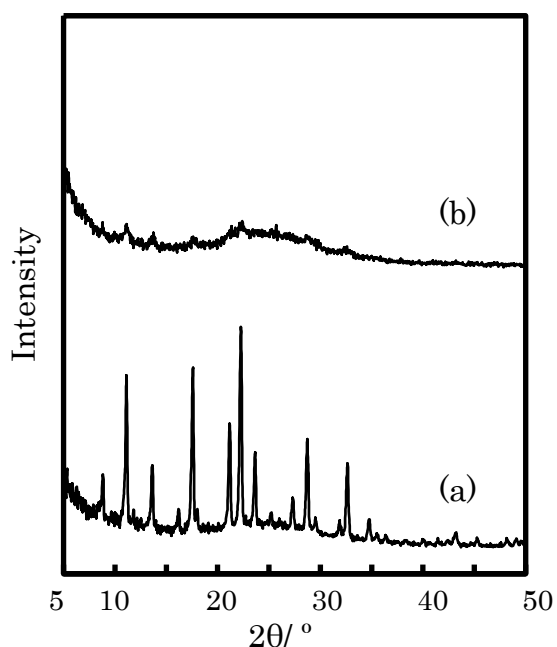


Fig. 3-10 XRD patterns of products obtained from FAU zeolite in the presence of (a) non-calcined and (b) calcined seed crystals at crystallization time of 30 min.

4. Conclusions

Successful conversion of FAU zeolite into LEV zeolite was achieved in the presence of non-calcined seed crystals, without the use of an additional OSDA. The interzeolite conversion depended strongly upon several factors such as the OH^-/SiO_2 ratio of the starting gel, the Si/Al ratio of the starting FAU zeolite and the type of alkaline metal

present. Only the FAU zeolites with Si/Al ratios in the range of 19–26 were converted into LEV zeolite at the OH^-/SiO_2 ratio of 0.6 when NaOH was used as an alkali source. Although the yield of LEV zeolite produced by this method was lower (18–26 %) than that of the conventional method with the use of OSDA, the obtained LEV zeolite exhibited a unique core/shell structure. It was also found that the choline cation occluded in the zeolitic pores contributes to an enhancement in the hydrothermal stability of seed crystals, thereby resulting in the fast and selective crystal growth of LEV zeolite on the seed surfaces. My findings strongly indicate the high possibility for and potential of interzeolite conversion in the presence of seed crystals.

References

- [1] J. Song, L. Dai, Y. Ji, F.-S. Xiao, *Chem. Mater.* 18 (2006) 2775.
- [2] Z. Wu, J. Song, L. Ren, Y. Ji, J. Li, F.-S. Xiao, *Chem. Mater.* 20 (2008) 357.
- [3] B. Xie, J. Song, L. Ren, Y. Ji, J. Li, F.-S. Xiao, *Chem. Mater.* 20 (2008) 4533.
- [4] G. Majano, L. Delmotte, V. Valtchev, S. Mintova, *Chem. Mater.* 21 (2009) 4184.
- [5] Y. Kamiyama, W. Chaikitlisilp, K. Itabashi, A. Shimojima, T. Okubo, *Chem. Asian J.* 5 (2010) 2182.
- [6] T. Yokoi, M. Yoshioka, H. Imai, T. Tatsumi, *Angew. Chem. Int. Ed.* 48 (2009) 9884.
- [7] K. Iyoki, Y. Kamimura, K. Itabashi, A. Shimojima, T. Okubo, *Chem. Lett.* 39 (2010) 730.
- [8] B. Subotić, D. Škrtić, I. Šmit, L. Sekovanić, *J. Cryst. Growth* 50 (1980) 498.
- [9] S. I. Zones, *J. Chem. Soc. Faraday Trans.* 87 (1991) 3709.
- [11] Y. Kubota, H. Maekawa, S. Miyata, T. Tatsumi, Y. Sugi, *Micropor. Mesopor. Mater.* 101 (2007) 115.
- [12] H. Jon, K. Nakahata, B. Lu, Y. Oumi, T. Sano, *Micropor. Mesopor. Mater.* 96 (2006) 72.
- [13] H. Jon, S. Takahashi, H. Sasaki, Y. Oumi, T. Sano, *Micropor. Mesopor. Mater.* 113 (2008) 56.
- [14] M. Itakura, T. Inoue, A. Takahashi, T. Fujitani, Y. Oumi, T. Sano, *Chem. Lett.* 39 (2008) 908.
- [15] H. Sasaki, H. Jon, M. Itakura, T. Inoue, T. Ikeda, Y. Oumi, T. Sano, *J. Porous Mater.* 16 (2009) 465.
- [16] T. Inoue, M. Itakura, H. Jon, A. Takahashi, T. Fujitani, Y. Oumi, T. Sano, *Micropor. Mesopor. Mater.* 122 (2009) 149.

[17] M. Itakura, Y. Oumi, M. Sadakane, T. Sano, *Mater. Res. Bull.* 45 (2010) 646.

[18] K. Honda, A. Yashiki, M. Itakura, Y. Ide, M. Sadakane, T. Sano, *Micropor. Mesopor. Mater.* in press.

[19] P. Lentz, J.B. Nagy, L. Delevoye, Y. Dumazy, C. Fernandez, J.-P. Amoureux, C.V. Tuoto, A. Nastro, *Colloid Surf. A* 158 (1999) 13.

Chapter 4

Hydrothermal conversion of FAU and *BEA zeolites into MAZ zeolites in the presence of non-calcined seed crystals

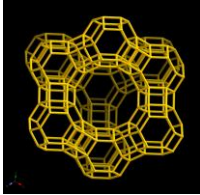

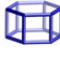
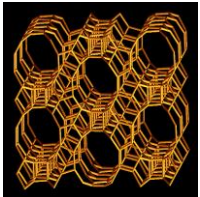



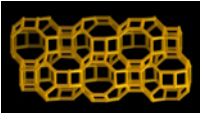
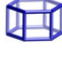
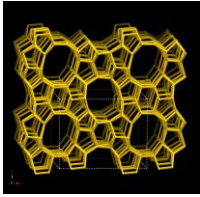




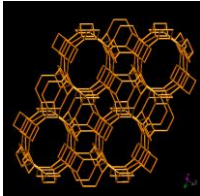


1. Introduction

Zeolites are a class of microporous crystalline aluminosilicates. Because of their desirable properties, such as having a unique framework structure, solid acidity, high surface area, and molecular sieving and ion-exchange abilities, they have been widely used in adsorption, catalysis, and ion-exchange applications. In general, high-silica zeolites with medium to large pore size are synthesized by hydrothermal treatment of amorphous aluminosilicate hydrogel used as starting material in the presence of various organic structure-directing agents (OSDAs). The OSDAs end up occluding the cages and pores of the final zeolite and, therefore, must be removed, generally by calcination at high temperatures, which generates harmful gaseous pollutants. Furthermore, the use of expensive OSDAs also increases the cost of zeolite. As a result, the recent development toward OSDA-free zeolite synthesis using seed crystals has attracted considerable attention [1], and several research groups have succeeded in the OSDA-free synthesis of zeolites of structure type ZSM-5(MFI)[2,3], ECR-1(EON)[4], ZSM-34(ERI/OFF)[5], *BEA[6–8], RTH[9], ZSM-12(MTW)[10], EMT[11], SUZ-4(SZR)[12], omega(MAZ)[13], and MTT[14]. Okubo and coworkers have

proposed a working assumption named “Composite Building Unit (CBU) Hypothesis” [15]. According to their hypothesis, it is possible to synthesize the desired zeolite via addition of seeds of the target zeolite to the hydrogel prepared without using an OSDA if at least one common CBU exists in the two frameworks.

Sano et al. have investigated the potential of this synthesis route for interzeolite conversion, *i.e.*, the hydrothermal conversion of one zeolite into another one [16,17]. I also succeeded in the OSDA-free synthesis of *BEA and LEV zeolites from FAU zeolites in the presence of seed crystals [18,19]. Table 4-1 lists the framework structures and CBUs of several zeolites, as summarized in the database of the Structure Commission of the International Zeolite Association [20]. The starting FAU zeolite contains the CBUs *sod* and *d6r*, and the final LEV zeolite contains *d6r* (in common with the initial FAU zeolite). *BEA zeolite contains the CBUs *mor*, *bea*, and *mtw*. Although there is no common CBU between FAU and *BEA, a common four-membered ring (4-MR) is observed in the CBUs *d6r* and *bea*, which may act as the common structural unit. These results strongly suggest that the structural similarity between the starting zeolite (FAU) and the finally crystallized zeolite (*BEA and LEV) is a crucial factor for the zeolite crystal growth. Namely, it is suggested that desired zeolites can be synthesized in the presence of seed crystals without the use of OSDAs if the starting FAU zeolite is decomposed/dissolved into locally ordered aluminosilicate species (nanoparts) with chemical structures that are suitable for crystallization into the desired zeolite. For the seed-assisted and OSDA-free synthesis of zeolites, it is also recognized that the hydrothermal stability of the seed crystals during hydrothermal conversion is very important for the reproducibility of the interzeolite conversion [19].

Table 4-1 Framework structures and CBUs of various zeolites.

Zeolite	Framework structure	CBU
FAU		 <i>sod</i>  <i>d6r</i>
*BEA		 <i>mor</i>  <i>bea</i>  <i>mtw</i>
LEV		 <i>d6r</i>
MFI		 <i>mor</i>  <i>mel</i>  <i>mtl</i>  <i>cas</i>
MAZ		 <i>dsc</i>  <i>gme</i>

To further understand the interzeolite conversion process, in this study, I investigated the seed-assisted synthesis of MAZ zeolite from various starting zeolites with different CBUs, such as FAU, *BEA, and MFI zeolites, without any additional OSDA. Considering the hydrothermal stability, non-calcined seeds were used. FAU zeolite contains CBU composed of mainly 4-MR, whereas *BEA zeolite includes 4- and

5-MRs, and MFI zeolite is comprised of 5- and 6-MRs. MAZ zeolite contains the CBU_s *dsc* (with a 4-MR) and *gmr*; and has a tubular 12-MR channel system (0.74 nm). Because of the textural similarity with MOR zeolite, MAZ zeolite can be applied to adsorbents and catalysts [21-23].

2. Experimental

2.1 Preparation of starting zeolites and MAZ seed crystals

The starting FAU and *BEA zeolites with various Si/Al ratios were prepared from NH₄-Y zeolite (Si/Al = 2.8, Tosoh Co., Japan) and H-*BEA zeolite (Si/Al = 21, Tosoh Co., Japan) by carrying out dealumination involving a combination of steaming at 700 °C and H₂SO₄ (0.74–0.85 M) treatment at 75 °C for 4 h, respectively. MFI zeolites were synthesized using trapropylammonium bromide (TPABr) as OSDA, Al (NO₃)₃·9H₂O, colloidal silica, NaOH, and deionized water. The hydrogel composition was as follows: SiO₂/Al₂O₃ = 50–100, OH⁻/SiO₂ = 0.1, H₂O/SiO₂ = 40, and TPABr/SiO₂ = 0.1. The resultant hydrogel was transferred into a 300 mL stainless-steel autoclave and stirred at 160 °C under autogenous pressure for 16 h. The precipitated crystals then were washed with deionized water, dried overnight at 120 °C, and calcined in air at 500 °C for 10 h to remove the organic cations remaining in the zeolite framework. The zeolite was protonated in a hydrochloric-acid solution (0.6 mol dm⁻³) at 60 °C for 24 h and calcined in air at 500 °C for 6 h.

The seed crystals of MAZ zeolite were synthesized using fumed silica (Cab-o-sil M5, CABOT Co.), NaAlO₂, tetramethylammonium hydroxide (TMAOH) as OSDA, NaOH, and deionized water, according to the method described in literature [24]. The resultant hydrogel with a chemical composition of SiO₂/Al₂O₃ = 20, TMAOH/SiO₂ = 0.2,

$\text{NaOH}/\text{SiO}_2 = 0.64$, and $\text{H}_2\text{O}/\text{SiO}_2 = 10$ was transformed into a 30 mL Teflon-lined stainless-steel vessel and heated at $100\text{ }^\circ\text{C}$ for 10 days in a convection oven under static conditions. After crystallization, the solid product was collected by centrifugation and washed thoroughly with deionized water, and then dried overnight at $120\text{ }^\circ\text{C}$.

2.2 OSDA-free synthesis of MAZ zeolite in the presence of non-calcined seed crystals

Hydrothermal conversion of the starting zeolite into MAZ zeolite was carried out by adding the starting zeolite to an aqueous solution of MOH (M: alkaline metal). Based on the previous result that the hydrothermal stability of the employed seed crystals is a crucial factor in the interzeolite conversion without OSDA, non-calcined seed crystals were used [19]. Because OSDA cations occluding the zeolitic pores of the seed crystals contribute to an enhancement in the hydrothermal stability, the result is a fast and selective crystal growth of the target zeolite on the seed surfaces. The prepared hydrogel was placed into a 30 mL Teflon-lined stainless-steel autoclave. Hydrothermal conversion was conducted at $70\text{--}170\text{ }^\circ\text{C}$ for 7–28 days in a convection oven under autogenous pressure and static conditions. After crystallization, the solid product was collected by centrifugation and washed thoroughly with deionized water until a nearly neutral pH was achieved, and then dried overnight at $70\text{ }^\circ\text{C}$. The yield of product was defined as follows:

$$\text{Yield (\%)} = \frac{\text{Product (g)} - \text{Seeds (g)}}{\text{Starting Si \& Al sources (g)}} \times 100$$

2.3 Characterization

Powder X-ray diffraction (XRD) patterns of the solid products were collected on a Rigaku Mini Flex diffractometer with curved-graphite monochromator using Cu K α radiation and operated at 30 kV and 15 mA. Bulk Si/Al ratios were determined using inductively coupled plasma optical emission spectroscopy (ICP, Seiko SPS7000). The crystal morphology was measured using scanning electron microscopy (SEM, Hitachi S-4800). ^1H - ^{13}C cross polarized magic angle spinning nuclear magnetic resonance (CP/MAS NMR) and ^{27}Al MAS NMR spectra were recorded using a 7 mm diameter zirconia rotor with Bruker Avance DRX-400 NMR at 100.6 MHz and 104.3 MHz, respectively. The rotor was spun at 4 kHz for ^{13}C CP/MAS NMR, and at 6 kHz for ^{27}Al MAS NMR. The spectra were accumulated with 6.0 μs pulses, 25 s recycle delay, and 1000 scans for ^{13}C CP/MAS NMR, and pulses of 2.3 μs , delay time of 1 s, and 1000 scans for ^{27}Al MAS NMR. $\text{Al}(\text{NO}_3)_3 \cdot 9\text{H}_2\text{O}$ and $\text{Si}(\text{CH}_3)_4$ were used as chemical-shift references for ^{27}Al MAS and ^{13}C CP/MAS NMR, respectively. Prior to the ^{27}Al MAS NMR measurements, the samples were moisture-equilibrated over a saturated solution of NH_4Cl for 24 h. Thermal analysis was performed using a thermogravimetry/differential thermal analysis (TG/DTA) apparatus (SSC/5200, Seiko Instruments). The sample (ca. 7 mg) was heated in a flow of air (50 mL min^{-1}) at $5 \text{ }^\circ\text{C min}^{-1}$ from room temperature to $800 \text{ }^\circ\text{C}$. Nitrogen adsorption isotherms at $-196 \text{ }^\circ\text{C}$ were obtained using a conventional volumetric apparatus (BELSORP-mini, Bel Japan, Inc.). Prior to the adsorption measurements, the calcined samples (ca. 0.1 g) were evacuated at $400 \text{ }^\circ\text{C}$ for 10 h.

3. Results and discussion

3.1 Preparation and characterization of starting zeolites and seed crystals

Figure 4-1 shows XRD patterns and SEM images of typical starting zeolites (FAU, *BEA, MFI) and MAZ seeds. The XRD patterns exhibited only the typical features of the corresponding zeolites, thus indicating high crystallinity without impurity. The SEM images also showed that no amorphous or impurities phase existed in all the samples. The MAZ seed crystals exhibited a round shape with an average diameter of approximately 2 μm , composed of aggregates in shape of small rods. From the ^{13}C CP/MAS NMR and TG/DTA measurements of the as-synthesized MAZ seeds, it was found that the TMA^+ cation was the only organic species existing in the MAZ zeolite pores at an amount of ca. 17 wt% (not shown).

3.2 OSDA-free synthesis of MAZ zeolite from FAU zeolite

As described above, I already succeeded in seed-assisted FAU-*BEA and FAU-LEV interzeolite conversions without the use of an OSDA. The seed-assisted and OSDA-free zeolite synthesis was carried out using the non-calcined seeds at MOH/SiO_2 ratio of 0.6 and $\text{H}_2\text{O}/\text{SiO}_2$ ratio of 15–20. I applied the hydrothermal synthesis conditions to accomplish the FAU-MAZ interzeolite conversion. The detailed hydrothermal synthesis conditions and characteristics of the obtained products are listed in Table 4-2.

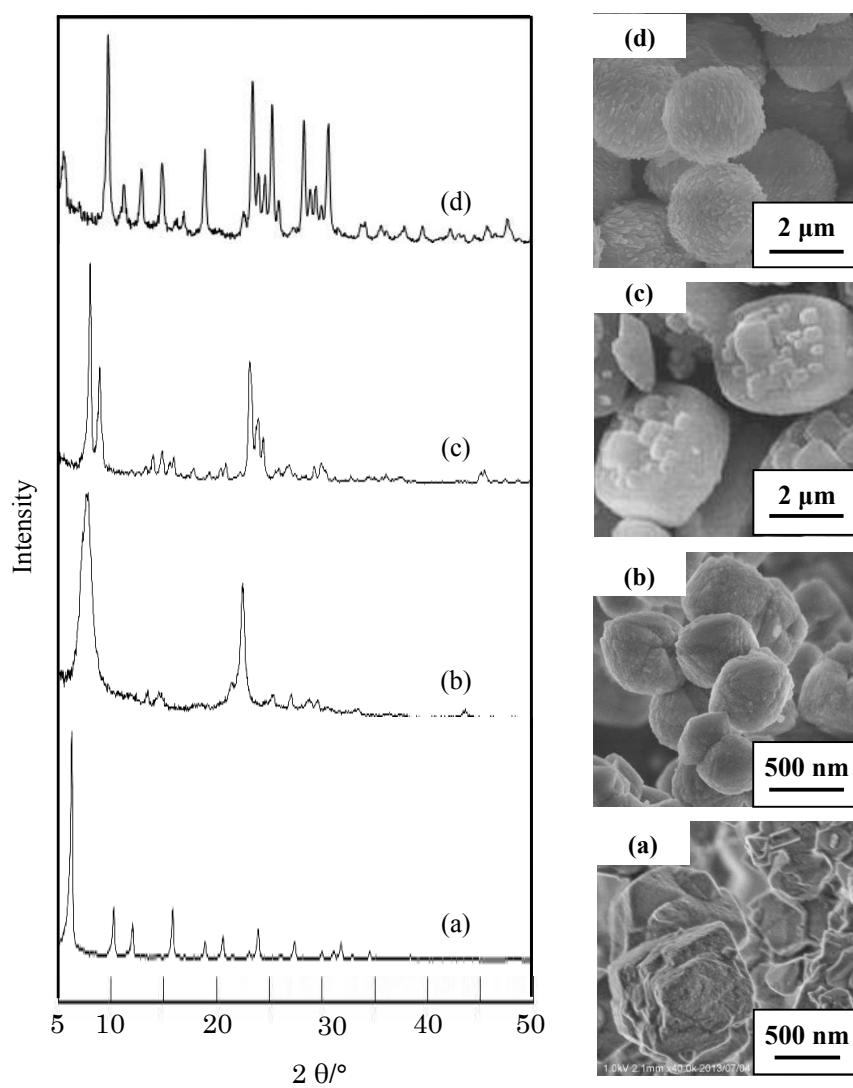


Fig. 4-1 XRD patterns and SEM images of typical starting zeolites of type (a) FAU(Si/Al = 16.9), (b)*BEA (Si/Al = 43.5), (c) MFI(Si/Al = 40.0), and (d) MAZ seed (Si/Al = 3.9).

At first, I investigated the influence of the synthesis temperature on the interzeolite conversion. The FAU zeolite with a Si/Al ratio of 16.9 was used as starting zeolite. Amorphous material co-existed together with MAZ zeolite when the interzeolite conversion was conducted at 50 °C (Run no. 1). When the synthesis temperature was increased to 70 °C, however, the FAU–MAZ zeolite conversion effectively took place and a pure MAZ zeolite was obtained (Run no. 2). When the synthesis temperature was further enhanced from 70 °C to 100 °C, MOR zeolite was generated as a by-product (Run no. 3). Therefore, the optimal synthesis temperature was determined to be 70 °C. The synthesis temperature was slightly lower in comparison to the procedure described by Barrer et al., in which the MAZ zeolite could be crystallized at 80 °C

Table 4-2 Seed-assisted and OSDA-free synthesis of MAZ from FAU.^a

Run no.	Synthesis conditions				Product		
	Si/Al ratio of starting FAU	NaOH/SiO ₂	Temp. (°C)	Seed (wt %)	Phase	Yield (%)	Bulk Si/Al
1	16.9	0.6	50	33.3	MAZ, Am.		
2	16.9	0.6	70	33.3	MAZ	34	4.8
3	16.9	0.6	100	33.3	MAZ, MOR		
4	9.2	0.6	70	33.3	FAU, MAZ		
5	27.6	0.6	70	33.3	MAZ	14	5.8
6	44.0	0.6	70	33.3	MAZ	8	5.9
7	72.0	0.6	70	33.3	MAZ	trace	
8	16.9	0.6	70	9.1	FAU, MAZ		
9	16.9	0.6	70	16.7	FAU, MAZ		
10	16.9	0.6(LiOH)	70	33.3	MAZ	36	6.4
11	16.9	0.6(KOH)	70	33.3	MAZ, Am.		
12	16.9	0.6(RbOH)	70	33.3	MAZ, OFF.		
13	16.9	0.6(CsOH)	70	33.3	MAZ, Am.		

^a Si/Al ratio = 20, synthesis time = 14 days, Si/Al ratio of MAZ seed = 3.9

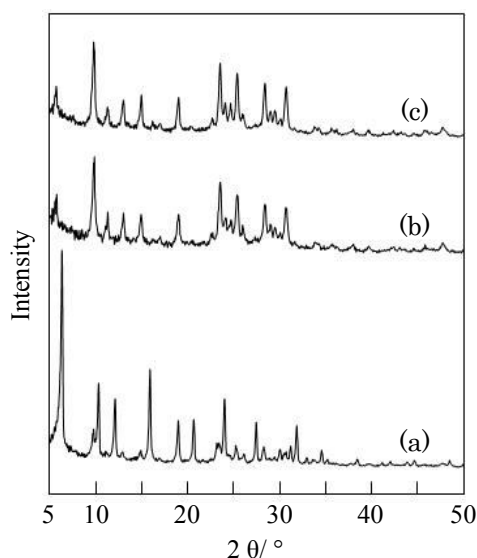


Fig. 4-2 XRD patterns of products obtained from FAU(Si/Al=16.9) after various hydrothermal treatment times at 70 °C. (a) before hydrothermal treatment, (b) after 3 d, and (c) after 14 d.

from amorphous hydrogel in the presence of TMA^+ cations used as OSDA [25]. Figure 4-2 shows the XRD patterns of products obtained from FAU(Si/Al=16.9) after hydrothermal treatment for 3 and 14 days at 70 °C. The intensities of the peaks corresponding to the MAZ zeolite increased with the hydrothermal treatment time and the pure MAZ zeolite was obtained after hydrothermal treatment for 14 days.

Sano et al. already reported that the interzeolite conversion was strongly dependent on the Si/Al ratio of the starting zeolite [16–19]. In order to investigate the influence of the Si/Al ratio of the starting material on the OSDA-free FAU–MAZ interzeolite conversion, FAU zeolites with various Si/Al ratios were prepared by dealumination and hydrothermal treatment. For the FAU zeolite with a Si/Al ratio of 9.2, the interzeolite conversion did not completely proceed, evidenced by the presence of the starting FAU zeolite in the product (Run no. 4). However, in case of using the FAU zeolites with

Si/Al ratios of 27.6 and 44.0, pure MAZ zeolites were obtained (Run nos. 5 and 6, respectively). The yield decreased on increasing Si/Al ratio. If the FAU zeolite with a ratio of Si/Al = 72.0 was used, only a trace amount of MAZ zeolite was obtained (Run no. 7). The bulk Si/Al ratios of the resulting MAZ zeolites were considerably lower than those of the starting FAU zeolites, probably because of higher alkaline conversion conditions, giving rise to an increase of the silicon concentration in the liquid phase.

Next, I investigated the influence of the content of seed crystals added to the starting hydrogel. When the content of seed crystals was decreased from 33.3 wt% to 16.7 wt% or even to 9.1 wt%, the formation of MAZ zeolite was observed (Run nos. 8 and 9). However, the starting FAU zeolite still remained even after hydrothermal treatment for 14 days, indicating that its decomposition/dissolution rate depended on the content of seed crystals added.

Finally, the FAU–MAZ interzeolite conversion was carried out by using various types of alkaline metal cations. As listed in Table 4-2 (Run nos. 10–13), if LiOH was employed instead of NaOH, pure MAZ zeolite was obtained (Run no. 10). However, KOH, RbOH, and CsOH did not yield pure MAZ-zeolite phase (Run nos. 11–13). Although I do not have enough data to explain the difference in the interzeolite conversion behavior, one could argue as follows. Smaller cations like Li^+ and Na^+ act as structure-forming entities, whereas larger cations like K^+ , Rb^+ , and Cs^+ act in a structure-breaking way [26], resulting in the observed differences in the decomposition/dissolution rate of the starting FAU and the crystal-growth rate of MAZ. Figure 4-3 shows SEM images of the MAZ zeolites obtained by using NaOH and LiOH. The crystal morphology of the MAZ zeolites was different from that of the MAZ seed crystals (Fig. 1(d)), and the crystal size was ca. 200–500 nm.

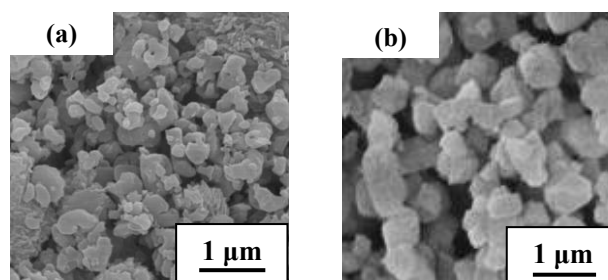


Fig. 4-3 SEM images of MAZ obtained using (a) NaOH (Run no. 2) and (b) LiOH (Run no. 10) as alkali source.

The chemical state of aluminum in the MAZ zeolites was investigated by ^{27}Al MAS NMR. As shown in Figure 4-4(a), the ^{27}Al MAS NMR spectrum of MAZ zeolite synthesized using NaOH showed two resonances centered at 52 and 59 ppm. No peak corresponding to octahedrally-coordinated aluminum ions (which is indicative of extra-framework aluminum species) was observed at around 0 ppm. Since it is well known that MAZ zeolite crystallographically has two kinds of T-sites in the framework [27], therefore, these results imply that all aluminum species of the MAZ zeolite existed within the zeolite framework. On the other hand, in the case of MAZ zeolite synthesized using LiOH, the resonance corresponding to octahedrally coordinated aluminum, namely extraframework aluminum species, was observed at around 0 ppm.

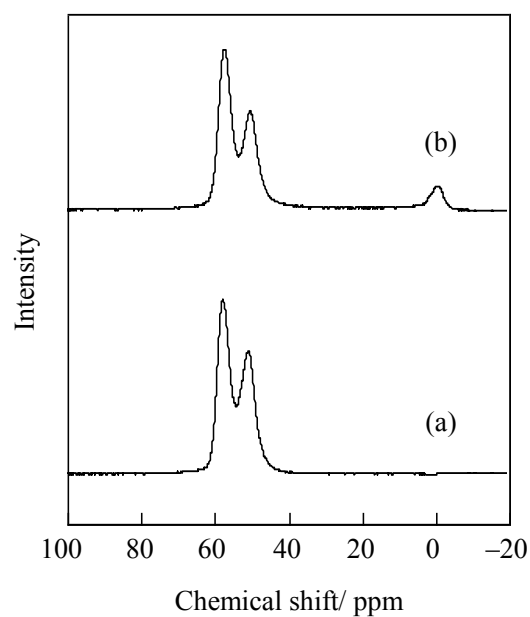


Fig. 4-4 ^{27}Al MAS NMR spectra of MAZ obtained using (a) NaOH(Run no. 2) and (b) LiOH(Run no. 10).

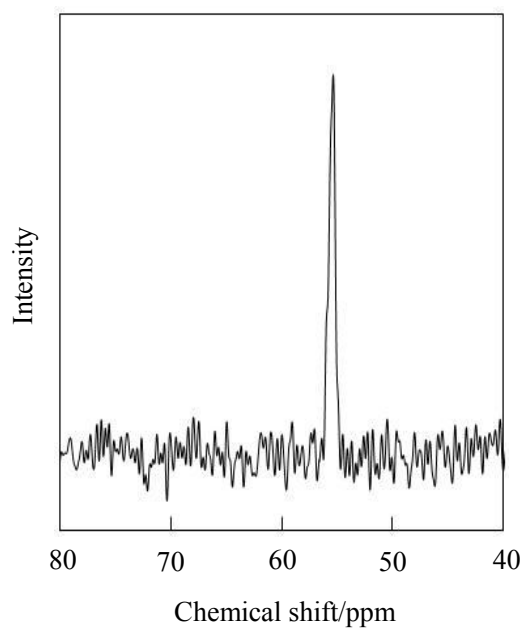


Fig. 4-5 ^{13}C CP/MAS NMR spectrum of as-synthesized MAZ obtained using NaOH(Run no. 2).

Figure 4-5 depicts the ^{13}C CP/MAS NMR spectrum of the as-synthesized MAZ zeolite using NaOH. Only one peak was observed at ca. 56 ppm, which is indicative of methyl groups attached to N, namely $-\text{CH}_3$ of $\text{N}-\text{CH}_3$. Therefore, it was found that TMA^+ species remained intact in the MAZ-zeolite pores. The amount of TMA^+ cations in the zeolitic pores was investigated by thermal analysis. The TG curve of the MAZ sample is presented in Figure 4-6. The weight loss between 250 and 600 °C, which corresponds to the decomposition/oxidation of TMA^+ cations, was ca. 10 wt%. Based on these results, a comparison of the amount of TMA^+ cations in the as-synthesized MAZ zeolite with that in the non-calcined seed crystals which were added to the starting gel showed that there was no difference: 0.25 g (weight of added seed content) \times 17 wt%(TG) = 0.0425 g for the non-calcined seed crystals and

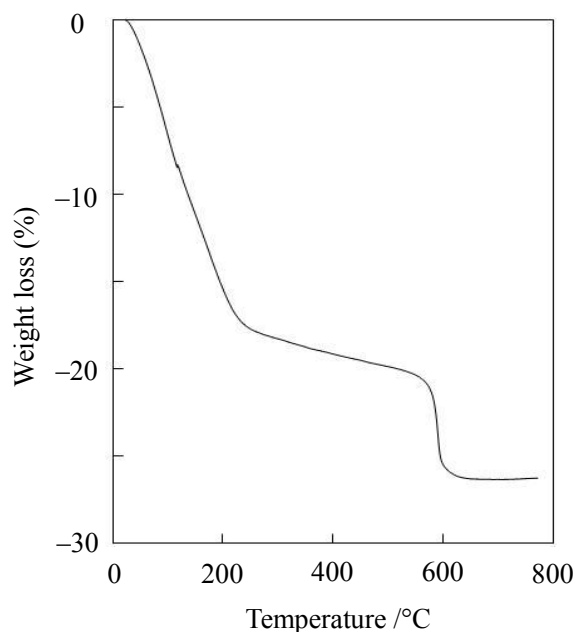


Fig. 4-6 TG curve of MAZ obtained using NaOH(Run no. 2).

0.42 g (total weight of the sample collected after crystallization) \times 10 wt%(TG) = 0.042 g for the obtained MAZ zeolite. Therefore, it was shown that the TMA^+ cations did not decompose or dissolve into the solution, i.e., the TMA^+ cations remained within the zeolitic pores of the seed crystals during the conversion process.

Figure 4-7 depicts the nitrogen adsorption isotherms of the MAZ zeolites obtained using NaOH and LiOH. Both samples were calcined at 600 °C for 10 h. The observed rapid increase in the amount of adsorbed N_2 at relatively low pressure indicates microporous structure. The BET surface areas and micropore volumes were calculated to be $287 \text{ m}^2\text{g}^{-1}$ and $0.14 \text{ cm}^3\text{g}^{-1}$ for MAZ obtained using NaOH, and $319 \text{ m}^2\text{g}^{-1}$ and $0.14 \text{ cm}^3\text{g}^{-1}$ for MAZ obtained using LiOH, respectively.

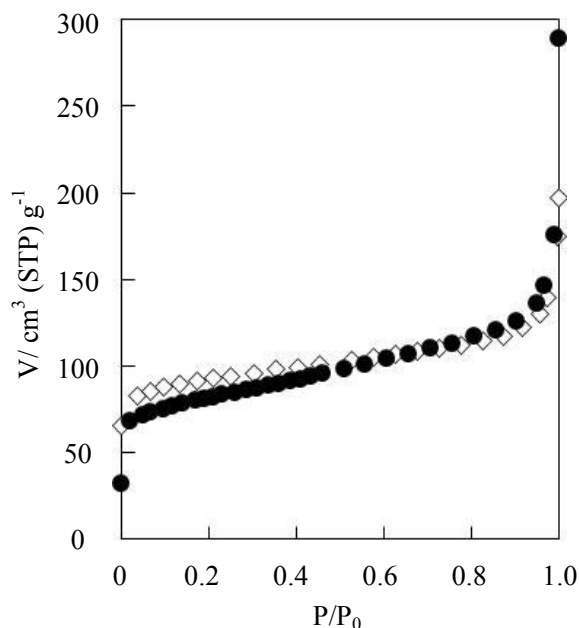


Fig. 4-7 Nitrogen adsorption isotherms of MAZ obtained using (●) NaOH(Run no. 2) and (◇) LiOH(Run no. 10).

3.3 OSDA-free synthesis of MAZ zeolite from *BEA and MFI zeolites

For interzeolite conversion, the structural similarity between the starting and the target zeolites is a crucial factor [28]. Therefore, I investigated the seed-assisted and OSDA-free synthesis of MAZ zeolite from *BEA and MFI instead of FAU zeolite, which contain CBUs composed of 4- and 5-MRs and 5- and 6-MRs, respectively. MAZ zeolite contains the CBUs *dsc* and *gmr*, which are composed of a 4-MR, as shown in Table 4-1. The hydrothermal conversion conditions are listed in Table 4-3. In the case of using *BEA zeolite as starting material with a ratio of Si/Al = 21, pure MAZ zeolite was obtained. However, the yield was slightly lower if compared to the conversion with FAU zeolite (Run no. 14). This difference in yield of MAZ zeolite is probably attributed to the difference in the amount of available 4-MR CBU. When *BEA zeolite with a ratio of Si/Al = 43.5 was used, MOR zeolite was obtained as a by-product (Run no. 15). It was also found that MAZ zeolite could not be obtained from MFI zeolites with Si/Al ratios of 25 and 40 (Run nos. 16 and 17, respectively).

Table 4-3 Seed-assisted and OSDA-free synthesis of MAZ from various starting materials.^a

Run no.	Si&Al source (Si/Al)	Products		
		Phase	Yield (%)	Bulk Si/Al
14	*BEA(21.0)	MAZ	22	6.1
15	*BEA(43.5)	MAZ, MOR		
16	MFI(25.0)	MFI, MAZ		
17	MFI(40.0)	MFI,MAZ		
18	Cab-o-sil M5/NaAlO ₂ (16.9)	MAZ	30	5.8

^a Si/Al ratio = 20, NaOH/SiO₂=0.6, synthesis time = 14 days, temperature = 70 °C, content of MAZ seed (Si/Al = 3.9) = 33.3 wt%.

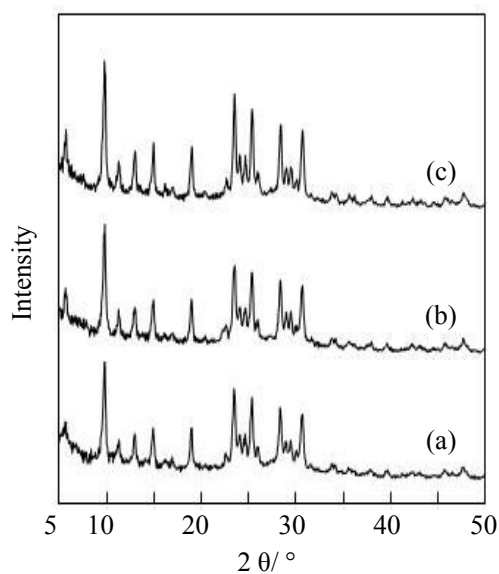


Fig. 4-8 XRD patterns of MAZ obtained using (a) amorphous hydrogel (Cab-O-Sil M5/NaAlO₂)(Run no. 18), (b) *BEA(Run no. 14), and (c) FAU(Run no. 2).

Figure 4-8 shows the XRD pattern of MAZ zeolite obtained from *BEA zeolite. For reference purpose, the XRD patterns of MAZ zeolites obtained from FAU zeolite and amorphous hydrogel (Cab-o-sil-M5/NaAlO₂) are also shown. The peak intensity of MAZ zeolite converted from FAU zeolite was slightly larger than in the other two cases, indicating a higher crystallinity. Figure 4-9 shows the SEM images of MAZ zeolites obtained from *BEA zeolite and amorphous hydrogel. The morphology of both samples was considerably different from that of the MAZ seed crystals. Figure 4-10 depicts the nitrogen adsorption isotherms of the calcined MAZ zeolites from *BEA zeolite and amorphous hydrogel. The nitrogen adsorption isotherm of MAZ zeolite obtained by *BEA–MAZ interzeolite conversion showed type I behavior. The BET surface area and micropore volume were calculated to be 141 m²g⁻¹ and 0.11 cm³g⁻¹, respectively. These values are considerably smaller those of MAZ zeolite (287 m²g⁻¹, 0.14 cm³g⁻¹) resulting from FAU, indicating a lower crystallinity of MAZ zeolite from *BEA. In the case of

MAZ zeolite from amorphous hydrogel, however, nitrogen adsorption hardly occurred. These results strongly indicate that the crystallinity of MAZ zeolite strongly depends on the starting material.

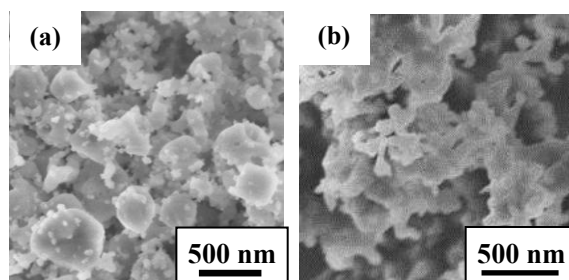


Fig. 4-9 SEM images of MAZ obtained using (a) *BEA (Run no. 14) and (b) amorphous hydrogel (Run no. 18).

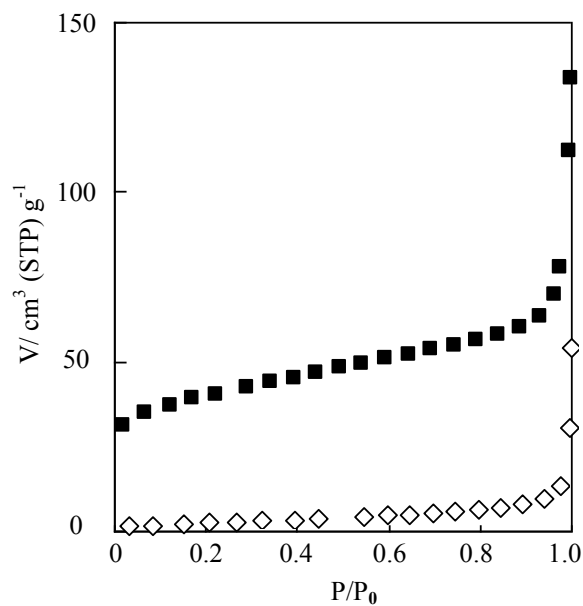


Fig. 4-10 Nitrogen adsorption isotherms of MAZ obtained using (■) *BEA (Run no. 14) and (◇) amorphous hydrogel (Run no. 18).

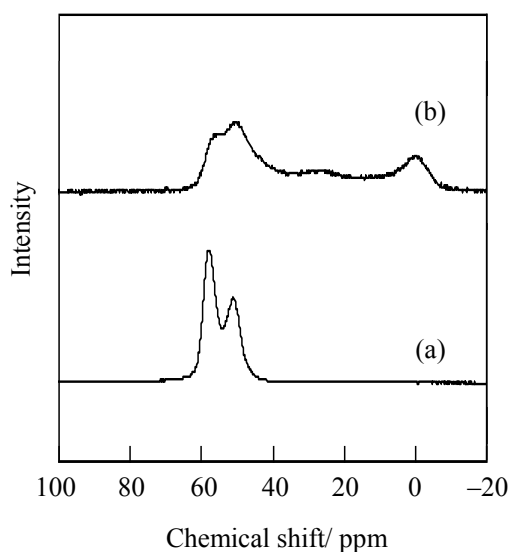


Fig. 4-11 ^{27}Al MAS NMR spectra of MAZ obtained using (a) *BEA(Run no. 14) and (b) amorphous hydrogel(Run no. 18).

Figure 4-11 shows the ^{27}Al MAS NMR spectra of MAZ zeolites from *BEA zeolite and amorphous hydrogel. The two clear resonances centered at 52 and 59 ppm are assigned to the tetrahedrally coordinated framework aluminum, similar to those of MAZ from FAU. In the spectrum of MAZ converted from amorphous hydrogel, however, the two resonance peaks were broad, and the resonance assigned to non-framework aluminum was additionally observed at 0 ppm. Taking into account the facts that MAZ zeolite contains CBUs composed of 4-MR and that it is not easy to synthesize such zeolites from high-silica aluminosilicate hydrogel (because of the high strain of the 4-MR), it may be concluded that starting zeolites containing 4-MR-based CBUs, such as FAU and *BEA zeolite, are much more effective for the seed-assisted and OSDA-free synthesis of MAZ zeolite.

4. Conclusions

I investigated the seed-assisted synthesis of MAZ zeolites from various starting zeolites with different framework structures, such as FAU, *BEA, and MFI, without the use of OSDA. The FAU–MAZ interzeolite conversion was successfully achieved in the presence of non-calcined seed crystals without the use of additional OSDA. Although MAZ zeolite could be synthesized from *BEA zeolite and amorphous hydrogel (Cab-o-sil M5/NaAlO₂), the crystallinity of the resulting crystals was lower, as evaluated by XRD, ²⁷Al MMS NMR, and N₂ adsorption. Therefore, it was confirmed that the structural similarity between the starting and the target zeolites is the crucial factor for interzeolite conversion. CBUs composed of a common 4-MR entity are a key for the OSDA-free synthesis of MAZ zeolite. The findings of this study indicate strongly that interzeolite conversion represents an alternative OSDA-free synthesis method of many zeolite types.

References

- [1] X. Meng, F.-S. Xiao, *Chem. Rev.* 114 (2014) 1521.
- [2] V. P. Shiralkar, A. Clearfield, *Zeolites* 9 (1989) 363.
- [3] N. Ren, Z.-J. Yang, X.-C. Lv, J. Shi, Y.-H Zhang, Y. Tang, *Micropor. Mesopor. Mater.* 131 (2010) 103.
- [4] J. Song, L. Dai, Y. Ji, F.-S. Xiao, *Chem. Mater.* 18 (2006) 2778.
- [5] Z. Wu, J. Song, Y. Ji, L. Ren, F.-S. Xiao, *Chem. Mater.* 20 (2008) 357.
- [6] B. Xie, J. Song, L. Ren, Y. Ji, J. Li, F.-S. Xiao, *Chem Mater.* 20 (2008) 4533.
- [7] G. Majano, L. Delmotte, V. Valtchev, S. Mintova, *Chem. Mater.* 21 (2009) 4184.
- [8] Y. Kamimura, W. Chaikitlisilp, K. Itabashi, A. Shimojima, T. Okubo, *Chem. Asian J.* 5 (2010) 2182.
- [9] T. Yokoi, M. Yoshioka, H. Imai, T. Tatsumi, *Angew. Chem. Int. Ed.* 48 (2009) 9884.
- [10] K. Iyoki, Y. Kamimura, K. Itabashi, A. Shimojima, T. Okubo, *Chem. Lett.* 39 (2010) 730.
- [11] E.-P. Ng, D. Chateigner, T. Bein, V. Valtchev, S. Mintova, *Science* 335 (2012) 70.
- [12] W. Zhang, Y. Wu, J. Gu, H. Zhou, J. Wang, *Mater. Res. Bull.* 46 (2011) 1451.
- [13] A. Ogawa, K. Iyoki, Y. Kamimura, S.P. Elangovan, K. Itabashi, T. Okubo, *Micropor. Mesopor. Mater.* 186 (2014) 21.
- [14] Q. Wu, X. Wang, X. Meng, C. Yang, Y. Liu, Y. Jin, Q. Yang, F.-S. Xiao, *Micropor. Mesopor. Mater.* 186 (2014) 106.
- [15] K. Itabashi, Y. Kamimura, K. Iyoki, A. Shimojima, T. Okubo, *J. Am. Chem. Soc.* 134 (2012) 11542.
- [16] T. Sano, M. Itakura, M. Sadakane, *J. Jpn. Petrol. Inst.* 56 (2013) 183.
- [17] H. Jon, N. Ikawa, Y. Oumi, T. Sano, *Chem. Mater.* 20 (2008) 4135.

- [18] K. Honda, A. Yashiki, M. Itakura, Y. Ide, M. Sadakane, T. Sano, *Micropor. Mesopor. Mater.* 142 (2011) 161.
- [19] A. Yashiki, K. Honda, A. Fujimoto, S. Shibata, Y. Ide, M. Sadakane, T. Sano, J. *Cryst. Growth* 325 (2011) 96.
- [20] International Zeolite Association Web site: <http://www.iza-online.org/>
- [21] R.A. Shigeishi, B.H. Chiche, F. Fajula, *Micropor. Mesopor. Mater.* 43 (2001) 211.
- [22] A.J. Perrotta, C. Kibby, B.R. Mitchell, E.R. Tucci, *J. Catal.* 55 (1978) 240.
- [23] V. Solinas, R. Monaci, B. Marongiu, L. Forni, *Appl. Catal.* 5 (1983) 171.
- [24] A.M. Goossens, E.J.P. Feijen, G. Verhoeven, B.H. Wouters, P.J. Grobel, P.A. Jacobs, J.A. Martens, *Micropor. Mesopor. Mater.* 35-36 (2000) 555.
- [25] R. Aiello, R.M. Barrer, *J. Chem. Soc. (A)* (1970) 1470.
- [26] Z. Gabelica, N. Blom, E.G. Derouane, *Appl. Catal.* 5 (1983) 227.
- [27] B.H. Wouters, T. Chen, A.M. Goossens, J.A. Martens, P.J. Grobet, *J. Phys. Chem. B* 103 (1999) 8093.
- [28] K. Honda, M. Itakura, Y. Matsuura, A. Onda, Y. Ide, M. Sadakane, T. Sano, J. *Nanosci. Nanotechnol.* 13 (2013) 3020.

Chapter 5

Role of structural similarity between starting zeolite and product zeolite in the interzeolite conversion process

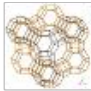




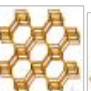

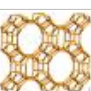
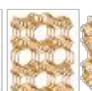
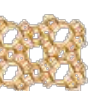















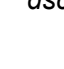






1. Introduction

Zeolites have regular microporous structures and desirable properties such as a solid acidity, high surface area, and molecular sieving and ion-exchange abilities. Therefore, they have been widely used in adsorption, catalysis, and ion-exchange applications. In general, zeolites are synthesized by hydrothermal treatment in the presence of organic structure-directing agents (OSDAs). OSDAs must be removed from the final zeolite, because, OSDAs end up occluding the cages and pores in them. The removing method was generally used calcination at high temperatures, which generates harmful gaseous pollutants. Furthermore, the use of expensive OSDAs also increases the cost of zeolite. As a result, OSDA-free zeolite synthesis using seed crystals has been desirable, and several research groups have succeeded in the OSDA-free synthesis of ZSM-5 (MFI), ECR-1 (EON), ZSM-34 (ERI/OFF), *BEA, RTH, ZSM-12 (MTW), and EMT zeolites [1–10].

I previously reported the OSDA-free synthesis of zeolites using the so-called interzeolite conversion method, using it to achieve the OSDA-free FAU to *BEA, FAU to LEV, and FAU to MAZ interzeolite conversions in the presence of seed crystals [11–13]. The use of FAU zeolite as the starting material resulted in a crystallization rate

superior to that achieved with conventional zeolite synthesis, in which amorphous aluminosilicate gel is used as the starting material. The enhanced crystallization rate was due to the decomposition/dissolution of the starting zeolite species, which generated locally ordered aluminosilicate species (nanoparts), which in turn assembled and transformed into a different type of zeolite [14]. Table 5-1 lists the framework structures and composite building units of several zeolites as summarized in the database of the Structure Commission of the International Zeolite Association [15]. In the seed-assisted OSDA-free zeolite synthesis, Itabashi et al. have proposed that the common composite building units between the seed zeolite and the finally crystallized zeolite from the seed-free starting gel are the crucial precursors for crystal growth [16]. The starting FAU zeolite contains the composite building units *sod* and *d6r*, the final LEV zeolite contains *d6r* (the common building unit with FAU zeolite), *BEA zeolite contains *mor*, *bea*, and *mtw*, and MAZ contains the *dsc* and *gme* units. Although it seems that there is no common composite building unit between FAU and *BEA or

Table 5-1 Framework structures and composite building units of various zeolites.

Framework type-code	FAU	*BEA	LEV	MAZ	CHA	GIS	LTL	MOR	FER	MFI
Framework structure										
Composite building unit	 <i>sod</i>  <i>d6r</i>	 <i>mor</i>  <i>bea</i>  <i>mtw</i>	 <i>d6r</i>	 <i>dsc</i>  <i>gme</i>	 <i>d6r</i>  <i>cha</i>	 <i>gis</i>  <i>dcc</i>	 <i>d6r</i>  <i>can</i>  <i>ltl</i>  <i>dsc</i>	 <i>mor</i>	 <i>fer</i>	 <i>mor</i>  <i>mel</i>  <i>mfi</i>  <i>cas</i>

FAU and MAZ, a common four-membered ring (4MR) chain is observed in the composite building units of *d6r*, *bea*, *dsc*, and *gme*, which serves as the common building unit. These results strongly suggest that structural similarity between the starting zeolite (FAU) and the final crystallized zeolite (BEA, LEV, and MAZ) is the crucial factor for zeolite crystal growth. I recently confirmed the validity of this hypothesis through our finding that the LEV–CHA transformation proceeded in the absence of both OSDAs and seed crystals [17]. I proposed a mechanism for the conversion based on the fact that LEV- and CHA zeolites have the common composite building unit of *d6r*, which under those particular hydrothermal conversion conditions led to the formation of locally ordered aluminosilicate species from the starting LEV zeolite. These species are similar to those of the CHA zeolite precursors, resulting in selective formation of CHA zeolites. This finding strongly suggests that transformations between zeolites having common composite building units are possible without the use of OSDAs.

To further understand the interzeolite conversion process, I examined the interzeolite conversion of FAU- and *BEA zeolites in the absence of OSDA under various hydrothermal conditions. I also attempted to synthesize MFI zeolite by interzeolite conversion of *BEA zeolite in the absence of OSDA and seed crystals. Both *BEA- and MFI zeolites are composed of 4 and 5 MRs, and have the common composite building unit of *mor*, which I hypothesized would enable successful transformation from one to the other.

2. Experimental

2.1 Hydrothermal conversion of FAU- and *BEA zeolites

FAU and *BEA zeolites with various Si/Al ratios were prepared from NH₄-Y zeolite (Si/Al = 2.8, Tosoh Co., Japan) and H-*BEA zeolite (Si/Al = 21, Tosoh Co., Japan) via dealumination through steaming and/or H₂SO₄ treatment, respectively. Hydrothermal conversion of the zeolite was carried out by adding the starting zeolite to an aqueous solution of alkaline metal (sodium or potassium) hydroxide. The mixture was placed into a 30-ml Teflon-lined stainless steel autoclave. Hydrothermal conversion was conducted at 70–170 °C for 30 min–7 days in a convection oven under autogenous pressure and static conditions. After crystallization, the solid product was collected by centrifugation and washed thoroughly with deionized water until a near neutral pH was achieved, and then dried overnight at 70 °C. The yield of product was estimated according to the following formula:

$$\text{Yield (\%)} = \frac{\text{Product (g)} - \text{Seeds (g)}}{\text{Starting Si \& Al sources (g)}} \times 100$$

2.2 Characterization

Powder X-ray diffraction (XRD) patterns of the solid products were collected using a Rigaku Mini Flex diffractometer with curved-graphite monochromatized Cu-K α radiation operated at 30 kV and 15 mA. Bulk Si/Al ratios were determined using inductively coupled plasma optical emission spectroscopy (ICP, Seiko SPS7000). The crystal morphology was observed using scanning electron microscopy (SEM, HITACHI S-4800). Nitrogen adsorption isotherms at -196 °C were obtained using a conventional volumetric apparatus (Bel Japan, BELSORP-mini).

3. Results and discussion

3.1 Hydrothermal conversion of FAU zeolite in the presence of alkaline metal cations

Interzeolite conversion of FAU zeolites was conducted using only alkaline metal hydroxides (MOH; NaOH or KOH). When NaOH was employed as both an alkali source and an inorganic SDA, GIS zeolite was obtained from FAU with a Si/Al ratio of 25 (Table 2, sample no. 1). On the other hand, LTL zeolite was obtained when KOH was

Table 5-2 Hydrothermal conversion of FAU-type zeolite and products obtained^a.

Sample no.	Starting materials	Si/Al ratio	MOH/SiO ₂	Temp./ °C	Products	Yield /%
1	FAU	25	0.6 (NaOH)	125	GIS	15
2	Cab-o-sil M5/NaAlO ₂	26	0.6 (NaOH)	125	Am. ^b	
3	FAU	25	0.6 (KOH)	125	LTL	18
4	Cab-o-sil M5/NaAlO ₂	26	0.6 (KOH)	125	Am. ^b	
5	FAU	76	0.6 (NaOH)	125	MOR	26
6	FAU	25	0.6 (NaOH)	140	MOR, GIS	
7	Cab-o-sil M5/NaAlO ₂	25	0.6 (NaOH)	140	MOR, GIS	

^a H₂O/SiO₂ = 15, Time = 7 days

^b Am.: amorphous phase

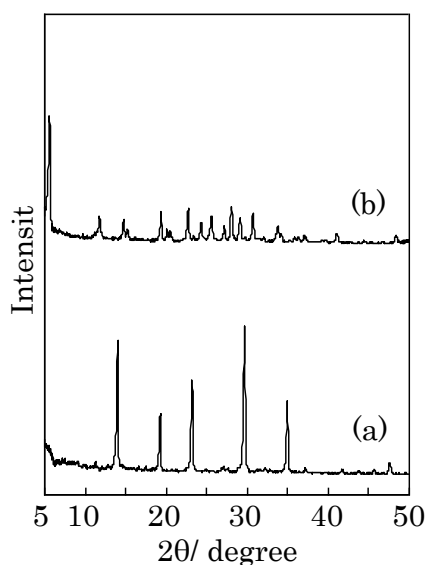


Fig. 5-1 XRD patterns of zeolites obtained. Sample nos. (a) 1 and (b) 3.

instead of NaOH (sample no. 3). As shown in Figure 5-1, there were no detectable peaks corresponding to by-products in the XRD patterns of these products. For comparison, zeolite synthesis was carried out via conventional hydrothermal synthesis using Cab-o-sil M5 and NaAlO₂ as the initial Si and Al sources, but no zeolite phase was obtained (sample nos. 2 and 4). GIS zeolite contains the composite building units *dcc* and *gis*, whereas LTL zeolite contains *d6r*, *can*, *ltl*, and *dsc* units; except for *d6r*, most of composite building units do not overlap, suggesting that interzeolite conversion would not occur. However, a 4MR chain is present in these composite building units that serves as the common element, suggesting that locally ordered aluminosilicate species (nanoparts) formed from the starting FAU zeolite in the presence of Na⁺ and K⁺ cations are similar to GIS- and LTL zeolite precursors, respectively. Specifically, the structural similarity between the starting and product zeolites is the critical factor in the interzeolite conversion. Sano's group already reported that the interzeolite conversion strongly depended on the Si/Al ratio of the starting FAU zeolite [11–13,17]. From the interzeolite conversion of FAU zeolite with higher Si/Al ratios, MOR zeolite was obtained instead of GIS- and LTL zeolites (sample no. 5). MOR zeolite was also formed at higher temperature (sample no. 6). Because the initial amorphous gel prepared from Cab-o-sil M5 and NaAlO₂ also gave MOR zeolite and there was no common composite building unit between FAU- and MOR zeolites, it is suggested that the structures of the nanoparts produced from FAU zeolite with high Si/Al ratios or under high-temperature conditions could be similar to those of aluminosilicate species derived from amorphous aluminosilicate gel. This would be possible only if extensive decomposition of the starting FAU zeolite occurred.

Table 5-3 Hydrothermal conversion of FAU-type zeolite in the presence of FER seed crystals^a

Sample no.	Starting materials Si/Al = 25	Temp. /°C	Products	Yield /%
8	FAU	150	FER	30
9	Cab-o-sil M5/NaAlO ₂	150	FER	18
10	FAU	125	GIS	19
11	Cab-o-sil M5/NaAlO ₂	125	FER	20

^a NaOH/SiO₂ = 0.6, H₂O/SiO₂ = 15, FER seed = 9.1 wt%,
Time = 1 day

To further confirm the importance of this structural similarity, hydrothermal conversion of FAU zeolite was carried out in the presence of FER seed crystals with a Si/Al ratio of 25. There is no structural similarity between FAU and FER zeolites (Table 5-1). Although FAU–FER interzeolite conversion occurred at 150 °C (Table 5-3, sample no. 8), only GIS phase was observed at 125 °C (sample nos. 10) even in the presence of FER seed crystals. In contrast, in the case of amorphous materials, FER zeolite was obtained regardless of synthesis temperature (sample nos. 9 and 11). These results indicate that the structure of the nanoparts produced by decomposition/dissolution of FAU zeolite is strongly dependent on synthesis conditions such as Si/Al ratio and temperature. Under mild hydrothermal condition (125 °C), nanoparts with a 4MR chain structure were produced from the starting FAU zeolite, resulting in the formation of GIS zeolite through the assembly of these nanoparts. However, at high temperature (150 °C), FAU zeolite significantly decomposed to yield aluminosilicate species similar to those formed from the amorphous starting materials. As the structure of the aluminosilicate species was rather similar to that of the 5MR-containing precursor of FER zeolite, it was likely incorporated into the FER seed crystals.

3.2 Hydrothermal conversion of *BEA zeolite in the presence of alkaline metal cations

As described above, *BEA zeolite contains the composite building units *mor*, *bea*, and *mtw*, which are composed of 4 and 5MRs. It is reasonable to conclude that the transformation behavior of *BEA zeolite is different from FAU zeolite[18]. Therefore, I investigated the transformation behavior of *BEA zeolite in the absence of OSDA under various synthesis conditions. On the basis of the above results of hydrothermal conversion of FAU zeolite, the NaOH/SiO₂ and H₂O/SiO₂ ratios were fixed at 0.6 and 15, respectively. As indicated in Table 5-4, although *BEA zeolite did not decompose completely even 7 days into the synthesis, MOR zeolite phase was observed (sample no. 12). This suggested that the starting *BEA zeolite was stable under these hydrothermal synthesis conditions, and that the formation of MOR zeolite was due to the common composite building unit *mor*. I previously reported the OSDA-free synthesis of LEV

Table 5-4 Hydrothermal conversion of *BEA-type zeolite^a.

Sample no.	Starting materials	Si/Al ratio	Seed (wt%)	Temp. /°C	Time /days	Products	Yield /%
12	*BEA	21	-	125	7	*BEA,MOR	
13	*BEA	21	LEV(16.7)	125	3	LEV,MOR	
14	*BEA	21	-	70	14	Am. ^b	
15	*BEA	21	MAZ(33.3)	70	14	MAZ	18
16	*BEA	21	FER(9.1)	125	1	FER	20
17	FAU	19	LEV(16.7)	125	3	LEV	26
18	FAU	17	MAZ(33.3)	70	14	MAZ	34

^a NaOH/SiO₂ = 0.6, H₂O/SiO₂ = 15

^b Am.: amorphous phase

and MAZ zeolites by interzeolite conversion of FAU zeolite in the presence of seed crystals [12,13]. Based on this finding, I investigated the effect of adding seed crystals

on the OSDA-free interzeolite conversion of *BEA zeolite. The addition of LEV seed crystals led to the formation of LEV zeolite. However, MOR zeolite was found coexisting in the product (sample no. 13). Conversely, when MAZ seed crystals were used, pure MAZ zeolite was successfully obtained, although the yield was lower than that obtained by interzeolite conversion of FAU zeolite (sample nos. 15 and 18). FAU, LEV, and MAZ zeolites contain composite building units composed of mainly 4MRs, whereas *BEA- and MOR zeolites contain those composed with 4 and 5MRs. It appears that compared to *BEA zeolite, FAU zeolite yields many 4MR-containing composite building units via its decomposition. Therefore, the difference in the yield of MAZ zeolite between interzeolite conversion starting with FAU- and *BEA zeolites is due to the difference in the amount of available 4MR-based building units.

If my hypothesis is correct, *BEA zeolite is suitable for the synthesis of zeolites containing only 5MR-based composite building units. In order to confirm this, interzeolite conversion of *BEA zeolite was carried out at 125 °C in the presence of FER seed crystals, which contained the fer composite building unit with 5MRs only. As expected, pure FER zeolite was obtained (sample no. 16). The yield of FER zeolite was consistent with that obtained by conventional hydrothermal synthesis using Cab-o-sil M5/NaAlO₂ (sample nos. 11 and 16). From these results, I concluded that the structures of nanoparts could be altered through the choice of starting zeolite, implying the possibility of zeolite synthesis by selective assembly of building units with specific structures.

3.3 *BEA–MFI interzeolite conversion

MFI zeolite contains the composite building units *cas*, *mel*, *mfi*, and *mor* composed of 4 and 5MRs, meaning that the *mor* unit is the common building unit between *BEA- and MFI zeolites. On this basis, I attempted to synthesize MFI zeolite by interzeolite conversion of *BEA zeolite in the absence of both OSDA and seed crystals. As expected, *BEA–MFI interzeolite conversion was observed when *BEA zeolites with high Si/Al ratios were employed as the starting material. Typical results are summarized in Table 5. MFI zeolites were obtained after just 2 h of synthesis time (sample nos. 19 and 22) in a yield of ~7–16% based on the weight of the starting *BEA zeolite. When using *BEA zeolites with low Si/Al ratios, the starting *BEA did not completely decompose (sample no. 25). Moreover, it was found that MFI zeolite was not obtained when FAU zeolite or

Table 5-5 *BEA–MFI interzeolite conversion^a.

Sample no.	Starting materials (Si/Al)	NaOH/ SiO ₂	H ₂ O/ SiO ₂	Time /h	Product	Bulk Si/Al	Yield /%
19	*BEA(87)	0.4	10	2	MFI		6.9
20	*BEA(87)	0.4	15	24	MFI		13.1
21	*BEA(87)	0.4	20	24	Am. ^b		
22	*BEA(76)	0.4	15	2	MFI	15	15.8
23	*BEA(76)	0.6	10	2	No product		
24	*BEA(53)	0.6	15	24	MFI	9.0	8.7
25	*BEA(21)	0.6	15	24	*BEA,Am. ^b		
26	FAU(76)	0.4	15	24	Am. ^b		
27	FAU(76)	0.6	15	24	MOR		
28	Cab-o-sil/NaAlO ₂ (53)	0.6	15	24	No product		

^a Temp. = 125 °C

amorphous aluminosilicate gel (Cab-o-sil M5 and NaAlO₂) was used as the starting materials (sample nos. 26 and 27). Taking together, these results imply that nanoparticles produced by the dissolution/decomposition of *BEA zeolites contribute to the

nucleation and crystal growth of MFI zeolites. The *BEA–MFI interzeolite conversion was, furthermore, strongly dependent on the alkalinity of the medium. Under mild alkaline conditions, no MFI phase was observed (sample no. 21), whereas under strong alkaline conditions, no product was obtained at all (i.e., *BEA zeolite was completely dissolved without subsequent transformation; sample no. 23). The Si/Al ratio of the obtained MFI zeolite (Si/Al = 9.0–15) was considerably lower than that of the starting *BEA zeolite due to the high NaOH concentration, which caused an increase in the silicon concentration of the liquid phase.

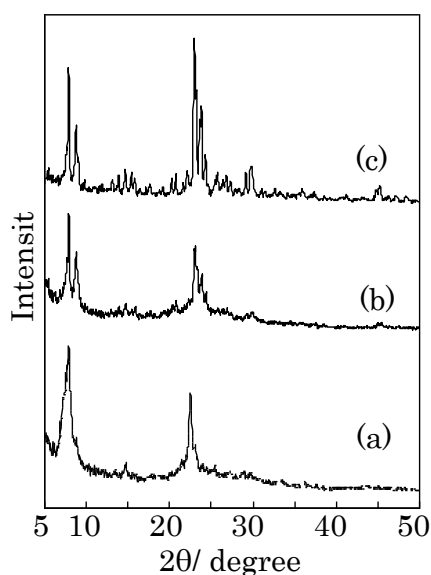


Fig. 5-2 XRD patterns of (a) starting *BEA and MFI zeolites obtained at synthesis times of (b) 30 min and (c) 24 h under NaOH/SiO₂ = 0.4 and H₂O/SiO₂ = 15.

Figure 5-2 shows the XRD patterns of MFI zeolites after reaction times of 30 min and 24 h. Interestingly, MFI zeolite was obtained after just 30 min, the crystallinity of which was found to increase with increasing length of reaction time. As shown in Figure 5-3, the outer surfaces of the MFI crystals were very rough, and a large number of

macropores were observed. With increasing hydrothermal treatment time, however, the surface became smoother. Figure 5-4A shows the N₂ adsorption-desorption isotherms of MFI zeolites obtained at varying reaction times. A clear hysteresis loop was observed for MFI zeolite obtained after 6 h, but at longer reaction times (i.e., at 12 and 24 h), the hysteresis loop became less pronounced, and the BET specific surface areas and pore volumes decreased (6 h: 510, 12 h: 480, and 24 h: 370 m²·g⁻¹, and 6 h: 0.31, 12 h: 0.27, and 24 h: 0.17 cm³·g⁻¹, respectively). Mesopore size analysis by the BJH method yielded broad peaks of 2 to 4 nm (Figure 5-4B). The number of mesopores decreased with increasing synthesis time, indicating the elimination of mesopores by the crystal growth of the MFI zeolite.

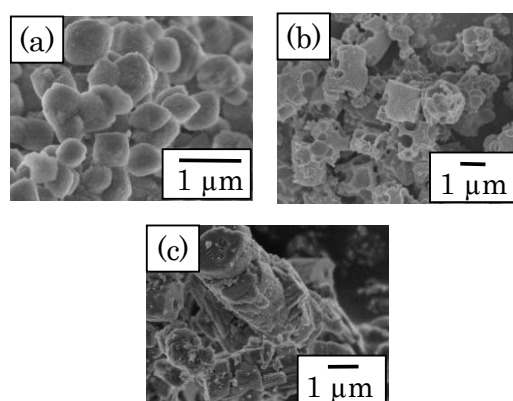


Figure 5-3 SEM images of (a) starting *BEA and MFI zeolites obtained at synthesis times of (b) 30 min and (c) 24 h under NaOH/SiO₂ = 0.4 and H₂O/SiO₂ = 15.

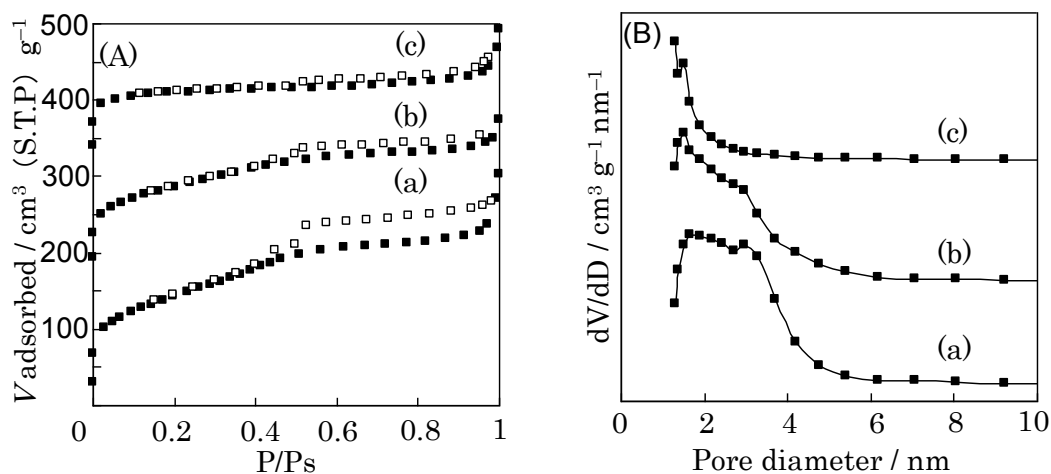


Fig. 5-4 (A) N_2 adsorption-desorption isotherms and (B) BJH pore size distributions of MFI-type zeolites obtained at synthesis times of (a) 6 h, (b) 12 h, and (c) 24 h under $\text{NaOH}/\text{SiO}_2 = 0.4$ and $\text{H}_2\text{O}/\text{SiO}_2 = 15$.

From the results presented above, I concluded that mesoporous MFI zeolites with high aluminum content could be readily synthesized from *BEA zeolites by the interzeolite conversion method. The creation of mesoporous zeolites has been actively sought as a way to overcome the diffusion limitation of reagents and products. There are several approaches for synthesizing mesoporous zeolites, such as the use of carbon particles as hard templates [19], the use of organosilane surfactants as soft templates [20], and, more recently, the desilication method [21]. However, all these approaches require multiple steps, unlike the method we have presented here. Therefore, the interzeolite conversion method provides a new route for creating mesopores in zeolites, while this *BEA–MFI interzeolite conversion requires preparation of starting zeolite and was low yield.

Having obtained mesoporous MFI zeolite with high aluminum content, we investigated its catalytic potential in the dehydration of lactic acid to acrylic acid. The dehydration reaction was carried out on Na^+ ion-exchanged mesoporous MFI zeolite (NaMFI, $\text{Si}/\text{Al}=15$) using a fixed-bed reactor at atmospheric pressure. Acrylic acid is a

useful raw material in the petrochemical industry, while lactic acid is a major product of biomass fermentation, making conversion of the latter into the former a desirable transformation. Before reaction, the catalyst (20 mg) was heated at 380 °C for 5 h under a flow of argon. The reaction was then performed at 350 °C by introducing an aqueous solution of lactic acid (3.5 wt%) into the argon flow (40 ml·min⁻¹). The catalytic performance of the MFI zeolite was compared with that of NaY (Si/Al = 2.8, JGC

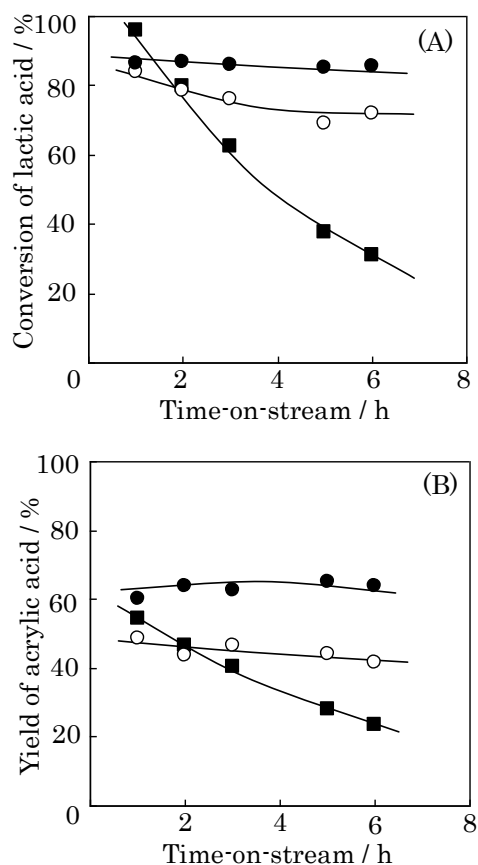


Fig. 5-5 (A) Conversion of lactic acid and (B) yield of acrylic acid over NaMFI and NaY catalysts. (○) : mesoporous NaMFI obtained at NaOH/SiO₂ = 0.4, H₂O/SiO₂ = 15, and synthesis time = 12 h, (●) : non-mesoporous NaMFI, (■) : NaY

Catalysts & Chemicals Ltd. Co., Japan), which typically exhibits excellent performance in the dehydration of lactic acid to acrylic acid [22]. As shown in Figure 5-5, although the initial lactic acid conversion for NaY was approximately 10% higher than that of NaMFI, deactivation of the NaY catalyst was observed at later time points, due to poisoning of active sites by the accumulation of carbonaceous deposits. On the other hand, only a slight decrease in lactic acid conversion was observed for the NaMFI catalyst. Similar behavior was observed for the production of acrylic acid using these catalysts. Indeed, a large difference in the amount of carbonaceous deposits after 6 h of time-on-stream was observed by thermogravimetric analysis: 4.2% for NaMFI and 21.7% for NaY. In addition, XRD analysis of the NaMFI catalysts after reaction confirmed that no structural collapse of NaMFI had occurred. Together, these results suggest that the mesoporosity of the NaMFI catalyst confers upon it superior catalytic stability through resistance to poisoning of active sites from the accumulation of carbonaceous deposits.

4. Conclusion

The interzeolite conversion process was investigated using FAU and *BEA zeolites in the absence of OSDA under various conditions. FAU zeolite contains the composite building units *sod* and *d6r*, which are composed of 4MRs. On the other hand, *BEA zeolite contains the composite building units *mor*, *bea*, and *mtw*, which are composed of 4 and 5MRs. Under mild hydrothermal conditions, FAU–GIS and FAU–LTL interzeolite conversions occurred when NaOH and KOH were used as alkali sources, respectively. Under severe conditions such as high temperature, MOR zeolite was obtained instead of GIS and LTL zeolites. Because MOR zeolite was obtained from amorphous hydrogel

prepared using Cab-o-sil M5/ NaAlO_2 , and there are no common composite building units between FAU- and MOR zeolites, I have concluded that the structural similarity between the starting zeolite and the final crystallized zeolite is the crucial factor for interzeolite conversion. This hypothesis was also confirmed by successful *BEA–MFI interzeolite conversion. The obtained mesoporous MFI zeolites with high aluminum content exhibited excellent catalytic performance for the dehydration of lactic acid to acrylic acid. These results confirm that the interzeolite conversion route is an alternative strategy for zeolite synthesis.

However, to establish the interzeolite conversion route as an alternative zeolite synthesis method, I must further characterize the chemical structures of the locally ordered aluminosilicate species generated from the starting zeolite. These studies are currently in progress.

References

- [1] V. P. Shiralkar and A. Clearfield, *Zeolites* 9 (1989) 363
- [2] N. Ren, Z.-J. Yang, X.-C. Lv, J. Shi, Y.-H. Zhang and Y. Tang, *Micropor. Mesopor. Mater.* 131 (2010) 103
- [3] J. Song, L. Dai, Y. Ji and F.-S. Xiao, *Chem. Mater.* 18 (2006) 2775
- [4] Z. Wu, J. Song, L. Ren, Y. Ji, J. Li and F.-S. Xiao, *Chem. Mater.* 20 (2008) 357
- [5] B. Xie, J. Song, L. Ren, Y. Ji, J. Li and F.-S. Xiao, *Chem. Mater.* 20 (2008) 4533
- [6] G. Majano, L. Delmotte, V. Valtchev and S. Mintova, *Chem. Mater.* 21 (2009) 4184
- [7] Y. Kamimura, W. Chaikitlisilp, K. Itabashi, A. Shimojima and T. Okubo, *Chem. Asian J.* 5 (2010) 182
- [8] T. Yokoi, M. Yoshioka, H. Imai and T. Tatsumi, *Angew. Chem. Int. Ed.* 48 (2009) 9884
- [9] K. Iyoki, Y. Kamimura, K. Itabashi, A. Shimojima and T. Okubo, *Chem. Lett.* 39 (2010) 730
- [10] E.-P. Ng, D. Chateigner, T. Bein, V. Valtchev and S. Mintova, *Science* 335 (2012) 70
- [11] K. Honda, A. Yashiki, M. Itakura, Y. Ide, M. Sadakane and T. Sano, *Micropor. Mesopor. Mater.* 142 (2011) 161
- [12] A. Yashiki, K. Honda, A. Fujimoto, S. Shibata, Y. Ide, M. Sadakane and T. Sano, *J. Cryst. Growth* 325 (2011) 96
- [13] A. Yashiki, A. Fujimoto, S. Shibata, H. Koutaro, M. Itakura, Y. Ide, M. Sadakane and T. Sano, 5th International FEZA Conference, SC-P-012-Mon-012 (2011)
- [14] H. Jon, N. Ikawa, Y. Oumi and T. Sano, *Chem. Mater.* 20 (2008) 4135
- [15] International Zeolite Association Web site: <http://www.iza-online.org/>.

- [16] K. Itabashi, Y. Kamimura, K. Iyoki, A. Shimojima and T. Okubo, *J. Am. Chem. Soc.* 134 (2012) 11542
- [17] I. Goto, M. Itakura, S. Shibata, Y. Ide, M. Sadakane and T. Sano, *Micropor. Mesopor. Mater.* 158 (2012) 117
- [18] M. Itakura, K. Ota, S. Shibata, T. Inoue, Y. Ide, M. Sadakane and T. Sano, *J. Cryst. Growth* 314 (2011) 274
- [19] C. J. Jacobsen, C. Madsen, J. Houzvicka, I. Schmidt and A. Carlsson, *J. Am. Chem. Soc.* 122 (2000) 7116
- [20] M. Choi, H. S. Cho, R. Srivastava, C. Venkatesan, D.-H. Choi and R. Ryoo, *Nat. Mater.* 5 (2006) 718
- [21] M. Ogura, S. Shinomiya, J. Tateno, Y. Nara, E. Kikuchi and M. Matsukata, *Chem. Lett.* (2000) 882
- [22] H. Wang, D. Yu, P. Sung, J. Yan, Y. Wang and H. Huang, *Catal. Commun.* 9 (2008) 1799

Chapter 6

Transformation of LEV zeolite into less dense CHA zeolite

1. Introduction

In general, medium/large pore size and high-silica zeolites are synthesized by hydrothermal treatment of amorphous aluminosilicate gel as a starting material in the presence of organic structure-directing agents (OSDAs). The use of OSDAs is, however, undesirable from a practical point of view, because of their high cost as well as their large environmental impact. As a consequence of these drawbacks, the synthesis of zeolites from seed crystals without the use of OSDAs has attracted considerable attention, and several research groups have already succeeded in the OSDA-free synthesis of ECR-1 [1], ZSM-34 [2], *BEA [3–5], RTH [6], ZSM-12 [7] and EMT [8] zeolites.

In the synthesis of most zeolites, an amorphous phase is converted directly to a given type of zeolite. Because zeolites are metastable, however, a sequence from the amorphous phase to a less stable zeolite to the most stable zeolite is often observed. In other words, a less stable zeolite crystallizes in a kinetically controlled process, and the transformation to the most stable zeolite is thermodynamically driven. Theoretical calculations and calorimetric measurements have suggested that the stability of zeolites decreases as their porosity increases, that is, as the zeolite framework density decreases

[9,10]. On this basis, several research groups have pointed out the high potential of an alternative method for zeolite formation, i.e., the hydrothermal conversion of one zeolite type into another (interzeolite conversion) [11–13].

Recently, Sano's group has also investigated the potential of interzeolite conversion and has succeeded in synthesizing several types zeolites, such as *BEA, RUT, CHA, LEV, MTN, and OFF zeolites using FAU zeolite as the starting material in the presence of various OSDAs [14–19]. Among the zeolites synthesized, LEV and CHA zeolites have attracted considerable interest because their structures have eight-membered ring pores ($4.8 \times 3.6 \text{ \AA}$) and because they show shape-specific selectivity for the conversion of methanol or ethanol into light olefins such as ethylene and propylene. The use of FAU zeolite as a starting material for the preparation of other zeolites, in the presence of choline hydroxide as a structure-directing agent for LEV zeolite and benzyltrimethylammonium hydroxide as a structure-directing agent for CHA zeolite, results in a crystallization rate that is superior to that achieved in the conventional synthesis using amorphous aluminosilicate gel as the starting material. This enhanced crystallization rate arises because the decomposition/dissolution of the starting zeolite generates locally ordered aluminosilicate species (nanoparts) that assemble and evolve into another type of zeolite [20].

In addition to the successful interzeolite conversions achieved using OSDAs, I very recently succeeded in OSDA-free FAU-*BEA and FAU-LEV transformations using corresponding noncalcined seed crystals [21,22]. Although the seed crystals employed contained OSDA cations in the zeolitic pores, no additional OSDAs were added into the starting gels. The OSDA cations in the zeolitic pores stabilized the seed crystals, and, consequently, the crystal surfaces of the seed crystals contributed to the crystal growth

of the *BEA and LEV zeolites. An investigation of the framework structures of these FAU, *BEA, and LEV zeolites, revealed that there is a similar building unit in their frameworks, the linear connection of four-membered rings.

Taking into account the fact that LEV and CHA zeolites have similar composite building units, because the two zeolites both belong to the chabazite group, the above results strongly suggest that it is possible to synthesize CHA (LEV) zeolite without the use of either OSDAs or seed crystals, if the starting LEV (CHA) zeolite is decomposed/dissolved into locally ordered aluminosilicate species (nanoparts) whose chemical structures are suitable for the crystallization of CHA (LEV) zeolite. This process would just involve reassemble of the nanoparts. Therefore, I applied the interzeolite conversion method to the OSDA-free, seed-crystal-free synthesis of CHA zeolite with a framework density (FD) of 15.1 T/1000 Å³ from LEV zeolite with a FD of 15.9 T/1000 Å³. That is, I transformed LEV zeolite into more less dense CHA zeolite. The possibility of transforming zeolite into less dense zeolites, for example, transforming ANA zeolite (FD = 19.2 T/1000 Å³) into KFI zeolite (FD = 15 T/1000 Å³), has already reported by Barrer [23]. However, this report did not provide information concerning the details of the transformation behaviour. Very recently, Zicovich-Wilson et al. reported the transformation of TON zeolite (FD = 18.1 T/1000 Å³) into less dense ITW zeolite (FD = 17.7 T/1000 Å³), although this transformation required both 1,3,4-trimethylimidazolium and fluoride ions [24]. Tian et al. also reported the phase transformation synthesis of SAPO-34 from SAPO-5 using dimethylamine [25]. To my knowledge, this is the first report on the transformation of LEV zeolite into less dense CHA zeolite without the use of either seed crystals or OSDAs.

2. Experimental

2.1 Synthesis of starting LEV

To produce the starting material, LEV zeolites with various Si/Al ratios were synthesized from FAU zeolites with different Si/Al ratios using choline hydroxide as a OSDA according to the procedure described in the previous report [17]. The obtained LEV zeolites were calcined at 450 °C for 48 h to remove choline cations from the zeolitic pores. The prepared LEV zeolites had a well-defined LEV structure, as demonstrated by the XRD pattern (Figure 1(a)). No diffraction peaks other than those of the LEV phase were observed. As can be seen in Figure 2(a), SEM observations revealed a round morphology of the LEV zeolite (Sample no. 1). The BET surface area and micropore volume were calculated to be 560 m² g⁻¹ and 0.26 cm³ g⁻¹, respectively.

2.2 Hydrothermal conversion of LEV to CHA

Hydrothermal conversion of LEV zeolite into CHA zeolite was carried out by adding the prepared LEV zeolite to an aqueous solution of MOH (M: alkaline metal). The mixture was placed into a 30-cm³ Teflon-lined stainless steel autoclave. Hydrothermal conversion was conducted under static conditions at 90–200 °C for 1.5–24 h in a convection oven. The solid product was collected by centrifugation and washed thoroughly with deionized water until the pH was near neutral. Then, it was dried overnight at 70 °C. The details of the hydrothermal conversion conditions are listed in Table 6-1.

Table 6-1 Hydrothermal conversion of FAU and products obtained.

Sample no.	Synthesis conditions ^a				Product		
	Starting Si/Al ratio	NaOH/SiO ₂	Temp. / °C	Time /h	Phase ^b	Bulk Si/Al ratio	Yield /%
1	9	3.0	125	1.5	CHA	2.8	19
2	6	3.0	125	1.5	LEV		
3	12	3.0	125	1.5	CHA	2.6	21
4	22	3.0	125	1.5	No product		
5	9	3.0	170	1.5	CHA	3.1	20
6	9	3.0	200	1.5	ANA		
7	9	3.0	90	1.5	Am.		
8	9	3.0	90	12	CHA	4.9	20
9	9	3.0(LiOH)	125	1.5	Am. + Un.		
10	9	3.0(KOH)	125	1.5	Am.		
11	9	3.0(RbOH)	125	1.5	Am.		

^a H₂O/SiO₂ = 80

^b Am. = amorphous, Un. = unknown

2.3 Characterization

X-ray diffraction (XRD) patterns of the solid products were collected using a powder X-ray diffractometer (Rigaku, Mini Flex) with graphite-monochromatized Cu K α radiation at 30 kV and 15 mA. The bulk Si/Al ratios were determined using inductively coupled plasma optical emission spectroscopy (ICP, Seiko SPS7000). The crystal morphology was observed using scanning electron microscopy (SEM, Hitachi S-4800). The ²⁷Al magic angle spinning (MAS) NMR and ²⁹Si MAS NMR spectra were recorded at 104.2 MHz and 79.5 MHz, respectively, on a Varian 600PS solid NMR spectrometer, using a 3.2-mm-diameter zirconia rotor for ²⁷Al MAS NMR and a 6-mm-diameter zirconia rotor for ²⁹Si MAS NMR. The rotor was spun at 6 kHz for ²⁹Si MAS NMR and at 15 kHz for ²⁷Al MAS NMR. The spectra were acquired using 2.3 μ s pulses, a 1 s recycle delay, and 1000 scans for ²⁷Al MAS NMR and 5 μ s pulses, a 100 s recycle delay,

and 1000 scans for ^{29}Si MAS NMR. $\text{Al}(\text{NO}_3)_3 \cdot 9\text{H}_2\text{O}$ and $\text{Si}(\text{CH}_3)_4$ were used as chemical shift references for ^{27}Al and ^{29}Si MAS NMR, respectively. Prior to the ^{27}Al MAS NMR measurements, the samples were moisture-equilibrated over a saturated solution of NH_4Cl for 24 h. Nitrogen adsorption isotherms at -196°C were obtained using a conventional volumetric apparatus (Bel Japan, BELSORP-mini). Prior to the adsorption measurements, the samples (ca. 0.1 g) were evacuated at 400°C for 10 h.

3. Results and Discussion

3.1 Transformation of LEV into CHA

First, I investigated the transformation behavior of LEV zeolite with a Si/Al ratio of 9 (Sample no.1). Several preliminary experiments allowed the NaOH/SiO_2 and $\text{H}_2\text{O}/\text{SiO}_2$ ratios in the starting materials to be fixed at 3.0 and 80, respectively. Detailed synthesis conditions and characteristics of the products obtained are listed in Table 6-1. Figure 6-1 shows the XRD patterns of the products obtained by varying the hydrothermal treatment time. It is clear that the starting LEV zeolite decomposed into an amorphous phase and then the pure CHA zeolite crystallized after 1.5 h of hydrothermal treatment. As the treatment time increased, the peaks corresponding to the CHA phase decreased and the pure ANA zeolite was finally obtained after 24 h of hydrothermal treatment. In other words, a sequence from starting LEV \rightarrow an amorphous phase \rightarrow CHA \rightarrow ANA was observed. The diffraction pattern of the obtained CHA zeolite was typical of CHA structure and contained no impurity peaks from unconverted starting LEV zeolite or cocrystallized phases. This indicates that the less stable CHA zeolite crystallizes in a kinetically controlled process and that the transformation to the most stable ANA zeolite is thermodynamically driven. To the best of my knowledge, this is the first report on the

transformation of LEV zeolite into less dense CHA zeolite without the use of either seed crystals or OSDAs. The yield of CHA zeolite was 19 % based on the weight of the starting LEV zeolite. Figures 6-2(b) and 6-2(c) show SEM images of the obtained CHA zeolites. The crystal morphology was cubic, and the crystals were 200–400 nm in size, which is smaller than the crystal size of the starting LEV zeolite, as shown in Figure 6-2(a).

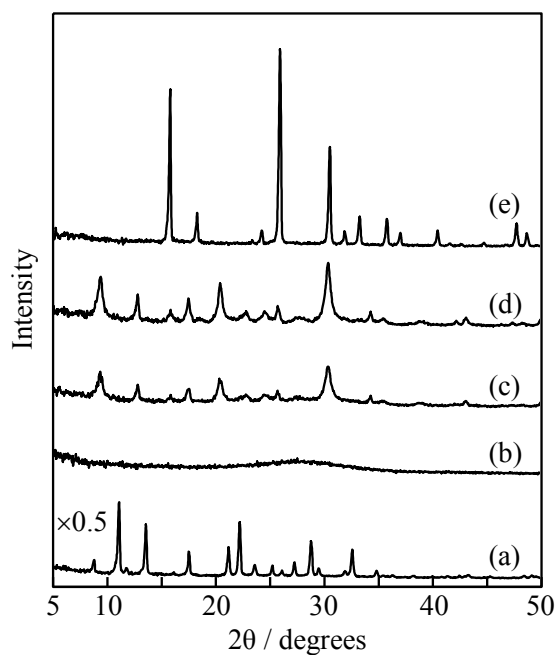


Fig. 6-1 XRD patterns of products obtained from LEV (Si/Al = 9) after various crystallization times. (a) Starting LEV and (b–e) products after (b) 0.5 h, (c) 1 h, (d) 1.5 h, and (e) 24 h.

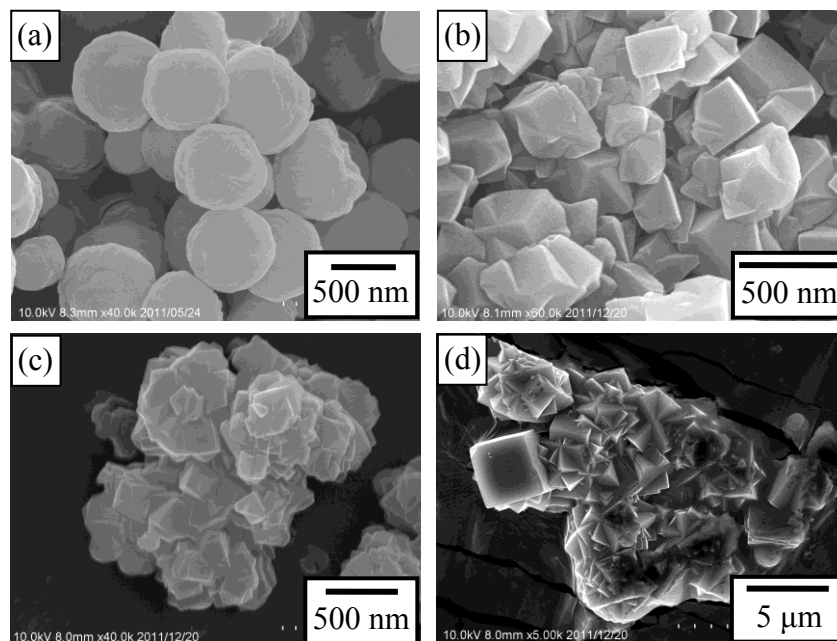


Fig. 6-2 SEM images of (a) starting LEV, (b) CHA ((Sample nos. 1), (c) CHA (Sample nos. 8), and (d) the obtained LTA.

The chemical state of the aluminum in the obtained CHA zeolite was investigated using ^{27}Al MAS NMR spectroscopy. As shown in Figure 6-3(a), the ^{27}Al MAS NMR spectrum of the CHA zeolite showed only the peak at approximately 56 ppm, corresponding to tetrahedrally coordinated framework aluminum species. No peak corresponding to octahedrally coordinated aluminum species (which is indicative of extra-framework aluminum species) was observed at around 0 ppm. This implies that all of the aluminum species existed within the zeolite framework in the CHA zeolite obtained by the hydrothermal conversion of LEV zeolite in the absence of any OSDAs or seed crystals. The ^{29}Si MAS NMR spectrum of the obtained CHA zeolite, presented in Figure 6-3(b), shows five peaks at -108 , -103 , -98 , -92 , and -88 ppm. These peaks can be assigned to Si(0Al), Si(1Al), Si(2Al), Si(3Al), and Si(4Al) species, respectively [26]. The existence of the Si(4Al) species indicates that the obtained CHA zeolite has

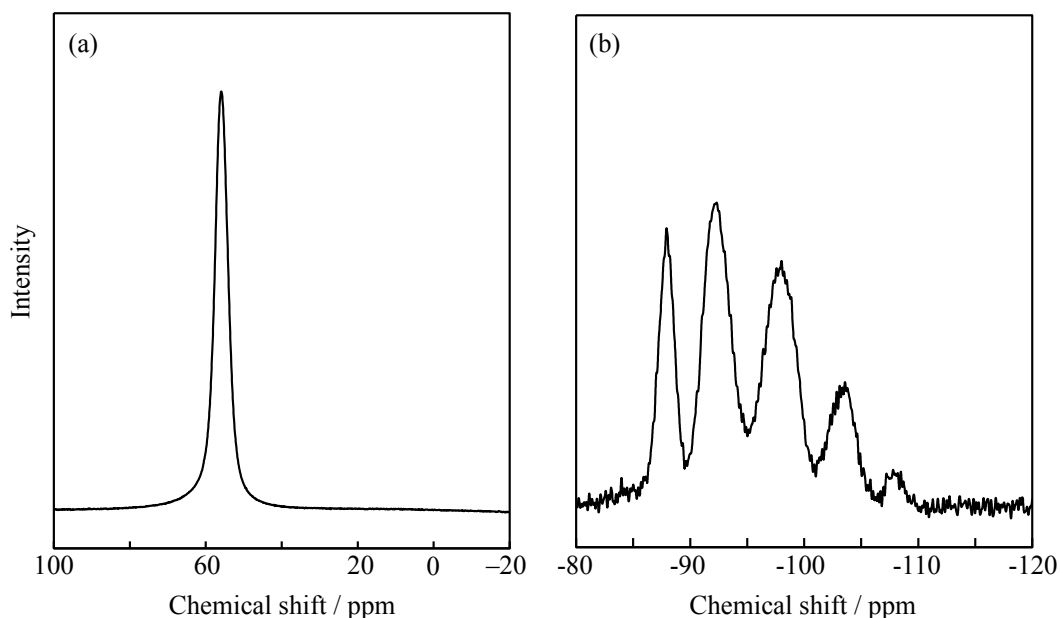


Fig. 6-3 (a) ^{27}Al and (b) ^{29}Si MAS NMR spectra of the obtained CHA (Sample no. 1).

a high aluminum content. The bulk Si/Al ratio measured using ICP was actually 1.8, which is considerably lower than that of the starting LEV zeolite (Si/Al = 9). This is probably a result of the highly alkaline conversion conditions, which caused an increase in the silicon concentration in the liquid phase.

As can be seen in Figure 6-4(a), the amount of nitrogen adsorbed on the Na^+ -ion-exchanged CHA zeolite was small. This is probably due to the pore blocking at particular locations by Na^+ -cations, which behave as charge compensators, or the presence of amorphous alumina and silica. Taking into account that there was no peak corresponding to octahedrally coordinated aluminum species at around 0 ppm

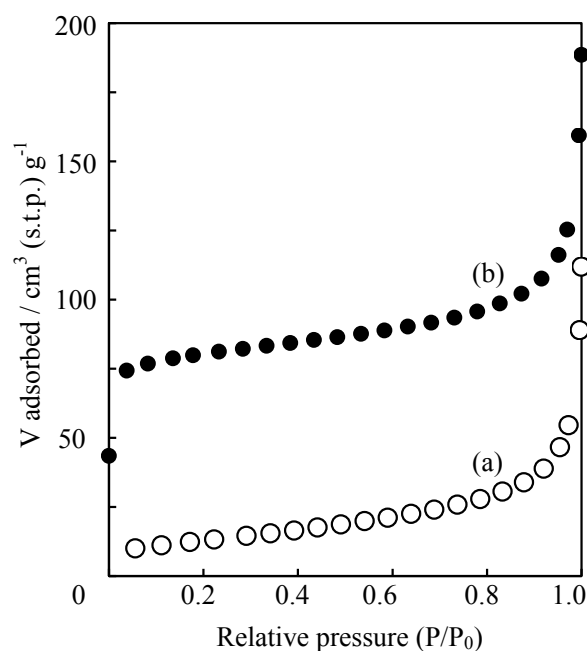


Fig. 6-4 N₂ adsorption isotherms of the obtained (a) Na⁺- and (b) Ca²⁺- form CHA-type zeolites.

(Figure 6-3(a)), the existence of amorphous material in the zeolite pores seems to be unlikely. On the other hand, the nitrogen adsorption isotherm of the Ca²⁺-ion-exchanged CHA zeolite can be classified as type I based on the IUPAC classification (Figure 6-4(b)), and the BET surface area and micropore volume were calculated to be 260 m² g⁻¹ and 0.12 cm³ g⁻¹, respectively. These values are slightly smaller than those of the CHA zeolite synthesized from FAU zeolite and KOH according to the recipe described in *Verified Syntheses of Zeolitic Materials* published by the International Zeolite Association, 340 m² g⁻¹ and 0.17 cm³ g⁻¹ [27].

Previous studies undertaken by Sano's group indicated that interzeolite conversion was strongly dependent on the Si/Al ratio of the starting zeolite [14–19]. Therefore, the influence of the Si/Al ratio of the starting LEV zeolite on the CHA zeolite synthesis was

investigated herein using LEV zeolites with various Si/Al ratios ($\text{Si/Al} = 6\text{--}22$). The results presented in Table 1 indicate that LEV zeolites with Si/Al ratios in the range of 9–12 could be converted into pure CHA zeolites by employing a synthesis time of 1.5 h (Sample nos. 1, 3, 5, and 8). The yield of LEV zeolite was ca. 20% regardless of the Si/Al ratio of the starting LEV zeolite. When LEV zeolite with a Si/Al ratio of 22 was used, no product was obtained because of the high alkalinity. In the case of LEV zeolite with a Si/Al ratio of 6, the starting zeolite hardly decomposed.

I then studied the influence of the synthesis temperature. When the hydrothermal conversion of LEV zeolite was carried out at 125–170 °C for 1.5 h, the LEV zeolite was transformed into CHA zeolite. At 200 °C, pure ANA zeolite was obtained, suggesting that CHA zeolite transformed into the most stable zeolite. At 90 °C pure CHA zeolite was obtained when the synthesis time was prolonged to 12 h. The morphology and crystal size of the LEV zeolite crystals obtained at 90 °C were similar to those obtained at 125 °C.

Finally, the influences of various types of alkaline metal cations were investigated. As shown in Table 6-1, when LiOH, KOH, and RbOH were employed instead of NaOH as an alkali source, the transformation of LEV zeolite did not occur (Sample nos. 9–11). Although I do not have enough data to explain this difference, I speculate that it occurs because the smaller Na^+ cation acts as structure-forming cation, whereas larger cations such as K^+ and Rb^+ cations act as structure-breaking cations [28]. At the present time, however, I cannot explain why the Li^+ cation had less structure-forming ability.

3.2 Effects of NaOH/SiO₂ and H₂O/SiO₂ ratios on transformation of LEV—Comparison with amorphous materials

In order to better understand the LEV-CHA transformation, the influences of the NaOH/SiO₂ and H₂O/SiO₂ ratios at a hydrothermal temperature of 125 °C were investigated. For comparison, zeolite synthesis was carried out by the conventional hydrothermal synthesis using Cab-o-sil M-5 and NaAlO₂ as the starting Si and Al sources. Figure 6-5 shows the reactant composition diagram for these zeolite syntheses, which were carried out at 125 °C for 1.5 h using LEV zeolite and amorphous material (Cab-o-sil M-5/NaAlO₂) as starting materials. This figure uses several symbols to stand for main the zeolite phases produced, and by-products are given below the main-product symbol.

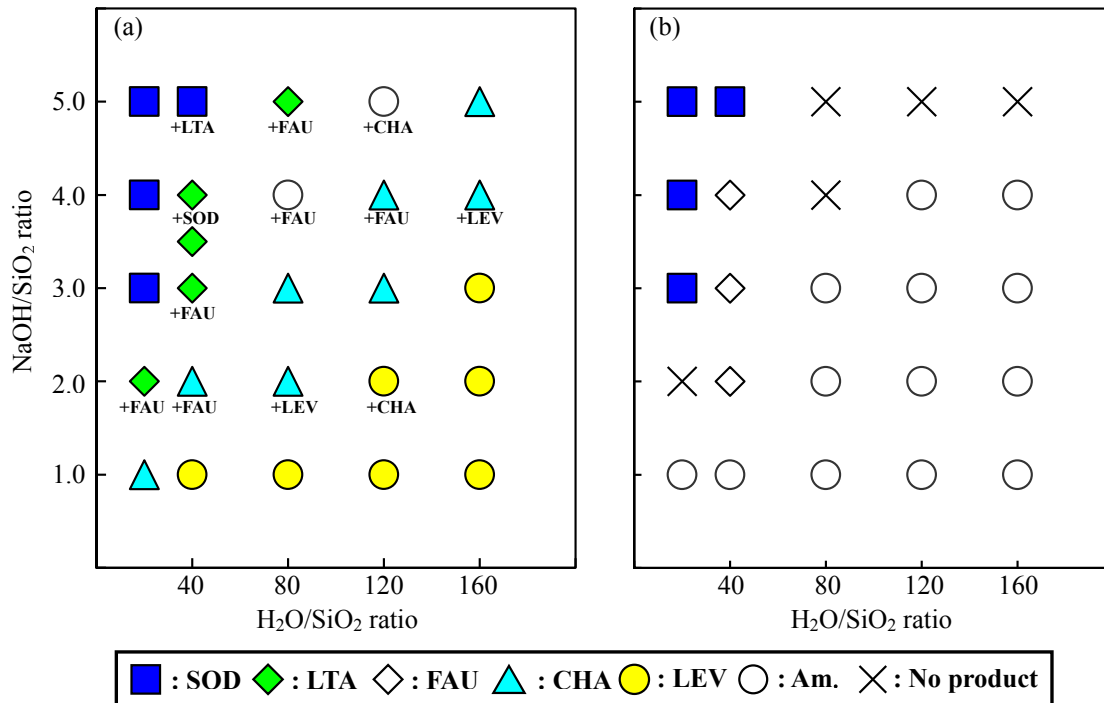


Fig. 6-5 Reactant composition diagram for zeolite syntheses at 125 °C for 1.5 h from (a) LEV (Si/Al = 9) and (b) Cab-O-Sil M-5/NaAlO₂.

When LEV zeolite was employed as the starting material, four types of zeolites, CHA, FAU, LTA, and SOD, were obtained. The less dense CHA and LTA zeolites were obtained as pure phases. The FD of LTA zeolite is $14.2 \text{ T}/1000 \text{ \AA}^3$. On the other hand only FAU and SOD zeolites were obtained from amorphous materials. The fact that CHA and LTA zeolites were not obtained from the amorphous materials under the present conditions strongly suggests that locally ordered aluminosilicate species (nanoparts) generated by the decomposition/dissolution of the starting LEV zeolite contribute to crystallization of these zeolites. LEV and CHA zeolites have similar composite building units because these two zeolites both belong to chabazite group, whereas there was less similarity between the composite units of LEV and LTA zeolites. These results strongly suggest that there is a large difference between the LEV-CHA and LEV-LTA interzeolite conversion behaviors. In contrast to the LEV-CHA transformation, the LEV-LTA transformation proceeded through the complete dissolution of the starting LEV type zeolite. In other words, there was no product at crystallization times of 0.5–1 h, and the pure LTA zeolite was only obtained after 1.5 h of synthesis time. As can be seen in Figure 6-2 (d), the LTA zeolite morphology was cubic, and the crystal size was 2–5 μm . These results strongly suggest that there is a large difference in the structures of nanoparts generated by decomposition of the starting zeolites in the LEV-CHA and LEV-LTA interzeolite conversions.

Recently, Okubo et al. investigated the crystallization mechanism of low-silica faujasite X (LSX) by using a novel method with intermediate addition of alkaline metals and the ion-exchange technique [29,30]. The ratio of potassium ions in the alkaline ions critically limited the selective formation of LSX zeolite. When potassium ions were added, the precursor to zeolite A, which is a four-membered ring (4R) in the liquid

phase, was selectively captured. This allowed the assembly of 4Rs into a double six-membered ring (D6R), which selectively formed LSX in a precipitated hydrogen phase.

On the basis of the above result, as well as the data obtained by Okubo et al., I can now speculate on the process of conversion of LEV zeolite into CHA and LTA zeolites, as follows. At high alkalinity, $\text{NaOH}/\text{H}_2\text{O} = (\text{NaOH}/\text{SiO}_2 = 3.5)/(\text{H}_2\text{O}/\text{SiO}_2 = 40) = 0.088$, it is expected that the starting LEV zeolite is decomposed into aluminosilicate species whose structure are different from the building units required for the crystallization of CHA zeolite. A simple 4R aluminosilicate is probably formed, resulting in the formation of LTA zeolite. Taking into account the fact that LTA zeolite could not form from the amorphous materials of Cab-o-sil M-5 and NaAlO_2 , it is found that the use of LEV zeolite could effectively yield the 4R aluminosilicate species. On the other hand, at lower alkalinity, $\text{NaOH}/\text{H}_2\text{O} = (\text{NaOH}/\text{SiO}_2 = 3)/(\text{H}_2\text{O}/\text{SiO}_2 = 80) = 0.038$, locally ordered aluminosilicate species whose structures are similar to those of the precursor to CHA zeolite are formed, resulting in the selective formation of CHA zeolite.

4. Conclusions

Hydrothermal conversion of LEV zeolite into CHA zeolite occurred in the absence of either OSDAs and seed crystals. Because the LEV-CHA transformation proceeds from a more dense zeolite (LEV) to a less dense one (CHA), the transformation is not thermodynamically favorable. When LEV-zeolite was used as the starting material, locally ordered aluminosilicate species (nanoparts) produced by dissolution/decomposition of the starting LEV zeolite under mild conditions contributed

to the transformation process. At higher alkalinity than that used for the CHA zeolite synthesis, LEV-LTA transformation also occurred effectively and selectively. Simple 4R aluminosilicate species were probably formed by the severe decomposition of LEV zeolite, resulting in the formation of LTA zeolite. The findings of the present study indicate the possibility of transformation of dense zeolite into less dense zeolite under mild conditions if there is similarity between the composite building units of the two zeolites. Therefore, the interzeolite conversion route has been again confirmed to be an alternative strategy for zeolite synthesis

References

- [1] J. Song, L. Dai, Y. Ji, F.-S. Xiao, *Chem. Mater.* 18 (2006) 2775.
- [2] Z. Wu, J. Song, L. Ren, Y. Ji, J. Li, F.-S. Xiao, *Chem. Mater.* 20 (2008) 357.
- [3] B. Xie, J. Song, L. Ren, Y. Ji, J. Li, F.-S. Xiao, *Chem. Mater.* 20 (2008) 4533.
- [4] G. Majano, L. Delmotte, V. Valtchev, S. Mintova, *Chem. Mater.* 21 (2009) 4184.
- [5] Y. Kamiyama, W. Chaikitlisilp, K. Itabashi, A. Shimojima, T. Okubo, *Chem. Asian J.* 5 (2010) 2182.
- [6] T. Yokoi, M. Yoshioka, H. Imai, T. Tatsumi, *Angew. Chem. Int. Ed.* 48 (2009) 9884.
- [7] K. Iyoki, Y. Kamimura, K. Itabashi, A. Shimojima, T. Okubo, *Chem. Lett.* 39 (2010) 730.
- [8] E.-P. Ng, D. Chateigner, T. Bein, V. Valtchev, S. Mintova, *Science*, 335 (2012) 70.
- [9] N.J. Henson, A.K. Cheetham, J.D. Gale, *Chem. Mater.* 6 (1994) 1647.
- [10] P.M. Piccione, C. Laberty, S. Yang, M.A. Camblor, A. Navrotsky, M.E. Davis, *J. Phys. Chem. B* 104 (2000) 10001.
- [11] B. Subotić, D. Škrtić, I. Šmit, L. Sekovanić, *J. Cryst. Growth* 50 (1980) 498.
- [12] S.I. Zones, *J. Chem. Soc. Faraday Trans.* 87 (1991) 3709.
- [13] Y. Kubota, H. Maekawa, S. Miyata, T. Tatsumi, Y. Sugi, *Micropor. Mesopor. Mater.* 101 (2007) 115.
- [14] H. Jon, K. Nakahata, B. Lu, Y. Oumi, T. Sano, *Micropor. Mesopor. Mater.* 96 (2006) 72.
- [15] H. Jon, S. Takahashi, H. Sasaki, Y. Oumi, T. Sano, *Micropor. Mesopor. Mater.* 113 (2008) 56.
- [16] M. Itakura, T. Inoue, A. Takahashi, T. Fujitani, Y. Oumi, T. Sano, *Chem. Lett.* 37 (2008) 908.

- [17] T. Inoue, M. Itakura, H. Jon, Y. Oumi, A. Takahashi, T. Fujitani, T. Sano, *Micropor. Mesopor. Mater.* 122 (2009) 149.
- [18] H. Sasaki, H. Jon, M. Itakura, T. Inoue, T. Ikeda, Y. Oumi, T. Sano, *J. Porous Mater.* 16 (2009) 465.
- [19] M. Itakura, Y. Oumi, M. Sadakane, T. Sano, *Mater. Res. Bull.* 45 (2010) 646.
- [20] H. Jon, N. Ikawa, Y. Oumi, T. Sano, *Chem. Mater.* 20 (2008) 4135.
- [21] K. Honda, A. Yashiki, M. Itakura, Y. Ide, M. Sadakane, T. Sano, *Micropor. Mesopor. Mater.* 142 (2011) 161.
- [22] A. Yashiki, K. Honda, A. Fujimoto, S. Shibata, Y. Ide, M. Sadakane, T. Sano, *J. Cryst. Growth* 325 (2011) 96.
- [23] R.M. Barrer, L. Hinds, E.A. White, *J. Chem. Soc.* (1953) 1466.
- [24] C.M. Zicovich-Wilson, F. Gándara, A. Monge, M.A. Camblor, *J. Am. Chem. Soc.* 132 (2010) 3461.
- [25] P. Tian, X. Su, Y. Wang, Q. Xia, Y. Zhang, D. Fan, S. Meng, Z. Liu, *Chem. Mater.* 23 (2011) 1406.
- [26] D.E. Akporiaye, I.M. Dahl, H.B. Mostad, R. Wendelbo, *J. Phys. Chem.* 100 (1996) 4148
- [27] H. Robson, K.P. Lillerud, *Verified Syntheses of Zeolitic Materials*, second ed., Elsevier, Amsterdam, (2001) p. 123.
- [28] Z. Gabelica, N. Blom, E.G. Derouane, *Appl. Catal.* 5 (1983) 227.
- [29] M. Iwama, Y. Suzuki, J. Plévert, K. Itabashi, M. Ogura, T. Okubo, *Cryst. Growth Des.* 10 (2010) 3471.
- [30] M. Ogura, Y. Kawazu, H. Takahashi, T. Okubo, *Chem. Mater.* 15 (2003) 2661.

Chapter 7

Synthesis and crystal structure of a layered silicate HUS-1 with a halved sodalite-cage topology

1. Introduction

Layered silicates are among important industrial materials, and their use as a flexible silica material has attracted the interest of many researchers. So far, layered silicates have been used as a silica source for the synthesis of various mesoporous materials or other silicates. For example, mesoporous FSM-16 and KSW-2 were synthesized from clay-like layered silicate kanemite and magadiite, respectively [1,2], and a zeolite offretite and a layered silicate FLS-1 were synthesized from magadiite [3,4]. Moreover, layered silicates have been adopted for new zeolite syntheses, as nanosized blocks in the topotactic conversion method. For example, CDO (the three characters indicate the framework code) [5], NSI [6], CAS-NSI [7], RWR [8-10], and RRO [11] zeolites have been prepared using layered silicates PLS-15 (isomorphic materials: PLS-4 [12], RUB-36 [13,14], MCM-47 [15], MCM-65 [16], UZM-13 [17], UZM-17 [17], UZM-19 [17]), Nu-6(1) [6], EU-19 [7,18], RUB-18 [19], and RUB-39 [20], respectively. In this method, frameworks of layered silicates are used like a Lego block, without destruction of their framework structures.

It is also known that layered silicates β -HLS [21] and RUB-15 [22] (isomorphic material: DLM-2 [23]) have a zeolitic framework composed of a halved sodalite cage. In both compounds, tetramethylammonium (TMA) cations are located in the interlayer.

Sodalite (SOD zeolite) [24], one of the most traditional zeolites, is constructed by connecting sodalite cages. The sodalite cage is a truncated octahedral cage composed of four- and six-membered Si rings; the effective window diameter is therefore small, about 0.22 nm, at the six-membered ring.

The framework structures of both β -HLS and RUB-15 are in part identical to that of sodalite, and the structural difference between them is the cutting direction in the sodalite structure (Figure 7-1). The β -HLS framework can be formed by clipping the sodalite cage along the [100] direction, whereas the framework of RUB-15 is formed by clipping along the [110] direction. Li and co-workers[25] reported a new layered silicate RUB-51 which includes the bulky benzyltrimethylammonium hydroxide in the interlayer. The RUB-51 framework structure is the same as that of RUB-15. Moteki et al.[26] reported that high-silica sodalite, whose pore openings are not occluded, can be obtained from RUB-15 by topotactic conversion via lamellar intermediates prepared by treatment with acetic acid. They also first demonstrated that the resultant high-silica sodalite has high hydrogenadsorption capabilities.

In this work, I found a new type of a layered silicate, HUS-1 (Hiroshima University Silicate-1), with a halved SOD framework structure; the silicate was obtained based on the interzeolite conversion method. Recently, I have demonstrated that various zeolites can be prepared by this method using a decomposed zeolite FAU as nanosized silica parts. The key concept of the interzeolite conversion method, which is a bottom-up building process, has been described elsewhere [27]. To date, CHA, *BEA, RUT, LEV, MTN, and OFF aluminosilicate zeolites have been synthesized by this method with tetraalkylammonium cations as a OSDA molecule [28-33].

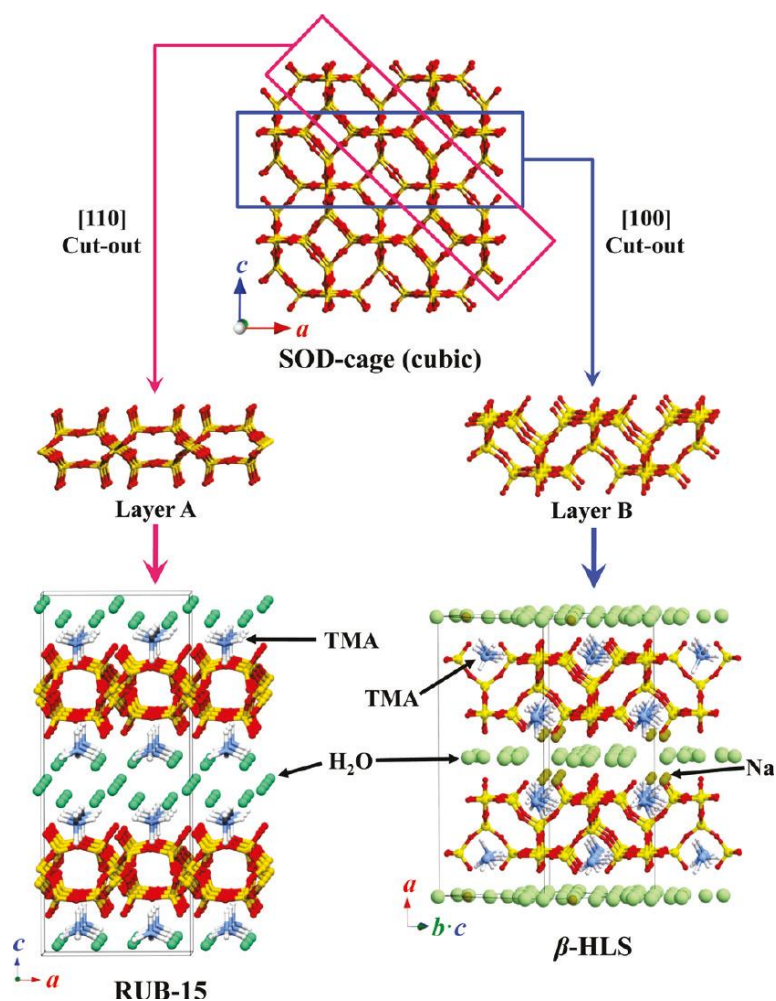


Fig. 7-1 Structural relationship between the layered silicates, RUB-15 and β -HLS. Both framework topologies are similar to that of SOD-type zeolite.

The layered silicate HUS-1 was synthesized hydrothermally using two kinds of zeolites, that is, FAU and *BEA. The crystal structure and physicochemical properties of HUS-1 were investigated in detail by X-ray powder diffractometry (XRD), solid-state magic-angle-spinning nuclear magnetic resonance (MAS NMR) spectroscopy, and thermogravimetric-differential thermal analysis (TG-DTA).

2. Experimental

2.1 Synthesis of HUS-1

The starting FAU and *BEA zeolites were prepared from $\text{NH}_4\text{-Y}$ zeolite (Si/Al = 2.8, Tosoh Co., Japan) and H-*BEA (Si/Al = 21, Tosoh Co., Japan) by dealumination with H_2SO_4 (0.44 M) at 75 °C for 4 h. The interzeolite conversion was performed as follows. Two types of primary gels including silica nanosized parts were prepared. One was prepared by decomposition of dealuminated FAU zeolite by hydrothermal treatment with tetramethylammonium hydroxide (TMAOH, 20 wt %, Aldrich, U.S.A.) at 125 °C for 24 h. The gel composition was Si/Al = 22, $\text{H}_2\text{O}/\text{SiO}_2 = 5.5$, and $\text{TMAOH}/\text{SiO}_2 = 0.2$.

The other primary gel was prepared by decomposition of dealuminated *BEA zeolite by hydrothermal treatment with benzyltrimethylammonium hydroxide (BTMAOH, 40 wt %, Aldrich, U.S.A.) at 125 °C for 24 h. The gel composition was Si/Al = 78, $\text{H}_2\text{O}/\text{SiO}_2 = 5.5$, and $\text{BTMAOH}/\text{SiO}_2 = 0.8$.

The resultant primary gels were mixed well with an aqueous solution of NaOH, and then the mixture was placed in a Teflon-lined stainless steel autoclave with a volume of 30 cm^3 . The composition of the gel mixture was Si/Al = 50, $\text{TMAOH}/\text{SiO}_2 = 0.1$, $\text{BTMAOH}/\text{SiO}_2 = 0.4$, $\text{NaOH}/\text{SiO}_2 = 0.2$, and $\text{H}_2\text{O}/\text{SiO}_2 = 5.5$. The hydrothermal conversion was conducted at 398 K for 7-21 d in a convection oven. The solid product was collected by centrifugation and washed thoroughly with deionized water until filtrates became nearly neutral and then dried overnight at 70 °C.

2.2 Physicochemical analysis

For accurate structural analyses, XRD data were collected at room temperature on an ADVANCE D8-VRrio1 (Bruker AXS, Japan) powder diffractometer with a modified Debye-Scherrer geometry and Cu KR1 radiation from a Ge(111) primary monochromator. The diffractometer was equipped with a linear position-sensitive detector VANTEC-1 (2θ coverage of 8°) and operated at 40 kV and 50 mA. The samples were sealed in borosilicate capillary tubes with an inner diameter of 0.7 mm. The μr (μ : linear absorption coefficient, r : sample radius) values of these sample tubes, which were determined by transmittance measurements, were 0.33, which was used for X-ray absorption corrections.

Crystal morphology was observed using an S-4800 (Hitachi, Japan) field emission scanning electron microscope (FE-SEM) operated at an acceleration voltage of 1 kV. Before the observation, all the samples were coated with an ion liquid (IL) of 1-butyl-3-methylimidazolium tetrafluoroborate (BMI-BF, Tokyo Chemical Industry Co., Inc.). The dilution of IL to a concentration of about 10% by methanol was effective for coating thin layers of IL on the sample. Coating of insulating samples (such as anhydrous silicate) with IL is effective in providing electronic conductivity to the samples, like metal coating by vacuum vapor deposition, that is, the electrification of the samples can be reduced remarkably[34]. Thermogravimetric analysis was carried out on a TG-DTA 2100 (MAC Science, Co. Ltd., Japan) in dry air at a heating rate of 10 °C/min. The amount of intercalated molecules was estimated from the resulting TG-DTA curves. The chemical composition was roughly estimated by energy-dispersive X-ray (EDX) spectroscopy with EMAX EX-350 (HORIBA, Japan) attached to the above FE-SEM. Especially, carbon, hydrogen, and nitrogen contents of HUS-1 were

determined by using a Yanaco CHN corder MT-6 in detail.

Solid-state ^1H - ^{29}Si dipolar-decoupled (DD) MAS NMR spectra were measured with a spinning frequency of 5 kHz using a 4 mm MAS probe, a 90° pulse length of 3.6 μs , and a cycle delay time of 100 s on an AVANCE 400 WB spectrometer (Bruker BioSpin, Japan) operated at 79.495 MHz. Solid-state ^1H - ^{29}Si cross-polarization (CP) MAS NMR spectra were also measured, with a contact time of 4 ms. The ^{29}Si chemical shift was calibrated with a standard sample of tetramethylsilane (TMS). The ^1H and ^{27}Al MAS NMR spectra were measured with a spinning frequency of 12 kHz and a single pulse sequence operated at 104.26 MHz for ^{27}Al and 400.13 MHz for ^1H . Furthermore, the ^1H - ^{13}C CP MAS NMR spectra were also measured with a spinning frequency of 5 kHz, a 90° pulse length of 4.7 μs , and a cycle delay time of 5 s (operated at 100.613 MHz). The ^1H , ^{13}C , and ^{27}Al chemical shifts were referenced to TMS, glycine, and an aqueous solution of AlCl_3 (1 mol/dm³), respectively.

2.3 Structural analysis

The crystal structure of HUS-1 was determined by ab initio structural analysis. Indexing of reflections with the programs DICVOL91 [35] and N-TREOR built in the program EXPO2009 [36] successfully gave lattice parameters and indices of the reflections. The space group was determined from reflection conditions derived from these indices. Observed integrated intensities, $|F_{\text{obs}}|^2$, were extracted by the Le Bail method [37] using EXPO2009.

Then, a structural model for HUS-1 was constructed by combination of the powder charge-flipping (*p*CF) method using Superflip [38,39] and the direct method with EXPO2009.

Lattice and structure parameters of HUS-1 were refined by the Rietveld method using the program RIETAN-FP [40] on the basis of the above structural model. A split pseudo-Voigt profile function and a background function of Legendre polynomials with 11th order were used in the refinement. Partial profile relaxation [41] with a modified split pseudo-Voigt function was applied to some reflections with highly asymmetric profiles. In the early stage of the refinement, I imposed restraints upon all the Si-O bond lengths, that is, $l(\text{Si-O}) = 1.60 (0.02 \text{ \AA})$, all the O-Si-O bond angles, that is, $\varphi(\text{O-Si-O}) = 109.47 (2.0^\circ)$. Furthermore, restraints were imposed upon all the N-C bond lengths, that is, $l(\text{N-C}) = 1.49 (0.03 \text{ \AA})$, all the C-H bond lengths, that is, $l(\text{C-H}) = 1.08 (0.02 \text{ \AA})$, all the C-N-C, N-C-H, and H-C-H bond angles, that is, $\varphi(\text{C-N-C}) = \varphi(\text{N-C-H}) = \varphi(\text{H-C-H}) = 109.47 (3.0^\circ)$, which are based on the molecular geometry of TMA, in the final stage of the structure refinement. Degrees of restraints were gradually decreased with progress in the structure refinement.

Electron-density distribution (EDD) in the unit cell of HUS-1 was calculated from the observed structure factors, F_{obs} , by the maximum entropy method (MEM) using the program *Dynomia* [42]. After the first MEM analysis, EDD was redetermined by MEM-based pattern fitting (MPF) [40]. The MPF analysis, which is an alternate repetition of whole-pattern fitting and MEM analyses, is very effective in visualizing chemical bonds and disordered arrangements of chemical species such as interlayer organic molecules. Table 7-1 summarizes experimental conditions of the XRD measurement and parts of the results of the Rietveld refinement for HUS-1. The final structural model and electron density distribution were visualized using the program *VESTA* [43].

Table 7-1 Conditions of the XRD Experiment and Parts of Data Related to the Rietveld Refinement for Layered Silicate HUS-1

compound name	HUS-1
estimated chemical formula	$\text{Si}_{10}\text{O}_{24}\text{H}_6 \cdot 2[(\text{CH}_3)_4\text{N}]$
F_w	819.18
space group	$P2_1$ (No. 4)
$a/\text{\AA}$	8.95561(19)
$b/\text{\AA}$	9.21294(13)
$c/\text{\AA}$	8.74207(12)
β/deg	95.831(2)
unit-cell volume, $V/\text{\AA}^3$	717.55(13)
wavelength, $\lambda/\text{\AA}$	1.540593 (Cu $K\alpha_1$)
2θ range/deg	8.0–100.1
step size, $2\theta/\text{deg}$	0.017368
counting time per step/s	32624
profile range in the unit of fwhm	14
fwhm/deg (at $2\theta = 16.566^\circ$)	0.246
no. of intensity data	5304
no. of contributing reflections	799
no. of refined structural parameters	115
no. of background parameters	12
no. of nonlinear restraints	102
R_F (Rietveld)	0.0080
R_B (Rietveld)	0.0079
R_{wp} (Rietveld)	0.0231
R_e (Rietveld)	0.0145
R_F (MEM_final)	0.0076
R_{wp} (MEM_final)	0.0051

3. Results and discussion

3.1 XRPD, SEM, and TG-DTA analysis

Figure 7-2 shows XRD patterns of the samples of HUS-1. Crystal growth of HUS-1 was finished almost completely after a reaction time of 7 d. Although the crystallinity of the resultant HUS-1 after reaction for 7 d was moderate, it was somewhat improved by extending the reaction time to 21 d. I will hereinafter describe only the product resulting from the reaction for 21 d.

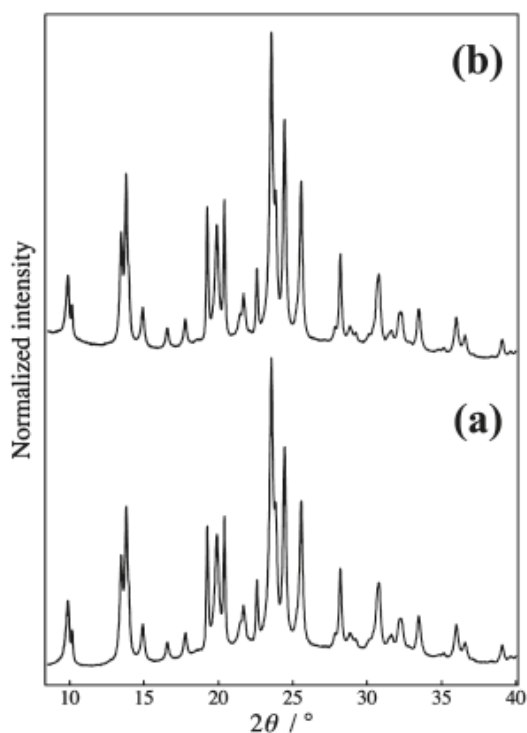


Fig. 7-2 XRD patterns of HUS-1 synthesized with reaction times of (a) 7 d and (b) 21 d using CuKR1 radiation.

A SEM image in Figure 7-3 shows that the product shape has the form of square plates with a size up to an area of $2\ \mu\text{m}$ – $4\ \mu\text{m}$ and a thickness up to $0.8\ \mu\text{m}$. The plate crystals were found to be stacks of thin layers, and their surfaces were rough with large voids. These findings suggest that HUS-1 has a typical layered structure. From EDX analysis,

Al and Na were hardly detected in the product. Carbon, hydrogen, and nitrogen contents of HUS-1 were estimated at 11.28 wt %, 3.37 wt %, and 3.37 wt %, respectively, indicating total amount of organic content of 18.02 wt %. This means that atomic ratio of the organic species in the product is C/H/N = 3.9:13.8:1.0.

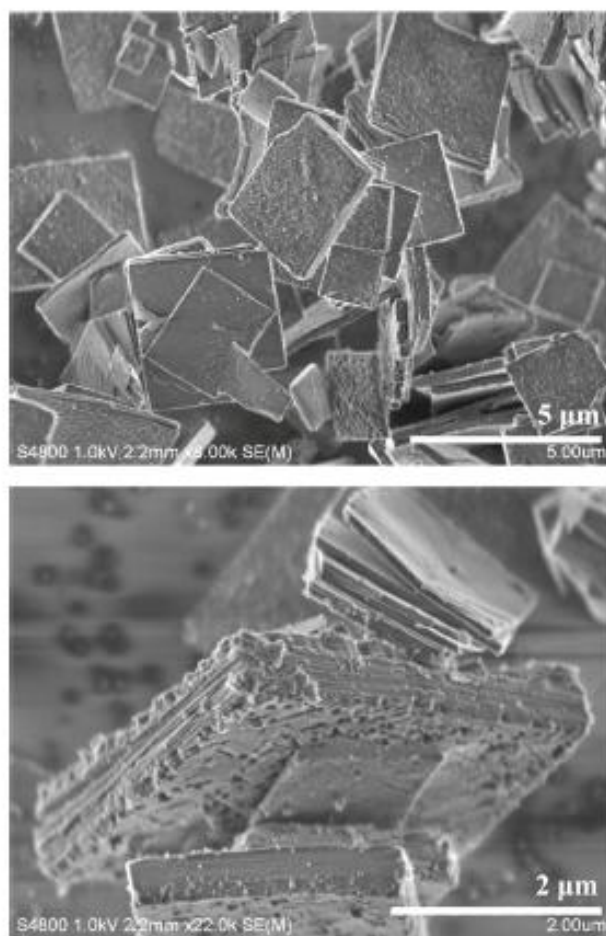


Fig. 7-3 SEM micrographs of HUS-1. The upper and lower images showsquare-shaped plate morphology and the rough surfaces,

A large weight loss of about 23 wt %, which is larger than that of organic content estimated by CHN analysis, was observed in TG-DTA curves in a temperature range 573-630 K (Figure 7-4).A strong exothermic peak was also observed at 350 °C. This

result suggests that observed large weight loss is derived from combustion of intercalated organic species and dehydration condensation of layered framework (see section 3.3). The weight loss at temperatures lower than 200 °C was only about 1 wt %, which provides evidence for a small amount of adsorbed water molecules in the interlayers; that is, HUS-1 is regarded as an anhydrous layered silicate. Additionally, the gradual weight loss of about 3 wt % was observed at > 357 K, which is due to dehydration condensation of silanols in the framework.

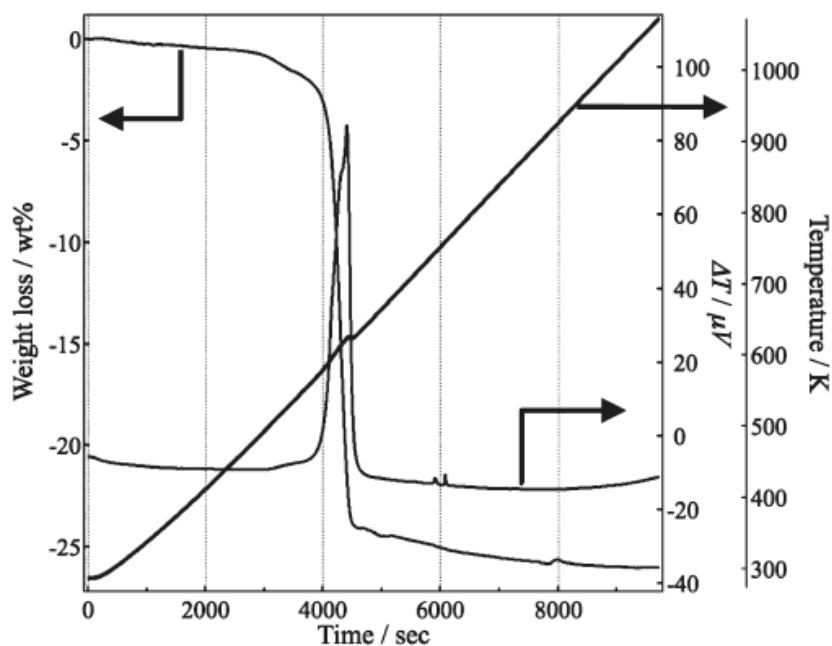


Fig. 7-4 TG, DTA, and temperature curves in the thermal analysis of HUS-1.

3.2 Solid-state NMR

First, NMR spectroscopy probes all samples in the specimen container including the amorphous part. Accordingly, the signal of the amorphous fraction overlaps the signal of the crystalline sample more or less. Figure 5 gives a ^1H - ^{13}C CP MAS NMR spectrum of HUS-1. A sharp resonance peak observed at 57.4 ppm is attributed to a methyl group, which presents evidence that only TMA cations are intercalated. This result, that is, the presence of TMA molecule with a molecular formula of $\text{C}_4\text{H}_{12}\text{N}$, was well consistent with the atomic ratio of $\text{C}:\text{H}:\text{N} = 3.9:13.8:1.0$ determined by the CHN analysis. BTMA cations are believed to be either absent in HUS-1 or decomposed into TMA cations during the hydrothermal conversion. BTMA is, in general, not converted into TMA. However, a puzzling phenomenon was observed in the synthesis of zeolite MTN by interzeolite conversion[32]. Moreover, a ^{13}C NMR spectrum of the primary gel including zeolite *BEA and BTMA cations showed the inclusion of BTMA cations.

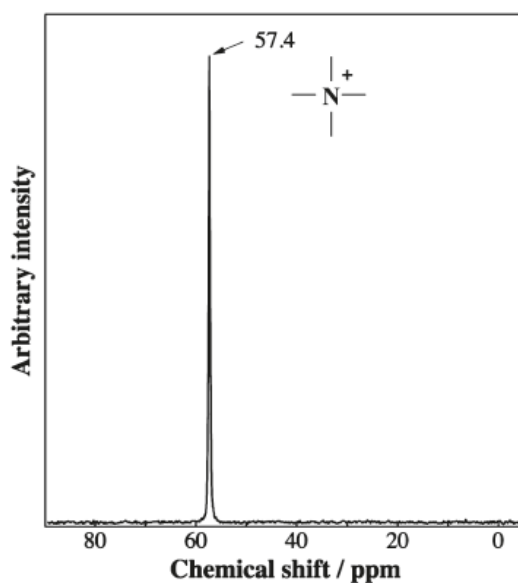


Fig. 7-5 ^1H - ^{13}C CP MAS NMR spectrum of HUS-1.

The presence of a tetrahedral Al site was detected in a ^{27}Al MAS NMR spectrum (Figure 7-6). However, the intensity of the peak was very small with a low S/N ratio despite accumulation of 5120 scans for this spectrum. The amount of Al atoms in the HUS-1 framework is, therefore, negligible. Further, a peak due to an octahedral Al site was hardly detected near 0 ppm. These findings are nearly consistent with the result of EDX analysis. Thus, in the structure refinement, I regarded that HUS-1 contains no Al atoms.

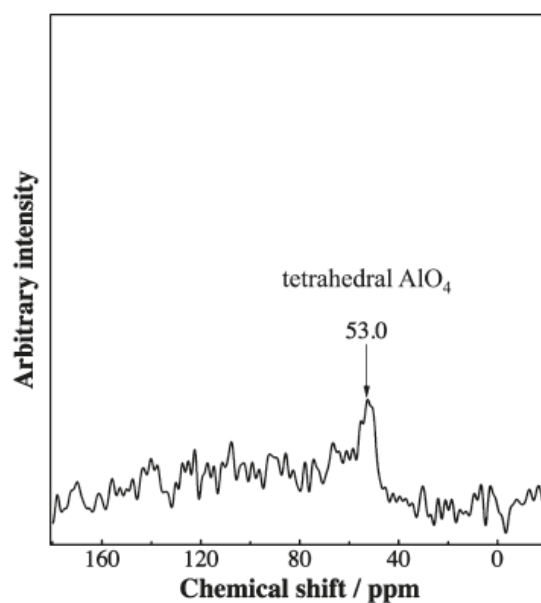


Fig. 7-6 ^{27}Al MAS NMR spectrum of HUS-1.

Figure 7-7 shows a ^1H MAS NMR spectrum of HUS-1. A resonance peak attributed to a methyl group was observed at 3.3 ppm. Three broad resonance peaks at 5.9 ppm, 9.9 ppm, and 12.5 ppm are due to the $\text{SiO-H}\cdots\text{OSi}$ hydrogen bonding of silanol groups. The atomic distances, $d(\text{O-O})$, between adjacent silanols were estimated at 2.78 Å, 2.64 Å, and 2.56 Å from the downfield shift, which is described as $\delta / \text{ppm} = 90.3 - 30.4 \times d(\text{O-H}\cdots\text{O}) / \text{Å}$ [44]. This finding suggests that the hydrogen bonding is

formed in the interlayer or intralayer.

An ^{29}Si MAS NMR spectrum showed inclusion of a large amount of Q^3 $[(-\text{SiO})_3\text{Si-OH}]$ structures in the HUS-1 framework. Three Q^3 resonance peaks were observed at -102.7 ppm, -105.6 ppm, and -107.5 ppm although a single Q^4 $[(-\text{SiO})_4\text{Si}]$ resonance peak was observed at -114.6 ppm in a ^1H - ^{29}Si DD MAS NMR spectrum (Figure 8a). The peak intensity ratio of Q^3/Q^4 was estimated at about 4.4 by curve fitting with a Lorentz function. The ^1H - ^{29}Si CP MAS NMR spectrum of HUS-1 was similar to the DD MAS NMR spectrum (Figure 7-8b) though intensities of Q^3 -peaks increased with sharper peak widths. These findings support the idea that HUS-1 has a layered structure with a large number of silanols on the layer surface.

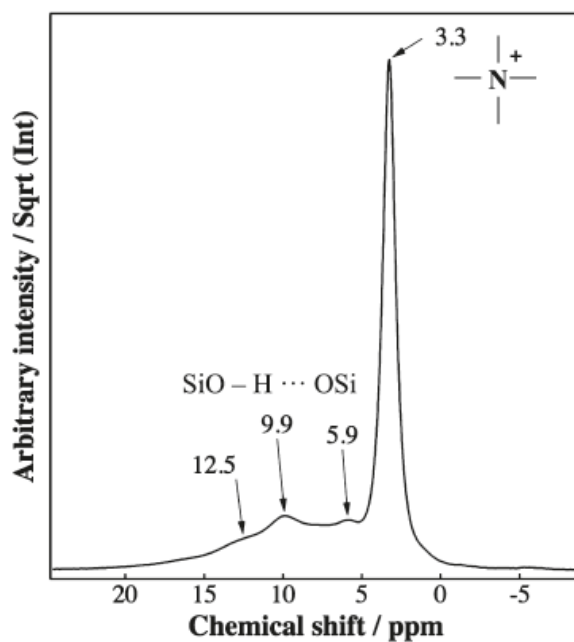


Fig. 7-7 ^1H MAS NMR spectrum of HUS-1; the y axis is displayed in a square-root scale.

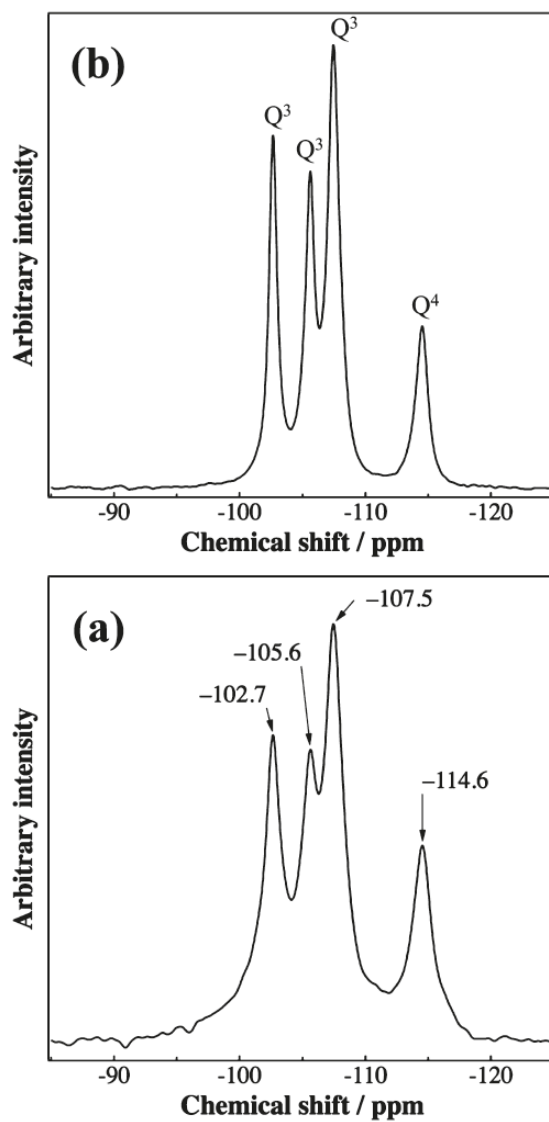


Fig. 7-8 (a) ^1H - ^{29}Si DD MAS NMR and (b) ^1H - ^{29}Si CP MAS NMR spectra of HUS-1.

3.3 Structural analysis

The indexing of the reflections gave a monoclinic unit cell of $a = 0.8973$ nm, $b = 0.9214$ nm, and $c = 0.8748$ nm, $\beta = 95.83^\circ$ with acceptable figures of merit: $F17 = 32$ and $M17 = 55$. Reflection conditions derived from the indexed reflections were $k = 2n$ for $0k0$, which gives two possible space groups: $P2_1$ and $P2_1/m$. Assuming that HUS-1 is centrosymmetric, we tentatively adopted $P2_1/m$ (No. 11, setting 1).

$|F_{\text{obs}}|^2$ values of 798 reflections in the region $d > 0.1$ nm were extracted by the Le Bail method. I, at first, attempted to solve the framework structure of HUS-1 by the direct method, but no solution was obtained. Next, I applied the pCF method to obtain the framework structure and detected four Si and five O sites. The framework topology composed of four- and sixmembered rings were clarified at this stage. Observed values of $|F_{\text{obs}}|^2$ were then re-extracted by the Le Bail method using RIETAN-FP on the basis of the partial structural information and analyzed by the direct-method with EXPO2009. Consequently, three additional O sites attributed to terminal silanols were successfully located. As figure 7-9 illustrates, its topology is identical to that of a halved SOD framework. A few atoms attributed to a TMA cation were further found in a hemispherical space.

All the sites, that is, four Si and eight O sites in the asymmetric unit, derived in the above way were included as the initial structural model of the Rietveld refinement. The fractional coordinates of a virtual atom corresponding to a TMA cation, which has a scattering amplitude equivalent to $(\text{CH}_3)_4\text{N}$, in a hemispherical space were also refined because the atomic configuration of the TMA cation could not be determined unambiguously.

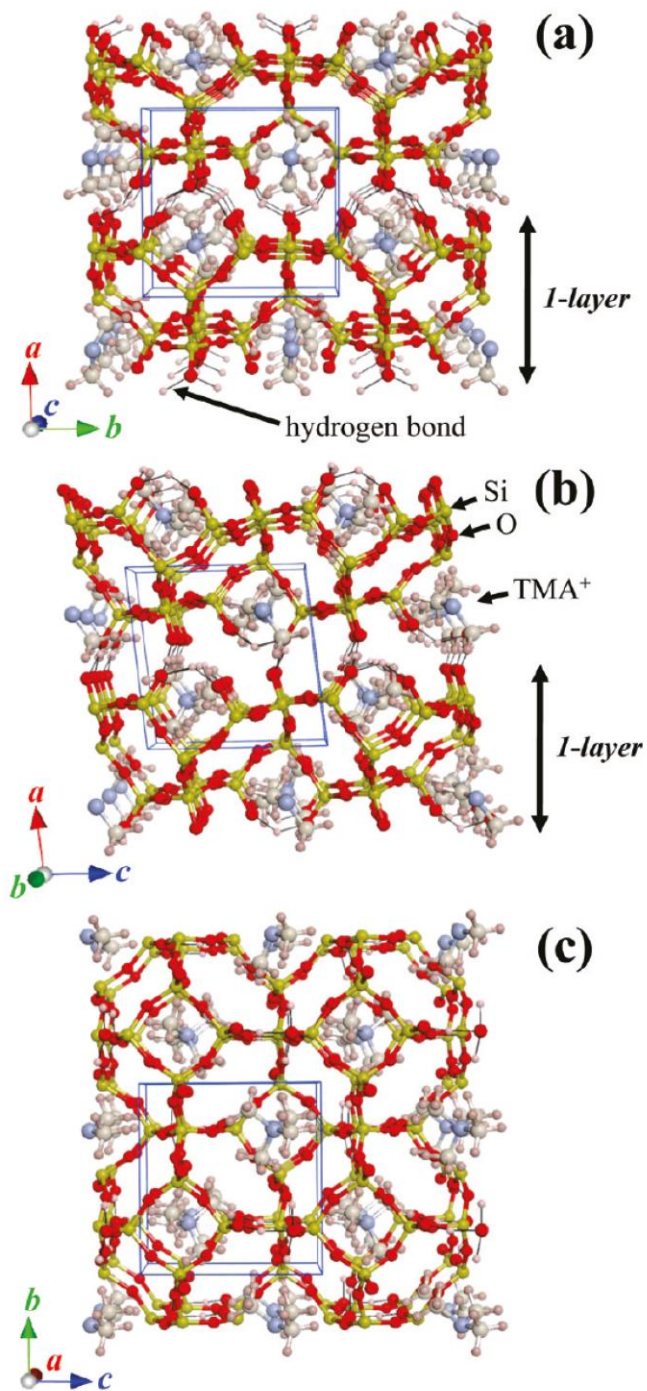


Fig. 7-9 Structural model of HUS-1 viewed along the (a) [001], (b) [010], and (c) [100] directions.

This finding, coupled with the results of the TG-TDA and ^{13}C MAS NMR measurements, shows the presence of TMA molecules in the interlayer. At this stage, the reliability indices, R_{wp} and R_{B} , reached 3.5% ($S = 2.4$) and 2.0%, respectively.

The distribution of TMA cations in the hemispherical cage was investigated by the direct-space method with the program FOX[45]. In this analysis, the molecular structure of the TMA cation plus an H atom were introduced into a structural model as a single atomic group with bond lengths and angles restrained within very narrow regions. In addition, the positions of all the framework atoms were fixed at the positions determined by the Rietveld analysis. As a result, two equivalent TMA molecules overlapped along the b axis appeared in the hemispherical cage, and the positions of the H atoms of the molecule were too close to the framework atoms, which suggests that the space-group symmetry, $P2_1/m$, assumed thus far is quite inadequate. I, therefore, reconstructed the previous model according to the space-group symmetry of $P2_1$ (No. 4), which is a maximal nonisomorphic subgroup of $P2_1/m$ [46]. The transformation from the centrosymmetric space group $P2_1/m$ to the noncentrosymmetric $P2_1$ enables a pair of positions, (x, y, z) and $(-x, -y, -z)$, to become independent. Among the four known Si atoms, three of them, which are in special positions in the space group $P2_1/m$, are still kept, and one Si atom is split into two sites. Among the oxygen atoms, four sites in the $P2_1/m$ model were split, resulting in eight sites, and the other oxygen sites are not doubled. The TMA molecule was located near the center of the hemispherical cage with its molecular orientation determined clearly. Each atomic position of TMA obtained in this way was used for the model reconstruction.

The EDD obtained by MPF strongly suggests the presence of hydrogen bonds between terminal oxygen sites O1-O3, O1-O4, and O1-O7. Three proton sites at (0.47, 0.88,

0.17) for site H18, (0.49, 0.61, 0.20) for site H19, and (0.55, 0.25, 0.67) for site H20 were then added to the structural model because these positions corresponded to weighted centers of the hydrogen bonds in the EDD images. The scattering amplitude of H was added to site O7 in a terminal silanol group to maintain the charge balance.

In the final Rietveld refinement, 5 Si, 12 O, 1 N, 4 C, and 15 H sites were included in the asymmetric unit. All the isotropic atomic displacement parameters, B , for the Si sites were constrained to be equal: $B(\text{Si}1) = B(\text{Si}n; n = 2-4)$. Simple approximations of $B(\text{O}1) = B(\text{O}n; n = 2-12)$ and $B(\text{C}n; n = 1-4) = B(\text{N}5) = B(\text{H}n; n = 6-17)$ were also imposed on the B parameters of the O sites and of the C, N, and H sites, respectively. The B values of the H18, H19, and H20 sites were fixed at 5.0 \AA^2 for convenience.

Finally, R factors were decreased to sufficiently low levels, that is, $R_{\text{wp}} = 2.3\%$ ($S = 1.6$) and $R_{\text{B}} = 0.8\%$ (Table 7-1).

The chemical formula of HUS-1 was estimated to be $\text{Si}_{10}\text{O}_{24}\text{H}_6 \cdot 2[(\text{CH}_3)_4\text{N}]$ according to the results of the structure refinement. The resulting organic content, which was calculated to be 18.05 wt %, agreed with those determined by the CHN analysis (ca. 18.0 wt %) very well. If I suppose that HUS-1 changes to amorphous silica completely (i.e., $\text{Si}_{10}\text{O}_{24}\text{H}_6 \cdot 2[(\text{CH}_3)_4\text{N}] \rightarrow \text{Si}_{10}\text{O}_{20}$), the total weight loss is calculated as 26.7 wt %, which is almost in agreement with the observed weight loss of 26.0 wt % by the TG-DTA analysis. Although a small amount of silanols might remain because of incomplete condensation, the TG result strongly supports the chemical formula estimated by the structure analysis. Thus, it was found that the result of the chemical analysis coincides with the structure model of HUS-1.

Figure 7-9 shows the structural model of HUS-1 obtained finally. The narrowest width between adjacent layers was estimated at about 0.15 nm (Figure 7-11). The lattice

parameter, a , approximately corresponds to the thickness of the silicate layer. The projection of the silicate layer along the [100] direction coincides with that of the sodalite structure along the [100] direction (Figure 9c). The nearest atomic distances between neighboring silanol groups, $l(\text{O-O})$, were $l(\text{O1-O3}) = 2.64(3) \text{ \AA}$, $l(\text{O1-O4}) = 2.53(6) \text{ \AA}$, and $l(\text{O1-O7}) = 2.69(2) \text{ \AA}$, which are in good agreement with the values, that is, 2.56 \AA , 2.64 \AA , and 2.78 \AA , estimated from the ^1H MAS NMR spectrum. Additionally, calculated Q^3/Q^4 ratio on the basis of the framework geometry is 4.0, which was smaller than the value (ca. 4.4) estimated by the ^{29}Si DDMAS NMR spectrum. This fact suggests that there is a small amount of Si atom defects in framework. The position of the defective site, however, could not be determined unambiguously by the structure refinement because of moderate crystallinity of the sample. The average bond length $l(\text{Si-O})$ and bond angle $\phi(\text{O-Si-O})$, which are close to expected values, fall within $1.55\text{-}1.64 \text{ \AA}$ and $106.1\text{-}114.1^\circ$, respectively.

Figure 7-10 shows EDD images of HUS-1 obtained by the MPF analysis. Electron densities attributed to hydrogen bonding were clearly seen between sites O1 and O7 (Figure 7-10a). Similarly, electron densities are observed between sites O1 and O3 and between sites O1 and O4 (Figure 7-10b). These findings support the idea that adjacent layers are bridged by hydrogen bonding to form a pseudo-spherical cage, with an internal diameter of about 0.65 nm, in the interlayer. Because the EDD determined by MPF shows the ordered arrangement of TMA in the pseudo-cage, the TMA molecules are believed to be cations. Furthermore, molecular motion of TMA is estimated to be considerably restricted. The MPF analysis lowered $R_{\text{wp}}(\text{MEM})$ from 0.75% to 0.51% and $R_{\text{F}}(\text{MEM})$ from 0.82% to 0.77% after four cycles.

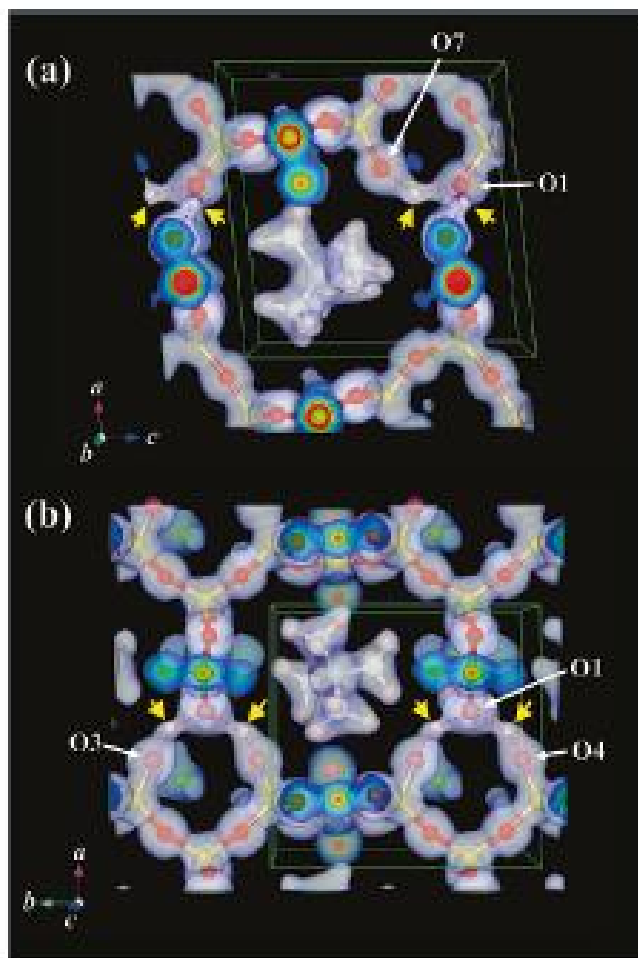


Fig. 7-10 EDD images of HUS-1 obtained by the MPF analysis: (a) electron densities ($0 < y < 0.51$) viewed along the b axis, and (b) electron densities ($0.43 < z < 1.0$) viewed along the c axis. The spatial resolution was $90 \times 92 \times 88$ pixels per unit cell.

3.4 Structural comparison of HUS-1 and β -HLS

Figure 7-11 illustrates the framework structures of HUS-1 and β -HLS[20] viewed along three different directions. The stacking sequence of neighboring layers in HUS-1 is completely different from that in β -HLS. The layers in HUS-1 are alternately stacked with shifts of $0.5b$ and $0.5c$ along the $[010]$ and $[001]$ directions, respectively, compared with those in β -HLS. In fact, the crystal structure of HUS-1 is formed in an AAAA stacking order whereas that of β -HLS is formed in an ABAB stacking order. Their

framework topologies are similar to each other. However, the framework of HUS-1 is somewhat asymmetric in comparison with the symmetric framework geometry of β -HLS or sodalite.

The interlayer distance in β -HLS is much larger than that in HUS-1. Adsorbed water molecules and Na^+ ions are densely distributed in the β -HLS[20] interlayer (Figure 7-1), but a small amount of H^+ ions contributing to hydrogen bonding is distributed in the HUS-1 interlayer. In both compounds, TMA cations are known to be accommodated in halved sodalite cages. From the structural model obtained in the present study, I can safely guess that HUS-1 is not transformed into sodalite by direct calcination. Although, HUS-1 was changed to an amorphous phase by calcination, a structural transformation may be achieved by some chemical modifications. For example, like IEZ[47-49] or APZ[50] series, which are prepared from various layered silicates, interlayer expansion may be possible even in HUS-1 by silylation or acid treatment because no extra-framework atoms exist in the interlayer except for TMA cations in the hemispherical cage.

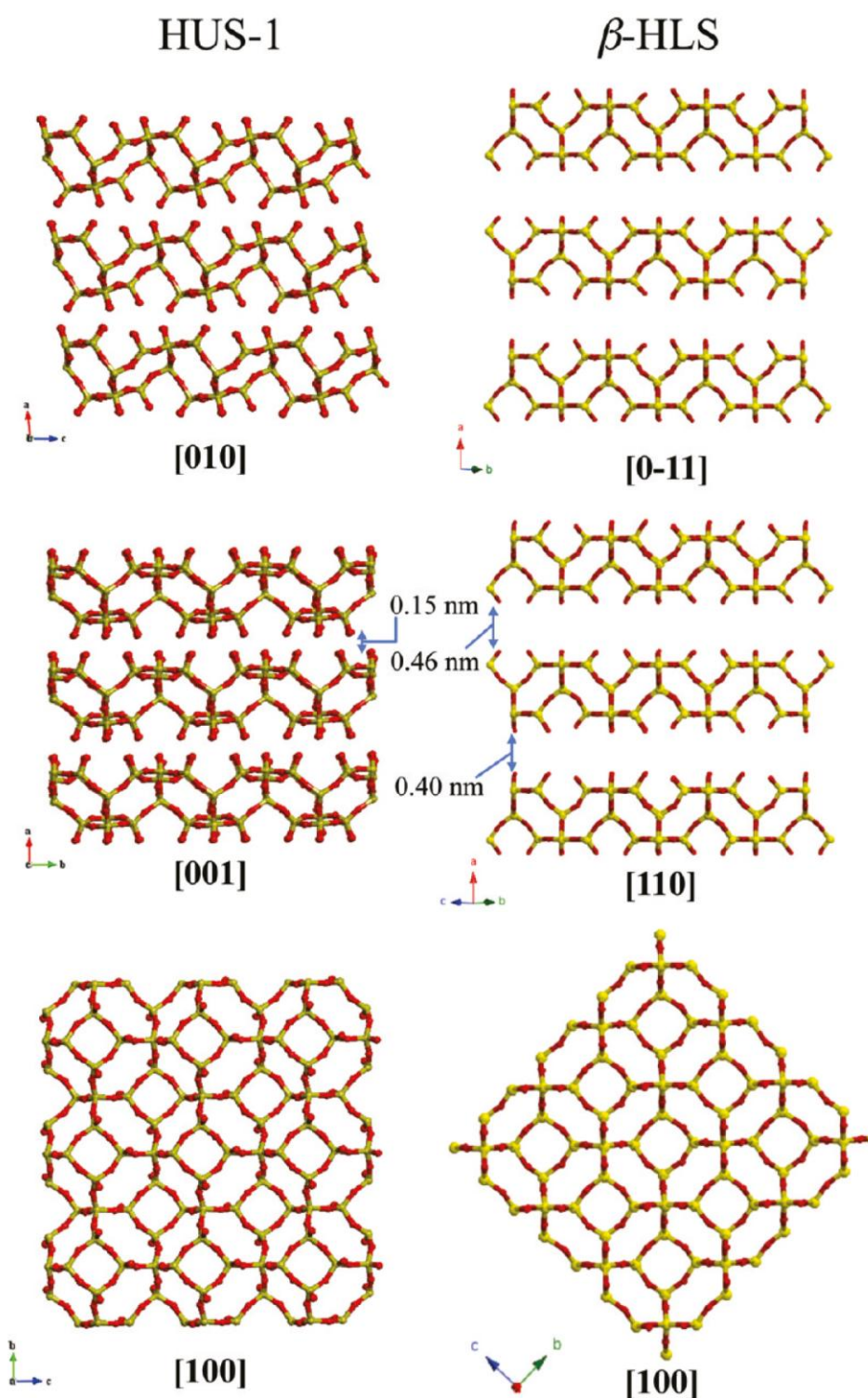


Fig. 7-11 Schematic representations of the framework structures for HUS-1 and β -HLS. The upper and middle figures show stacking sequences of silicate layers in HUS-1 and β -HLS, respectively, while the lower figure illustrates the identical framework topology of both layers.

4. Conclusions

We synthesized a new layered silicate HUS-1, whose chemical composition is $\text{Si}_{10}\text{O}_{24}\text{H}_6 \cdot 2(\text{TMA})$, based on the interzeolite conversion method. Silica and alumina sources were prepared by decomposition of FAU and *BEA zeolites under hydrothermal conditions, but Al atoms were hardly included in the HUS-1 framework. The crystal structure of HUS-1, with a halved SOD framework topology, is very similar to that of β -HLS though the topology was deformed in comparison with that of β -HLS. The TMA molecule in the hemispherical sodalite cage acted as an SDA. The interlayer distances between neighboring silicate layers are very short because neighboring layers are bridged by hydrogen bonding between terminal silanols. The presence of hydrogen bonding was clearly revealed by ^1H MAS NMR spectra and EDD images resulting from MPF analysis. The hydrogen bonds stabilize the whole crystal structure to form small pseudocages like sodalite cage.

References

- [1] T. Kimura, T. Kamata, M. Fuziwara, Y. Takano, M. Kaneda, Y. Sakamoto, O. Terasaki, Y. Sugahara, K. Kuroda. *Angew. Chem., Int. Ed.* 39 (2000) 3855.
- [2] S. Inagaki, Y. Fukushima, K. Kuroda. *J. Chem. Soc., Chem. Commun.* 680 (1993).
- [3] Y. Wang, Y. Shang, J. Wu, J. Zhu, Y. Yang, C. Meng. *J. Chem. Technol. Biotechnol.* 85 (2010) 279.
- [4] F. Kooli, Y. Kiyozumi, Y. Rives, V. Mizukami, *F. Langmuir* 2002, 18, 4103.
- [5] T. Ikeda, Y. Akiyama, Y. Oumi, A. Kawai, F. Mizukami. *Angew. Chem., Int. Ed.* 43(2004) 4892.
- [6] S. Zanardi, A. Alberti, G. Cruciani, A. Corma, V. Fornes, M. Brunelli. *Angew. Chem., Int. Ed.* 43 (2004) 4933.
- [7] B. Marler, M. Cambor, H. Gies. *Microporous Mesoporous Mater.* 90 (2000) 87.
- [8] B. Marler, N. Str€oter, H. Gies. *Microporous Mesoporous Mater.* 83 (2005) 201.
- [9] Y. Oumi, T. Takeoka, T. Ikeda, T. Yokoyama, T. Sano. *New J. Chem.* 31 (2007) 593.
- [10] T. Ikeda, Y. Oumi, T. Takeoka, T. Yokoyama, T. Sano, T. Hanaoka. *Microporous Mesoporous Mater.* 110 (2008) 488.
- [11] Y. Wang, B. Marler, H. Gies. *M€uller, U. Chem. Mater.* 17 (2005) 43.
- [12] T. Ikeda, S. Kayamori, F. Mizukami. *J. Mater. Chem.* 19 (2009) 5518.
- [13] J. Song, H. Gies. *Stud. Surf. Sci. Catal.* 154A (2004) 295.
- [14] B. Marler, Y. Wang, H. Song, H. Gies. *Abstracts of Papers, 15th International Zeolite Conference, 2007 Beijing, China, August 12-17 (2007) p 599.*
- [15] A. Burton, R.J. Accardi, R.F. Lobo, M. Falcioni, M.W. Deem. *Chem. Mater.* 12 (2000) 2936.

- [16]D.L. Dorset, G.J. Kennedy. *J. Phys. Chem. B* 108 (2004) 15216.
- [17]L.M. Knight, M.A. Miller, S.C. Koster, M.G. Gatter, A.I. Benin, R.R. Willis, G.J. Lewis, R.W. Broach. *Stud. Surf. Sci. Catal.* 170A (2007) 338.
- [18]A.J. Blake, K.R. Franklin, B.M. Lowe. *J. Chem. Soc., Dalton Trans.* (1988) 2513.
- [19]S. Vortmann, J. Rius, S. Siegmann., H. Gies. *J. Phys. Chem. B* 101 (1997) 1292.
- [20]Y.X. Wang, H. Gies, J.H. Lin. *Chem. Mater.* 19 (2007) 4181.
- [21]T. Ikeda, Y. Akiyama, F. Izumi, Y. Kiyozumi, F. Mizukami, T. Kodaira, *Chem. Mater.* 13 (2001) 1286.
- [22] U. Oberhagemann, P. Bayat, B. Marler, H. Gies, J. Rius. *Angew. Chem., Int. Ed. Engl.* 35 (1996) 2869.
- [23]L. Masséger, C. Baerlocher, L.B. McCusker, M.A. Zwijnenburg *Microporous Mesoporous Mater.* 105 (2007) 75.
- [24]L.Z. Pauling. *Kristallogr.* 74 (1930) 213.
- [25]Z. Li, B. Marler, H. Gies. *Chem. Mater.* 20 (2008) 1896.
- [26]T. Moteki, W. Chaikittisilp, A. Shimojima, T. Okubo. *J. Am. Chem. Soc.* 130 (2008) 15780.
- [27]H. Jon, H. Sasaki, T. Inoue, M. Itakura, S. Takahashi, Y. Oumi, T. Sano. *Stud. Surf. Sci. Catal.* 174 (2008) 229.
- [28]M. Itakura, T. Inoue, A. Takahashi, T. Fujitani, Y. Oumi, T. Sano. *Chem. Lett.* 37 (2008) 908.
- [29]H. Jon, N. Ikawa, Y. Oumi, T. Sano. *Chem. Mater.* 20 (2008) 4135.
- [30]H. Jon, T. Takahashi, H. Sasaki, Y. Oumi, T. Sano. *Microporous Mesoporous Mater.* 113 (2008) 56.
- [31]T. Inoue, M. Itakura, H. Jon, Y. Oumi, A. Takahashi, T. Fujitani, T. Sano.

- Microporous Mesoporous Mater. 122 (2008) 149.
- [32]H. Sasaki, H. Jon, M. Itakura, T. Inoue, T. Ikeda, Y. Oumi, T. Sano. *J. Porous Mater.* 16 (2009) 465.
- [33]M. Itakura, Y. Oumi, M. Sadakane, T. Sano. *Mater. Res. Bull.* 45 (2010) 646.
- [34]S. Arimoto, M. Sugimura, H. Kageyama, T. Torimoto, S. Kuwabata. *Electrochim. Acta* 53 (2008) 6228.
- [35]A. Boultif, D. Lou er. *J. Appl. Crystallogr.* 24 (1991) 987.
- [36]A. Altomare, M. Camalli, C. Cuocci, C. Giacobozzo, A. Moliterni, R. Rizzi. *J. Appl. Crystallogr.* 42 (2009) 1197.
- [37]A. Le Bail, H. Duroy, J.L. Fourquet. *Mater. Res. Bull.* 23 (1988) 447.
- [38]G. Oszl_anyi, A. S uto. *Acta Crystallogr., Sect. A* 60 (2004) 134.
- [39]L. Palatinus, G. Chapuis. *J. Appl. Crystallogr.* 40 (2007) 786.
- [40]F. Izumi, K. Momma. *Solid State Phenom.* 130 (2007) 15.
- [41]T. Ohta, F. Izumi, K. Oikawa, T. Kamiyama. *Phys. B* 234-236 (1997) 1093.
- [42]F. Izumi, K. Momma. *J. Vac. Soc. Jpn.* 53 (2010) 706-712.
- [43]K. Momma, F. Izumi. *J. Appl. Crystallogr.* 41 (2008) 653.
- [44]X. Xue, M. Kanzaki. *J. Phys. Chem. B* 111 (2007) 13156.
- [45]V. Favre-Nicolin, R. Cerny. *J. Appl. Crystallogr.* 35 (2002) 734.
- [46] International Tables for Crystallography, 5th ed. Hahn, Th., Ed. Springer: Dordrecht, The Netherlands, Vol. A (2005) pp 35-38.
- [47]S. Inagaki, T. Yokoi, Y. Kubota, T. Tatsumi. *Chem. Commun.* 5188 (2007).
- [48]P. Wu, J. Ruan, L. Wang, L. Wu, Y. Wang, Y. Liu, W. Fan, M. He, O. Terasaki, T. Tatsumi. *J. Am. Chem. Soc.* 130 (2008) 8178.
- [49]J. Ruan, P. Wu, B. Slater, Z. Zhao, L. Wu, O. Terasaki. *Chem. Mater.* 21 (2009)

2904.

[50]T. Ikeda, S. Kayamori, Y. Oumi, F. Mizukami. *J. Phys. Chem. C* 114 (2010) 3466.

Chapter 8

An efficient way to synthesize Hiroshima University Silicate-1 (HUS-1) and the selective adsorption property of Ni²⁺ from seawater

1. Introduction

Concentration of ions on solid surface from the environment is a topic of a wide range of scientific and practical viewpoints for such purposes as the removal of toxic metals and the collection of noble elements. Adsorption processes are promising strategies for the objective, therefore, searching and designing adsorbents for target ions have actively been conducted. Layered materials are promising adsorbents due to advantages such as chemical and thermal stabilities if compared with organic counterparts, and material diversity[1,2]. There have been several papers on ion-exchange selectivity on layered materials. For example, anions with higher charge and smaller size are preferentially adsorbed on layered double hydroxides[3]. Recently, the concentration of NO₃⁻ on a Ni/Fe layered double hydroxide from seawater has been reported[4]. As for cations, selective adsorption of such elements as heavy metals and radioactive ions on ion exchangeable layered materials such as smectite clays[5], synthetic micas[6,7], layered metal phosphates[8,9], and layered transition-metal oxides[10–12] has been reported to date. Ide et al. have also found that a layered alkali silicate, magadiite, effectively concentrates Zn²⁺ from seawater[13]. A wide variety of layered materials are available, therefore it is still worth conducting study of layered materials for environmental

purification and collection of noble ions.

Very recently, I have reported the successful synthesis and structural analysis of a new layered silicate, HUS-1 (Hiroshima University Silicate-1, $\text{Si}_{10}\text{O}_{24}\text{H}_8 \cdot 2[(\text{CH}_3)_4\text{N}]$) which is composed of silicate sheets with a halved sodalite cage framework structure and interlayer TMA cation[14,15] (Figure 8-1), an ast-type layered silicate[16]. However, the silicate was synthesized by a complicated procedure, the decomposition of dealuminated FAU and *BEA zeolites with TMA hydroxide and benzyltrimethylammonium hydroxide, respectively, under hydrothermal conditions, followed by hydrothermal mixing of the two obtained gels. This procedure was on the basis of our interzeolite conversion method using decomposed FAU zeolites and various structure-directing agents like TMA, which was useful to synthesize a wide variety of zeolites[17–24]. In the present study, I developed an alternative and efficient way to synthesize HUS-1 only using amorphous silica and TMA which are as a silica source and a structure-directing agent, respectively.

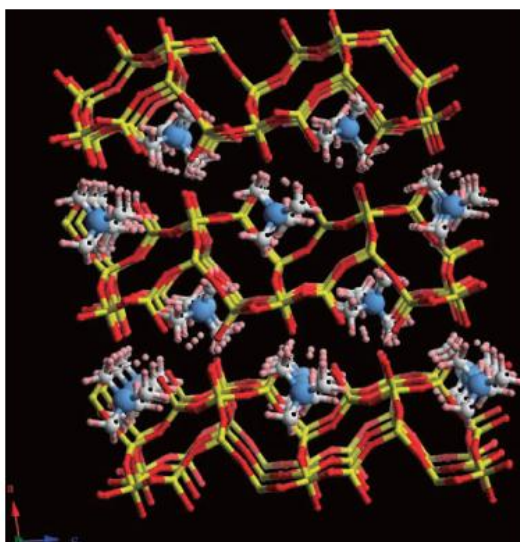


Fig. 8-1 Structure of HUS-1.

In this article, I also report the successful concentration of Ni^{2+} on the obtained HUS-1 from seawater. Nickel was chosen as a target element to be concentrated, because it is widely applied in various industries, is an element of concern for depletion of natural resources, and exists in seawater at the concentration of 0.4 ppb[25]. In addition, nickel ion or nickel oxide particle-supported nanoporous inorganics such as layered titanates and mesoporous silicas have a potential as efficient catalysts for reactions such as selective cyclohexane epoxidation and ethane to propene reaction [26–28]. I have investigated the concentration of Ni^{2+} from seawater on various cation exchangeable materials such as HUS-1, a layered alkali silicate (Na magadiite), a layered clay (Na montmorillonite), and a zeolite (Na mordenite), finding that selective and effective adsorption of Ni^{2+} was attained only on HUS-1.

2. Experimental

2.1 Synthesis of HUS-1

Amorphous silica Nipsil ($\text{SiO}_2 = 88 \text{ wt}\%$, $\text{Al}_2\text{O}_3 = 0.27 \text{ wt}\%$, Nippon Silica Ind., Japan), tetramethyl ammonium hydroxide (TMA, 20 wt%, Aldrich), sodium hydroxide (>99%, High Purity Chemical Inc., Japan), and distilled water were mixed at various $\text{H}_2\text{O}:\text{TMA}:\text{NaOH}:\text{SiO}_2$ molar ratios. The mixture was sealed in a Teflon-lined stainless steel vessel and treated hydrothermally at temperature ranging from 100 to 170 °C for 3–21 days. The product was separated by centrifugation (3500 rpm, 10 min) and washed with a dilute aqueous solution of NaOH (pH 9.0) and dried at 40 °C for 2 days. The synthesis of HUS-1 in the presence of the seed crystal was also conducted.

2.2 Preparation of other adsorbents

Magadiite was synthesized by a reported method [29]. High-purity sodium silicate (SiO_2 , 21.1 wt%; Na_2O , 6.57 wt%, Nihon Chemical Ind. Co.), silica gel (special grade, Wako Chemicals, Japan), NaOH, and distilled water were mixed at the molar ratio of $\text{SiO}_2:\text{NaOH}:\text{H}_2\text{O} = 1:0.23:18.5$. The mixture was sealed in a Teflon-lined stainless steel vessel and treated hydrothermally at 150 °C for 2 days. The product was separated by centrifugation (3500 rpm, 10 min) and washed with a dilute aqueous solution of NaOH (pH 9.0) and dried at 40 °C for 2 days. Na montmorillonite (Kunipia F) and Na mordenite (HSZ642NAA, $\text{SiO}_2/\text{Al}_2\text{O}_3 = 18$) were obtained from Kunimine Ind. Co., Japan and Tosoh Co., Japan, respectively.

2.3 Preparation of seawater-mimicking mixed electrolyte Solution

A mixed electrolyte solution (pH 7.3) was prepared using NaCl (99.5%, Kanto Chemical Co., Inc., Japan), KCl (99.5%, Wako), CaSO_4 (98%, Wako), MgCl_2 (Nacalai Tesque, Inc., Japan), and MgSO_4 (99.5%, Wako). The composition was on the basis of natural seawater [30].

2.4 Adsorption tests

Adsorbent (40 mg) was mixed with the mixed electrolyte solution (40 mL) containing the tuned amount of $\text{Ni}(\text{NO}_3)_2 \cdot 6\text{H}_2\text{O}$ (99.9%, Wako) and the mixture was shaken for 3 days at room temperature. After the adsorbent was separated by filtration, the concentration of the remaining Ni ions in the supernatant was determined by inductively coupled plasma-optical emission spectroscopy (ICP-OES, CAP6000 series (Thermo Scientific)). The adsorption isotherms were plotted using the Ni^{2+} concentration as

equilibrium concentration. In order to estimate the amount of the remaining TMA in HUS-1, Ni-adsorbed products were washed with water and then measured by thermogravimetric-differential thermal analyses (TG-DTA).

2.5 Characterization

X-ray diffraction patterns of the solid products were collected using a powder X-ray diffractometer (Bruker D8 Advance) with graphite monochromatized $\text{CuK}\alpha$ radiation at 40 kV and 30 mA. The crystal morphology was observed by scanning electron microscopy (SEM, Hitachi S-4800) and elemental mapping of products after adsorption tests was conducted by SEM and energy-dispersive X-ray analysis. TG-DTA curves were collected using a SSC/5200 apparatus (Seiko Instruments). The sample was heated from room temperature to 800 °C in an air flow (50 mL min^{-1}) at a rate of $10 \text{ }^\circ\text{C min}^{-1}$. ^{13}C CP/MAS NMR and ^{29}Si MAS NMR spectra were recorded at 600MHz on a Varian 600 spectrometer using a 6 mm-diameter zirconia rotor spinning at 5 kHz. The spectra were acquired using $4.8 \mu\text{s}$ 90° pulse length, 50 s recycle delay, and 1000 scans for ^{13}C CP/MAS NMR, and $6.7 \mu\text{s}$ 90° pulse length, 100 s recycle delay, and 500 scans for ^{29}Si MAS NMR, respectively. ^1H MAS NMR spectrum was also measured using 3.2 mm-diameter zirconia rotor with a spinning at 15 kHz, $4.2 \mu\text{s}$ 90° pulse length, 5 s recycle delay. The ^1H , ^{13}C , and ^{29}Si chemical shifts were referenced to adamantane, hexamethylbenzene, and 3-(trimethylsilyl)propionic-2,2,3,3- d_4 acid sodium salt, respectively.

3. Results and discussion

3.1 Synthesis of HUS-1

HUS-1 has a framework topology similar to that of sodalite zeolites, which is described in our earlier work (Figure 8-1)[14]. Recent successes on the synthesis of new sodalite-like layered silicates other than HUS-1, using TMA as a structure-directing agent and amorphous silica as a silica source at higher $\text{H}_2\text{O}/\text{SiO}_2$ ratio (16–48)[31–34] as well as the interzeolite conversion at lower $\text{H}_2\text{O}/\text{SiO}_2$ ratio (5–10)[17–24], motivated me to synthesize HUS-1 using TMA and amorphous silica at lower $\text{H}_2\text{O}/\text{SiO}_2$ ratio. Table 8-1 presents conditions used for synthesizing HUS-1. As it is well recognized that adding seed crystal of the desired zeolite phase to the starting synthesis gel can enhance the crystallization rate[30,35], I also tried to synthesize HUS-1 in the presence of seed crystals. As expected, when the reaction was conducted at relatively low $\text{H}_2\text{O}/\text{SiO}_2$ ratio (5.5), HUS-1 formed as a single crystalline compound (Figure 8-2). It became clear that HUS-1 could be synthesized only using amorphous silica and TMA as silica source and structure-directing agent, respectively, for a wide range of NaOH/SiO_2 (0.2–0.6) and $\text{TMAOH}/\text{SiO}_2$ (0.2–0.8) ratios at a $\text{H}_2\text{O}/\text{SiO}_2$ ratio of 5.5 and reaction temperature of 140 °C. It was also found that the yield of HUS-1 was increased by adding seeds. This result is worth mentioning as a merit of the present material synthesis, since HUS-1 is originally synthesized through a complicated procedure involving the decomposition of dealuminated FAU and *BEA zeolites with TMA hydroxide and benzyltrimethylammonium hydroxide, respectively, under hydrothermal conditions, followed by hydrothermal mixing of the two gels[14]. The yield and crystallinity (which correlates to the stacking regularity of the silicate sheets) of HUS-1 varied depending on the synthetic conditions (Table 8-1).

Table 8-1 Synthesis Conditions of HUS-1

Entry	Starting synthesis gel			Temp. /°C	Time /day	Yield / % ^{a)}	Relative crystallinity / % ^{b)}	Products
	H ₂ O/SiO ₂	TMAOH/SiO ₂	NaOH/SiO ₂					
1	15.5	0.6	0.2	140	7	trace	28	HUS-1, Unknown
2	10.5	0.6	0.2	140	7	trace	33	HUS-1, Unknown
3	5.5	0.6	0.2	100	7	trace	41	HUS-1, Unknown
4	5.5	0.6	0.2	125	7	57	77	HUS-1
5	5.5	0.6	0.2	140	3	22	80	HUS-1
6	5.5	0.6	0.2	140	3 ^{c)}	30	95	HUS-1
7	5.5	0.6	0	140	7	—	—	RUB-15
8	5.5	0.6	0.2	140	7	24	58	HUS-1
9	5.5	0.6	0.4	140	7	44	71	HUS-1
10	5.5	0.6	0.6	140	7	2	20	HUS-1, Silica-sodalite
11	5.5	0.6	0.8	140	7	—	—	Silica-sodalite
12	5.5	0.2	0.2	140	7	70	41	HUS-1, Amorphous
13	5.5	0.4	0.2	140	7	6	65	HUS-1
14	5.5	0.8	0.2	140	7	100	78	HUS-1
15	5.5	0.8	0.2	140	21	95	73	HUS-1
16	5.5	0.6	0.2	140	21	54	100	HUS-1
17	5.5	0.6	0.2	170	7	60	24	HUS-1, Unknown

a) Based on starting SiO₂ source. b) [Sum of intensities of the three most intense peaks at $2\theta = 9.9$ (basal plane), 19.9 (basal plane), and 23.6° for products]/[Sum of intensities of the three most intense peaks at $2\theta = 9.9$ (basal plane), 19.9 (basal plane), and 23.6° for sample 16] $\times 100$. c) Seed HUS-1 crystal (Entry 16, 3 mass %) was added in the mixture.

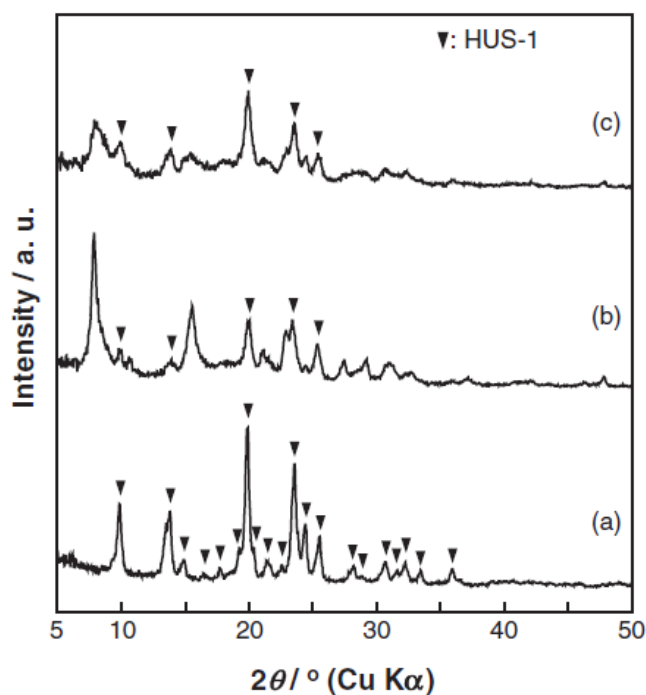


Fig. 8-2 X-ray diffraction patterns of products obtained at TMAOH/SiO₂ ratio of 0.6, NaOH/SiO₂ ratio of 0.2, and 140 °C for 7 days with varied H₂O/SiO₂ ratio; (a) 5.5, (b) 10.5, and (c) 15.5 (Entries 8, 2, and 1 in Table 8-1, respectively).

Spectroscopic studies of the products further confirmed the formation of HUS-1 by the presently developed simple method. Figure 8-3a shows the ^{13}C CP/MAS NMR spectrum of a typical sample (Entry 16). A sharp resonance observed at 57.8 ppm is attributed to a methyl group of the intercalated TMA cation[14]. In the ^{29}Si MAS NMR spectrum of the same product, Q^3 and Q^4 species were clearly observed (Figure 8-3b). Three resonance peaks at ca. -102, -105, and -108 ppm were assigned to the Q^3 structure, whereas a resonance peak at -115 ppm was assigned to the Q^4 structure, indicating that there are crystallographically different 4T atoms within HUS-1 framework structure. As shown in the ^1H MAS NMR spectrum (Figure 8-3c), one strong peak and three weak resonance peaks were observed. The strong peak at 3.4 ppm was assigned to a methyl groups, while the three broad peaks at 6.1, 10.0, and 12.6 ppm were due to $\text{SiO}-\text{H}\cdots\text{OSi}$ hydrogen bonds in the interlayer and intralayer. These NMR results were in good agreements with those of the originally developed HUS-1, showing a characteristic hydrogen bonding between the adjacent silicate sheets in the layered silicate (Figure 8-1). The previous work demonstrated that the nearest atomic distances between neighboring silanol groups were $l(\text{O1}-\text{O3}) = 2.64\text{\AA}$, $l(\text{O1}-\text{O4}) = 2.53\text{\AA}$, and $l(\text{O1}-\text{O7}) = 2.69\text{\AA}$ [14].

The TG curves of the present HUS-1 are shown in Figure 8-4. The mass loss in a temperature range between 200–800 °C, which was due to the oxidative decomposition of TMA and the condensation of the interlayer silanol groups, was identical (25–26 mass%) for all the products synthesized by different conditions.

In the SEM images of the present products, square-plate particles were observed (Figure 8-5). This particle morphology is also characteristic of HUS-1[14]. In the previous study, HUS-1 particles with a size of 24 μm were obtained. For the present

HUS-1, the particle size varied from 0.6 to 8 μm depending on the synthetic conditions.

All the results described above indicate that I successfully synthesize HUS-1 with identical structure and composition ($\text{Si}_{10}\text{O}_{24}\text{H}_8 \cdot 2[(\text{CH}_3)_4\text{N}]$); on the other hand, the crystallinity and particle size are dependent upon the hydrothermal synthetic conditions.

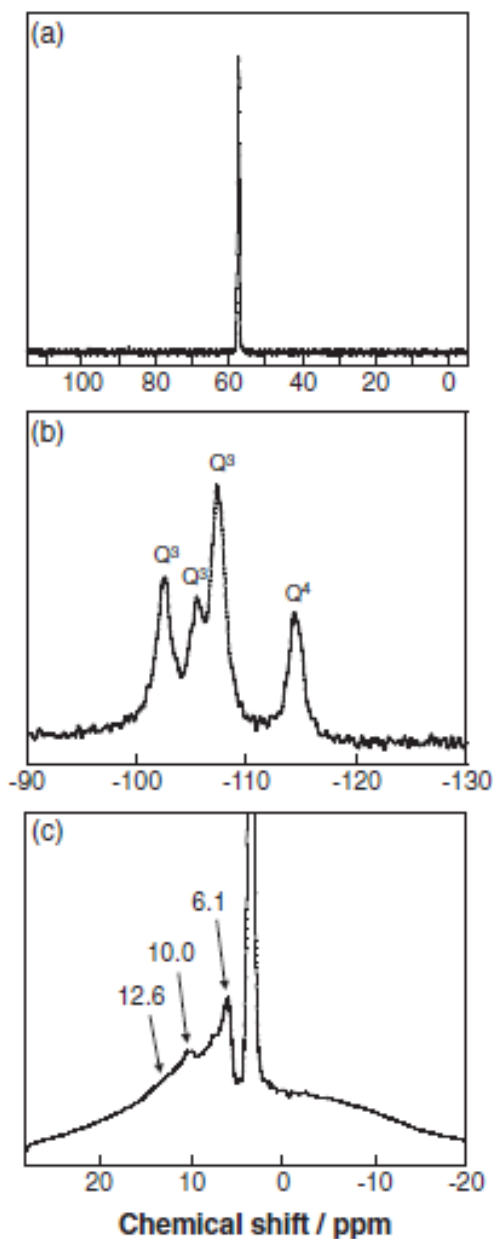


Fig. 8-3 (a) ^{13}C CP/MAS NMR, (b) ^{29}Si MAS NMR, and (c) ^1H MAS NMR spectra of HUS-1 (Entry 16 in Table 1).

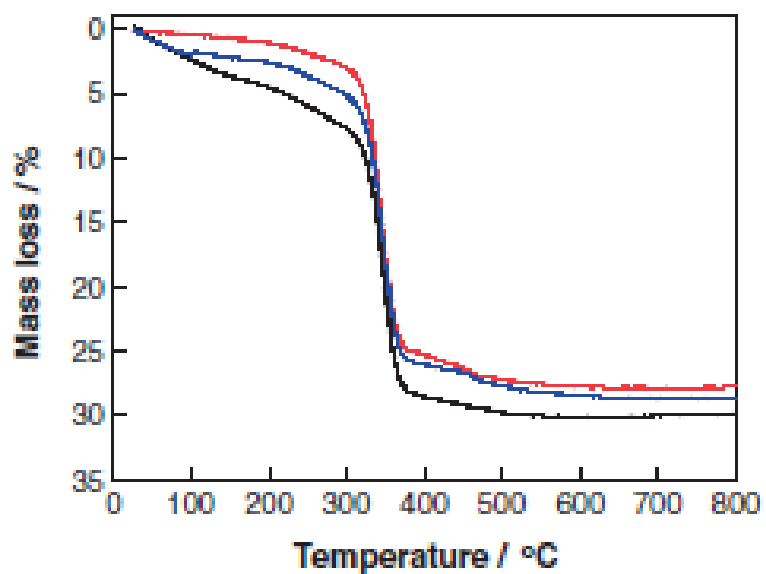


Fig. 8-4 TG curves of HUS-1: (—) Entry 5, (—) Entry 6, and (—) Entry 16 in Table 1.

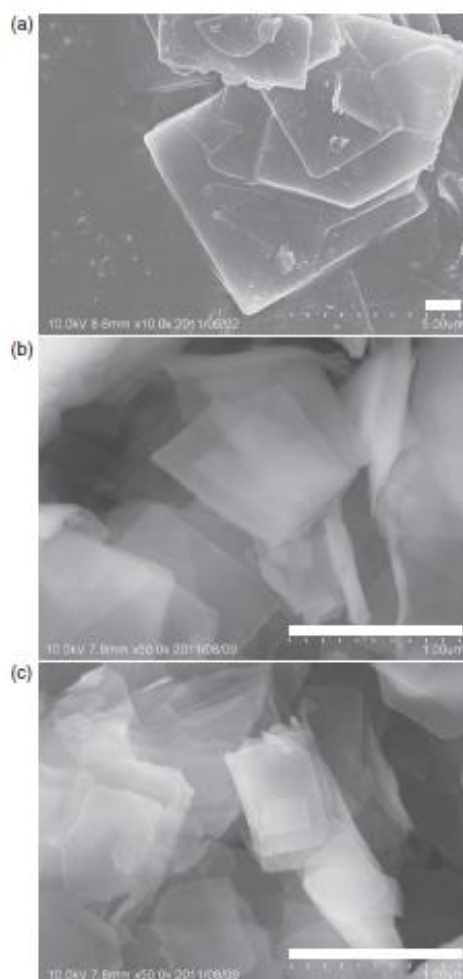


Fig. 8-5 SEM images of HUS-1 prepared with different conditions: (a) Entry 16, (b) Entry 5, and (c) Entry 6 in Table 1. Scale bar: 1 μm.

3.2 Concentration of Ni²⁺

Table 8-2 shows the composition of the mixed electrolyte solution mimicking seawater used in this study. The characteristics of HUS-1 and other adsorbents examined in this study, magadiite, montmorillonite, and mordenite, are also summarized in Table 8-3.

Table 8-2 Compositions of Natural Seawater and Mixed Electrolyte Solution Mimicking Seawater

Constitute	Concentration/ppm	
	Natural ³⁵	Mimic
Cl ⁻	7048	7112
Na ⁺	3960	3934
SO ₄ ²⁻	633	591
Mg ²⁺	315	315
Ca ²⁺	143	119
K ⁺	104	142

Three kinds of HUS-1 with different particle size and crystallinity were used. Figure 7-6 depicts the adsorption isotherm of Ni²⁺ on HUS-1(Entry 5 in Table 8-1) from the mixed electrolyte solution. The isotherm exhibits H-type according to the Giles classification[37], indicating strong interactions between Ni²⁺ and the HUS-1 even in the presence of other cations such as Na⁺, K⁺, Mg²⁺, and Ca²⁺. Similar H-type isotherms were obtained for other HUS-1 and the amount of the adsorbed Ni²⁺ depended on the synthetic conditions (Table 8-3). The amount of the adsorbed Ni²⁺ on HUS-1 was lower than the cation-exchange capacity for divalent cations (1.1 mmol g⁻¹); on the other hand, was in good agreement with that of the de-intercalated TMA cation determined on the basis of the TG curves of the Ni²⁺-adsorbed products, which was washed with water for the removal of metal salts precipitated on the particle outer surface. Therefore, Ni²⁺ is thought to adsorb on HUS-1 from seawater through ion exchange with the interlayer TMA cation.

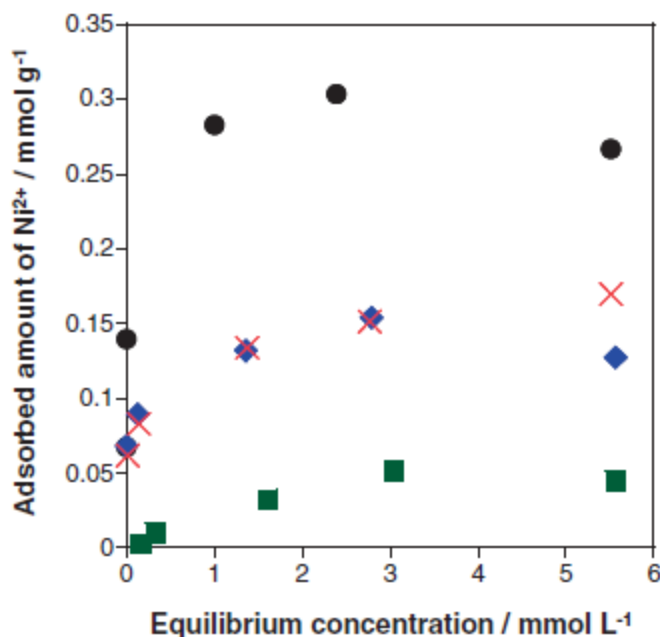


Fig. 8-6 Adsorption isotherms of Ni²⁺ from seawater on (●) HUS-1 (Entry 5 in Table 1), (◆) magadiite, (×) montmorillonite, and (■) mordenite.

Table 8-3 Characteristics and Maximum Amounts of the Adsorbed Ni²⁺ from Seawater of Adsorbents Used in This Study

Adsorbent	Chemical formula	Cation-exchange capacity /mmol g ⁻¹	Maximum amount of adsorbed Ni ²⁺ /mmol g ⁻¹
HUS-1 (Entry 5)	Si ₁₀ O ₂₄ H ₈ ·2[(CH ₃) ₄ N]	2.2 ^{a)}	0.30
HUS-1 (Entry 6)			0.22
HUS-1 (Entry 16)			0.18
Magadiite	Na ₂ Si ₁₄ O ₂₉	2.0 ^{a)}	0.15
Montmorillonite	(Na _{0.53} Ca _{0.09})[(Al _{3.28} Fe _{0.31} Mg _{0.43})(Si _{7.65} Al _{0.35})O ₂₀ (OH) ₄]	1.2	0.15
Mordenite	Na _{4.8} (H ₂ O) _{14.4} [Al _{4.8} Si _{43.2} O ₉₆]	1.5 ^{a)}	0.052

a) Based on the chemical formula.

In order to confirm the adsorption of Ni²⁺ on HUS-1 via cation exchange, [i] HUS-1 (Entry 5 in Table 8-1) was reacted with Ni²⁺ in water, and then [ii] the Ni-adsorbed HUS-1 was treated with an aqueous solution of TMA chloride (regeneration of HUS-1), and finally, [iii] the obtained solid was reacted with aqueous Ni²⁺ again (reuse). From the TG-DTA curves of the solid products and the ICP-OES of the supernatants obtained

at each step, assuming that all the adsorbed Ni species is Ni^{2+} , the composition of each solid product was estimated to be $\text{Si}_{10}\text{O}_{24}\text{H}_8 \cdot 1.8[(\text{CH}_3)_4\text{N}] \cdot 0.10\text{Ni}$, $\text{Si}_{10}\text{O}_{24}\text{H}_8 \cdot 1.9[(\text{CH}_3)_4\text{N}] \cdot 0.05\text{Ni}$, and $\text{Si}_{10}\text{O}_{24}\text{H}_8 \cdot 1.8[(\text{CH}_3)_4\text{N}] \cdot 0.08\text{Ni}$ for step [i], [ii], and [iii], respectively. The original structure of HUS-1 hardly changed during the successive treatments, which was monitored by the XRD and ^{29}Si MAS NMR of the products (data not shown). Moreover, the adsorbed Ni was not eluted with water, but rather quantitatively eluted with aqueous HCl (0.1 mol L^{-1}). These results strongly suggest Ni^{2+} adsorb on HUS-1 reversibly via ion-exchange reaction, rather than via precipitation as salts like $\text{Ni}(\text{OH})_2$. The elemental mapping and the XRD patterns of the Ni^{2+} -adsorbed HUS-1 (Entry 5 in Table 8-1) further supported the replacement of the interlayer TMA cation with Ni^{2+} . In Figure 8-7, Ni is not concentrated on the edge of a particle but is distributed entirely within a particle. The intensity of the diffraction peaks

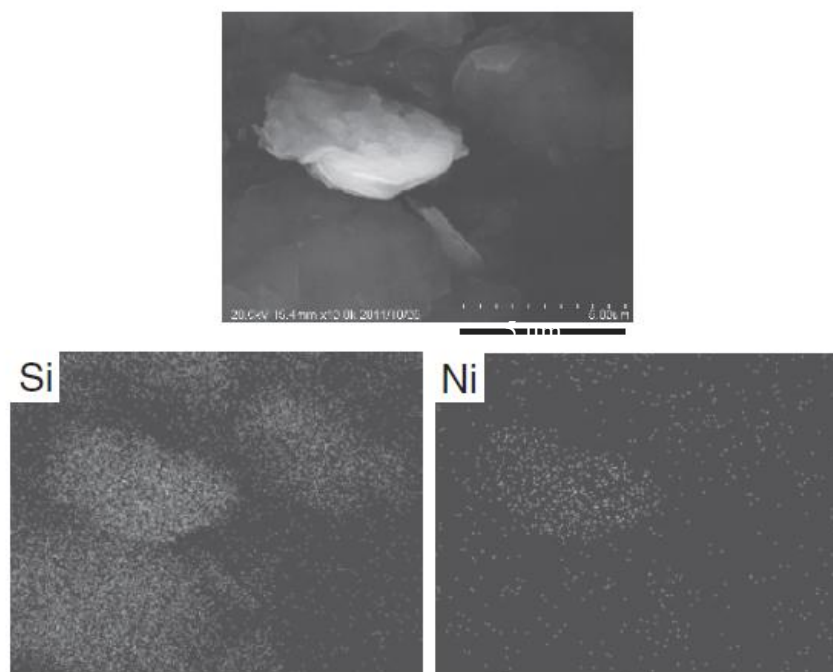


Fig. 8-7 SEM image and the corresponding elemental mapping of HUS-1 (Entry 5 in Table 1) adsorbed with Ni^{2+} from seawater. of HUS-1 lowered upon the adsorption of Ni^{2+} as shown in Figure 8-8. These results

implied the intercalation of Ni^{2+} in the interlayer space of HUS-1. The amount (0.30mmol g^{-1} (0.25 groups per $\text{Si}_{10}\text{O}_{24}\text{H}_8$ unit cell)) of the adsorbed Ni^{2+} on HUS-1 (Entry 5 in Table 8-1) from seawater was much larger than that (0.13mmol g^{-1} (0.10 groups per $\text{Si}_{10}\text{O}_{24}\text{H}_8$ unit cell)) from water. The reason for the result is not clear at present. The pH of seawater (7.8 and 6.5 before and after the reaction, respectively) was higher than that of aqueous $\text{Ni}(\text{NO}_3)_2$ solution (5.1 and 5.5 before and after the reaction, respectively), so that we cannot rule out the possibility of partial precipitation of Ni from seawater on HUS-1.

Ni^{2+} was not replaced by the interlayer TMA cation quantitatively even after repeated reactions (Table 8-3 and Figures 8-8a–8d). When HUS-1 was treated with 1.0 molL^{-1} of aqueous HCl, the original structure collapsed accompanied by the removal of almost all the TMA, which was revealed by the XRD pattern (Figure 8-8e), ^{29}Si MAS NMR spectrum (data not shown), and TG-DTA curves (data not shown) of the product.

Judging from

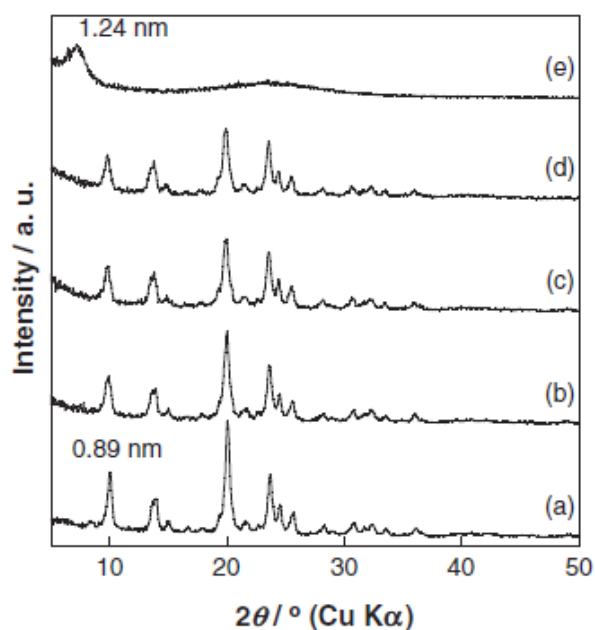


Fig. 8-8 XRD patterns of HUS-1 (Entry 5 in Table 1) (a) before and after the reaction with Ni^{2+} in water for (b) 1, (c) 2, and (d) 3 times, (e) followed by treating with HCl (1mol L^{-1}).

structure, so that it is difficult for Ni^{2+} to be exchanged with TMA^+ quantitatively. As another possible reason for the nonquantitative cation exchange, we consider as follows: The basal spacing of layered materials often varies upon ion exchange. For example, the basal spacing of magadiite decreased from 1.6 to 1.4 nm after the cation exchange of the interlayer Na^+ with Zn^{2+} [13,38] which was explained as a result of the change in the hydration of the interlayer space from the highly hydrophilic Na-form to Zn form[39–41]. In the present case, the basal spacing of HUS-1 hardly changed after the adsorption of Ni^{2+} (Figure 8-8) possibly due to the strong hydrogen-bonding interactions between the adjacent silicate layers[14]. Additionally, a larger amount of Ni^{2+} adsorbed on HUS-1 with smaller particle size and less ordered layer stacking (Table 8-3). Therefore, the narrow interlayer space (0.15–0.26 nm) and strong hydrogen bonding between the adjacent layers of HUS-1[14] prevent the diffusion of Ni^{2+} into the center of the crystal.

The washing of the Ni^{2+} -adsorbed HUS-1 with aqueous HCl (0.1 mol L^{-1}) did not elute the cations other than Ni^{2+} , confirming the selective cation exchange of the interlayer TMA^+ with Ni^{2+} (only slight amount (ca. $0.026 \text{ mmol g}^{-1}$) of Mg^{2+} also adsorbed). A reason for the selectivity was considered as follows: Taking the size (Na^+ , 0.19 nm; K^+ , 0.26 nm; Mg^{2+} , 0.13 nm; Ca^{2+} , 0.20 nm; Ni^{2+} , 0.14 nm)[42] and hydration energy (Na^+ , $114 \text{ kcal g}^{-1} \text{ ion}^{-1}$; K^+ , $94 \text{ kcal g}^{-1} \text{ ion}^{-1}$; Mg^{2+} , $490 \text{ kcal g}^{-1} \text{ ion}^{-1}$; Ca^{2+} , $410 \text{ kcal g}^{-1} \text{ ion}^{-1}$; Ni^{2+} , $516 \text{ kcal g}^{-1} \text{ ion}^{-1}$)[43] of the presently used cations into consideration, only Ni^{2+} was intercalated into narrow interlayer space(0.15–0.26 nm) of HUS-1. The coadsorption of Mg^{2+} , with similar size and hydration energy, supported the hypothesis. Although I cannot rule out an influence of the diameter of hydrated cation on the selective cation exchange, taking into account the facts that the basal spacing of HUS-1

hardly changed after the adsorption of Ni^{2+} and no weight loss due to adsorbed water was observed, the high Ni^{2+} selectivity is probably due to the cation size. Komarneni and Roy have reported the selective adsorption of Cs^+ on α -zirconium phosphate from an aqueous mixture of Na^+ or Ca^{2+} , which was explained by that less hydrated Cs^+ being preferentially intercalated in the narrow interlayer space (0.29 nm) of the phosphate than the more hydrated Na^+ and Ca^{2+} [6].

It should be noted here that the other adsorbents, magadiite, montmorillonite, and mordenite did not concentrate Ni^{2+} from seawater more efficiently than HUS-1. Moreover, the maximum amount (ca. 0.3mmol g^{-1}) of the adsorbed Ni^{2+} on HUS-1 from seawater was comparable to those (ca. 0.4mmol g^{-1}) on a synthetic hydrous manganese dioxide from seawater [44] and on a synthetic hexagonal birnessite from an aqueous solution of NaNO_3 (pH 7) [45]. These facts show the merit of HUS-1 as an adsorbent for collecting Ni^{2+} from seawater and motivate me to investigate Ni^{2+} - or NiO-supported HUS-1 as molecular sievelike catalysts [26–28].

4. Conclusions

I have developed an alternative and efficient way to synthesize HUS-1 by hydrothermal treatment of the starting gel composed of amorphous silica, TMA hydroxide, NaOH, and water. In this synthetic procedure, by changing reaction time (3, 7, and 21 days) and NaOH/ SiO_2 (0.2–0.6) and TMA/ SiO_2 (0.2–0.8) ratios, in the absence or the presence of the seed crystal, HUS-1 with identical structure and composition ($\text{Si}_{10}\text{O}_{24}\text{H}_8 \cdot 2[(\text{CH}_3)_4\text{N}]$), and different particle size and crystallinity successfully formed at 140 °C. The resulting HUS-1 selectively adsorbed Ni^{2+} from a mixed electrolyte solution mimicking seawater by the ion exchange with the interlayer

TMA cation. The maximum amount of the adsorbed Ni^{2+} on HUS-1 varied depending on the synthetic conditions and attained up to 0.3 mmol g^{-1} (0.25 groups per a $\text{Si}_{10}\text{O}_{24}\text{H}_8$ unit cell). The efficient concentration of Ni^{2+} was not attained on other adsorbents, Na magadiite, Na montmorillonite, and Na mordenite.

References

- [1] Handbook of Layered Materials, ed. by S. M. Auerbach, K. A. Carrado, P. K. Dutta, Marcel Dekker, New York, 2004.
- [2] A. Clearfield, Chem. Rev. 88 (1988) 125.
- [3] S. Miyata, Clays Clay Miner. 31 (1983) 305.
- [4] S. Tezuka, R. Chitrakar, A. Sonoda, K. Ooi, T. Tomida, Adsorption 11 (2005) 751.
- [5] C. P. Straub, R. J. Morton, O. R. Placak, J. - Am. Water Works Assoc. 43 (1951) 773.
- [6] W. J. Paulus, S. Komarneni, R. Roy, Nature 357 (1992) 571.
- [7] T. Kodama, S. Komarneni, J. Mater. Chem. 9 (1999) 533.
- [8] S. Komarneni, R. Roy, Nature 299 (1982) 707.
- [9] N. Suzuki, M. Igarashi, H. Suzuki, M. Itoh, Y. Komatsu, Y. Kanzaki, Bull. Chem. Soc. Jpn. 77 (2004) 1829.
- [10] Y. Komatsu, Y. Fujiki, Chem. Lett. 1525 (1980).
- [11] T. Sasaki, Y. Komatsu, Y. Fujiki, Sep. Sci. Technol. 18 (1983) 49.
- [12] D. Yang, Z. Zheng, H. Liu, H. Zhu, X. Ke, Y. Xu, D. Wu, Y. Sun, J. Phys. Chem. C 112 (2008) 16275.
- [13] Y. Ide, N. Ochi, M. Ogawa, Angew. Chem., Int. Ed. 50 (2011) 654.
- [14] T. Ikeda, Y. Oumi, K. Honda, T. Sano, K. Momma, F. Izumi, Inorg. Chem. 50 (2011) 2294.
- [15] Y. Ide, M. Torii, N. Tsunoji, M. Sadakane, T. Sano, Chem. Commun. 48 (2012) 7073.
- [16] B. Marler, H. Gies, Eur. J. Mineral. 24, (2012) 405.
- [17] H. Jon, K. Nakahata, B. Lu, Y. Oumi, T. Sano, Microporous Mesoporous Mater. 96 (2006) 72.

- [18] H. Jon, S. Takahasni, H. Sasaki, Y. Oumi, T. Sano, *Microporous Mesoporous Mater.* 113 (2008) 56.
- [19] M. Itakura, T. Inoue, A. Takahashi, T. Fujitani, Y. Oumi, T. Sano, *Chem. Lett.* 37 (2008) 908.
- [20] H. Sasaki, H. Jon, M. Itakura, T. Inoue, T. Ikeda, Y. Oumi, T. Sano, *J. Porous Mater.* 16 (2009) 465.
- [21] T. Inoue, M. Itakura, H. Jon, Y. Oumi, A. Takahashi, T. Fujitani, T. Sano, *Microporous Mesoporous Mater.* 122 (2009) 149.
- [22] M. Itakura, Y. Oumi, M. Sadakane, T. Sano, *Mater. Res. Bull.* 45 (2010) 646.
- [23] S. Shibata, M. Itakura, Y. Ide, M. Sadakane, T. Sano, *Microporous Mesoporous Mater.* 138 (2011) 32.
- [24] K. Honda, A. Yashiki, M. Itakura, Y. Ide, M. Sadakane, T. Sano, *Microporous Mesoporous Mater.* 142 (2011) 161.
- [25] M. Ezoë, T. Ishita, M. Kinugasa, X. Lai, K. Norisuye, Y. Sohrin, *Geochem. J.* 38 (2004) 535.
- [26] K. Ikeda, Y. Kawamura, T. Yamamoto, M. Iwamoto, *Catal. Commun.* 9 (2008) 106.
- [27] D. Tichit, B. Coq, *CATTECH* 7 (2003) 206.
- [28] T. W. Kim, S.-J. Hwang, S. H. Jhung, J.-S. Chang, H. Park, W. Choi, J.-H. Choy, *Adv. Mater.* 20 (2008) 539.
- [29] K. Kosuge, A. Yamazaki, A. Tsunashima, R. Otsuka, *J. Ceram. Soc. Jpn.* 100, 1992) 326
- [30] A. P. Trujillo, H. V. Thurman, *Essentials of Oceanography*, 6th ed., Prentice Hall, New Jersey, 1999.
- [31] T. Ikeda, Y. Akiyama, F. Izumi, Y. Kiyozumi, F. Mizukami, T. Kodaira, *Chem.*

Mater. 13 (2001) 1286.

[32] Y. Akiyama, T. Ikeda, A. Kawai, Y. Kiyozumi, F. Mizukami, Mater. Chem. Phys. 86 (2004) 112.

[33] A. Kawai, T. Ikeda, Y. Kiyozumi, H. Chiku, F. Mizukami, Mater. Chem. Phys. 99 (2006) 470.

[34] B. Marler, A. Grünewald-Lüke, S. Grabowski, H. Gies, Z. Kristallogr. 227 (2012) 427.

[35] G. T. Kerr, J. Phys. Chem. 70 (1966) 1047.

[36] J. Warzywoda, R. W. Thompson, Zeolites 11 (1991) 577.

[37] C. H. Giles, T. H. MacEwan, S. N. Nakhwa, D. Smith, J. Chem. Soc. 3973 (1960).

[38] H. Muraishi, A. Matsuo, Nendo Kagaku 46 (2007) 61.

[39] N. Mizukami, M. Tsujimura, K. Kuroda, M. Ogawa, Clays Clay Miner. 50 (2002) 799.

[40] M. Ogawa, Y. Takahashi, Clay Sci. 13 (2007) 133.

[41] M. Ogawa, Y. Ide, M. Mizushima, Chem. Commun. 46 (2010) 2241.

[42] L. Pauling, J. Am. Chem. Soc. 49 (1927) 765.

[43] J. D. Bernal, R. H. Fowler, J. Chem. Phys. 1 (1933) 515.

[44] S. B. Kanungo, S. S. Tripathy, Rajeev, J. Colloid Interface Sci. 269 (2004) 1.

[45] C. L. Peacock, D. M. Sherman, Chem. Geol. 238 (2007) 94.

Chapter 9

Summary

Chapter 1, to make the objectives of my doctoral thesis clear, the historical and experimental overview of zeolite chemistry was described.

Next, in chapter 2, I reported applying a seed-assisted method to FAU-*BEA interzeolite conversion with TEOH (tetraethyl ammonium hydroxide) to clarify an influence of seeding on the interzeolite conversion. The crystallization time was shortened from 6 days to 2.5 days by adding seed crystals into the starting mixtures. It was clarified that adding seed crystals was effective on interzeolite conversion. Additionally, I succeeded in shortening the crystallization time to only 2 hours by increasing the amounts of seed crystals. Surprisingly, by adding seed crystals, it was also found that the decomposition/dissolution rate of FAU zeolite became faster than the rate in the case without seed crystals. Namely, the rate of incorporation of locally ordered aluminosilicate species produced by the decomposition/dissolution of starting FAU zeolite to seed crystal surfaces or nuclei was enhanced; consequently, the decomposition/dissolution rate of FAU zeolite increased. This result strongly indicates that it is reasonable to assume that the locally ordered aluminosilicate species produced in the presence of an OSDA other than TEOH contributes to the crystallization of

*BEA zeolite if their chemical structures are suitable for the crystal growth. Therefore, I investigated the influence of OSDAs other than TEAOH on FAU-*BEA interzeolite conversion.

I succeeded in FAU-*BEA interzeolite conversion by using BTMAOH (benzyl trimethyl ammonium hydroxide) in the presence of seed crystals. BTMAOH has already been found to be effective for the synthesis of CHA zeolite from FAU zeolite in the absence of seed crystals. Additionally, I could not obtain a single phase *BEA zeolite in the case of using amorphous material $\text{SiO}_2/\text{Al}(\text{OH})_3$ as a starting material, indicating that the decomposition/dissolution of FAU zeolite can produce more easily suitable locally ordered aluminosilicate species which are suitable for crystal growth of *BEA zeolite. So, next, I investigated the hydrothermal synthesis conditions of OSDA-free FAU-*BEA interzeolite conversions.

I succeeded in interzeolite conversion of FAU zeolite into BEA zeolite in the absence of OSDAs at low temperature (100 °C). To my knowledge, this is the first report on OSDA-free FAU-*BEA interzeolite conversion.

The above results suggest that the zeolite formation process via the interzeolite conversion is more efficient for synthesizing zeolite. The possibility and potential of OSDA-free conversion are shown.

In chapter 3, I tried the seed-assisted FAU-LEV interzeolite conversion in the absence of OSDA.

First, I investigated an influence of alkali metal cations on the interzeolite conversions. The single phase LEV zeolite was obtained in the only case of using NaOH. To my knowledge, this is the first report on hydrothermal synthesis of LEV zeolite from FAU

zeolite in the presence of seed crystals without the use of additional OSDA.

The TEM image of the LEV zeolite obtained showed the presence of smaller crystals within the larger crystals of LEV zeolite, indicating that the LEV zeolite so-obtained has a unique core/shell structure. The smaller crystals are possibly partially decomposed/dissolved seed crystals. The EDX analysis also revealed that the Si/Al ratio of the shell (4.1–4.4) was lower than that of the core (5.5–6.4), i.e., a thin Al-rich shell was wrapped around the core. The Al-rich shell is considered to be fabricated from the aluminosilicate species produced by the decomposition/dissolution of the FAU zeolite. These results strongly suggest that the structural similarity between the starting zeolite (FAU) and the finally crystallized zeolite (LEV) is a crucial factor for the zeolite crystal growth.

In chapter 4, MAZ zeolite was synthesized from FAU zeolite by OSDA-free interzeolite conversion method in the presence of seed crystals. MAZ zeolite has a Composite Building Unit (CBU) composed of mainly 4-MR the same as FAU zeolite.

To further understand the interzeolite conversion process, I investigated the seed-assisted synthesis of MAZ zeolite from various starting zeolites with different CBUs, such as FAU, *BEA, and MFI zeolites, without any additional OSDA. FAU zeolite contains CBU composed of mainly 4-MR, whereas *BEA zeolite includes 4- and 5-MRs, and MFI zeolite is comprised of 5- and 6-MRs.

In the case of using *BEA zeolite as starting material, pure MAZ zeolite was obtained. It was also found that MAZ zeolite could not be obtained from MFI zeolites. However, the yield in the case of using *BEA zeolite was slightly lower if compared to the conversion with FAU zeolite. This difference in yield of MAZ zeolite is probably

attributed to the difference in the amount of available 4-MR CBU. The nitrogen adsorption isotherms of the calcined MAZ zeolite from *BEA zeolite showed type I behavior. The BET surface area and micropore volume were calculated to be $141 \text{ m}^2\text{g}^{-1}$ and $0.11 \text{ cm}^3\text{g}^{-1}$, respectively. These values are considerably smaller than those of MAZ zeolite ($287 \text{ m}^2\text{g}^{-1}$, $0.14 \text{ cm}^3\text{g}^{-1}$) resulting from FAU, indicating a lower crystallinity of MAZ zeolite from *BEA. In the case of MAZ zeolite from amorphous hydrogel, however, nitrogen adsorption hardly occurred. These results strongly indicate that the crystallinity of MAZ zeolite strongly depends on the starting material.

Taking into account the facts that MAZ zeolite contains CBUs composed of 4-MR and that it is not easy to synthesize such zeolites from high-silica aluminosilicate hydrogel (because of the high strain of the 4-MR), it may be concluded that starting zeolites containing 4-MR-based CBUs, such as FAU and *BEA zeolite, are much more effective for the seed-assisted and OSDA-free synthesis of MAZ zeolite. Therefore, it was confirmed that the structural similarity between the starting and the target zeolites is the crucial factor for interzeolite conversion. CBUs composed of a common 4-MR entity are a key for the OSDA-free synthesis of MAZ zeolite. These findings indicate strongly that interzeolite conversion represents an alternative OSDA-free synthesis method of many zeolite types.

In chapter 5, roles of structural similarity between starting and product zeolites in the interzeolite conversion process were investigated.

Interzeolite conversion of FAU zeolites was conducted using only alkaline metal hydroxides. When NaOH was employed as both an alkali source and an inorganic SDA, GIS zeolite was obtained from FAU with a Si/Al ratio of 25. On the other hand, LTL

zeolite was obtained when KOH was used instead of NaOH. For comparison, zeolite synthesis was carried out via conventional hydrothermal synthesis using Cab-o-sil M5 and NaAlO₂ as the initial Si and Al sources, but no zeolite phase was obtained. Except for 6r unit in LTL zeolite, there is no overlap of composite building unit between the starting FAU and product LTL or GIS zeolite. However, a 4MR chain is present in composite building unit of them.

To further confirm the importance of this structural similarity, hydrothermal conversion of FAU zeolite was carried out in the presence of FER seed crystals at various hydrothermal temperatures. There is no structural similarity between FAU and FER zeolites. As expected, pure GIS zeolite was obtained even in the presence of FER seed crystals at 125 °C. However, FAU–FER interzeolite conversion occurred at higher 150 °C. In contrast, in the case of amorphous materials, FER zeolite was obtained regardless of synthesis temperature. These results indicate that structures of the nanoparts produced by decomposition/dissolution of FAU zeolite are strongly dependent on synthesis temperature.

Next, I tried interzeolite conversions of *BEA zeolites in the absence of OSDA. *BEA zeolite is composed 4 and 5 MRs. So, It is expected that the transformation behavior of *BEA zeolite is different from that of FAU zeolite. MOR zeolite was obtained by interzeolite conversion of *BEA zeolite in the condition that GIS zeolite was obtained in the case of using FAU zeolite. This suggests that the starting *BEA zeolite is stable under thus hydrothermal synthesis conditions, and that the formation of MOR zeolite is due to the common composite building unit *mor* (5MRs). I described the OSDA-free syntheses of LEV and MAZ zeolites by interzeolite conversion of FAU zeolite in the presence of seed crystals (Chapters 3, 4). I investigated the effect of adding seed crystals

on the OSDA-free interzeolite conversion of *BEA zeolite. The addition of LEV seed crystals led to the formation of LEV zeolite. However, MOR zeolite coexisted in the product. Conversely, when MAZ seed crystals were used, pure MAZ zeolite was successfully obtained, although the yield was lower than that obtained by interzeolite conversion of FAU zeolite. It appears that compared to *BEA zeolite, FAU zeolite yields many 4MR- containing composite building units via its decomposition. Therefore, the difference in the yield of MAZ zeolite between interzeolite conversion starting with FAU and *BEA zeolites is due to the difference in the amount of available 4MR-based building units.

Therefore, *BEA zeolite is suitable for the synthesis of zeolites containing only 5MR-based composite units. In order to confirm this, interzeolite conversion of *BEA zeolite was carried out in the presence of FER seed crystals, which contained the *fer* composite building unit with 5MRs only. As expected, pure FER zeolite was obtained.

From these results, it was concluded that the structures of nanoparts could be altered through the choice of starting zeolite, implying the possibility of zeolite synthesis by selective assembly of building units with specific structures.

I attempted to synthesize MFI zeolite by interzeolite conversion of *BEA zeolite in the absence of both OSDA and seed crystals, because MFI and *BEA zeolites contain the composite building units composed 4 and 5 MRs. As expected, *BEA–MFI interzeolite conversion was observed when *BEA zeolites with high Si/Al ratios were employed as the starting material. Moreover, it was found that MFI zeolite was not obtained when FAU zeolite and amorphous aluminosilicate gel was used as the starting materials. These results imply that nanoparts produced by the dissolution/decomposition of *BEA zeolites contribute to the nucleation and crystal growth of MFI zeolites.

SEM images and N₂ adsorption-desorption isotherms of the MFI zeolite obtained showed macropores and mesopores. The number of macropores and mesopores decreased with increasing synthesis time.

As mesoporous MFI zeolite with high aluminum content was prepared, I investigated its catalytic potential in the dehydration of lactic acid to acrylic acid. The obtained mesoporous MFI zeolite exhibited good catalytic performance for the dehydration of lactic acid to acrylic acid.

In chapter 6, I attempted hydrothermal conversion of LEV zeolite into CHA zeolite in the absence of both an OSDA and seed crystals. The LEV-CHA transformation proceeds from a more dense zeolite to a less dense one. The pure CHA zeolite was obtained from LEV zeolite as a starting material after 1.5 h of hydrothermal treatment. As the treatment time increased, however, the peaks corresponding to the CHA phase decreased. Finally, the pure ANA zeolite was obtained after 24 h. On the other hand, the formation of CHA zeolite was not observed in the case of using amorphous materials as the starting. In other words, a sequence from starting LEV → an amorphous phase → CHA → ANA was observed. This indicates that the metastable CHA zeolite crystallizes in a kinetically controlled process and that the transformation to most stable ANA zeolite is thermodynamically driven. To the best of my knowledge, this is the first report on the transformation of LEV zeolite into less dense CHA zeolite without the use of both seed crystals and OSDAs.

For comparison, zeolite synthesis was carried out via the conventional hydrothermal synthesis using Cab-o-sil M-5 and NaAlO₂ as the starting Si and Al sources. Only FAU and SOD zeolites were obtained. These results strongly suggest that locally ordered

aluminosilicate species generated by the decomposition/dissolution of the starting LEV zeolite contribute to crystallization of these zeolites.

In chapter 7, I succeeded in synthesizing a new type of a layered silicate, HUS-1 (Hiroshima University Silicate-1), with a halved SOD framework structure. The layered silicate HUS-1 was synthesized hydrothermally using two kinds of zeolites, FAU and *BEA. Two types of primary gels including silica nanosized parts were prepared. One was prepared by decomposition of dealuminated FAU zeolite by hydrothermal treatment with tetramethylammonium hydroxide. The other primary gel was prepared by decomposition of dealuminated *BEA zeolite by hydrothermal treatment with benzyltrimethylammonium hydroxide. The resultant primary gels were mixed well with an aqueous solution of NaOH, and the hydrothermal conversion was conducted. The crystal structure and physicochemical properties of HUS-1 were investigated in detail by field emission scanning electron microscope (FE-SEM), X-ray powder diffractometry (XRD), solid-state magic-angle-spinning nuclear magnetic resonance (MAS NMR) spectroscopy, and thermogravimetric-differential thermal analysis (TG-DTA).

Based on above the characterizations and a structural analyst, the chemical formula of HUS-1 was estimated to be $\text{Si}_{10}\text{O}_{24}\text{H}_6 \cdot 2[(\text{CH}_3)_4\text{N}]$.

In order to better understand the structure of HUS-1, I compared the structure of HUS-1 with β -HLS. The stacking sequence of neighboring layers in HUS-1 is completely different from that in β -HLS. The crystal structure of HUS-1 is formed in an AAAA stacking order whereas that of β -HLS is formed in an ABAB stacking order. Their framework topologies are similar to each other. However, the framework of

HUS-1 is somewhat asymmetric in comparison with the symmetric framework geometry of β -HLS or sodalite.

In chapter 8, to find an efficient way to synthesize HUS-1, the synthesis of HUS-1 was examined by using amorphous silica, sodium hydroxide, and tetramethylammonium hydroxide (TMA). HUS-1 was successfully prepared at a wide range of NaOH/SiO₂ and TMA/SiO₂ ratios. It was also found that the yield of HUS-1 was increased by adding seeds. These results are worth mentioning as merits of the present material synthesis, since HUS-1 is originally synthesized through a complicated procedure (Chapter 7).

Next, I investigated the concentration of Ni²⁺ from seawater on HUS-1. It became clear that there is the strong interaction between Ni²⁺ and the HUS-1 even in the presence of other cations such as Na⁺, K⁺, Mg²⁺, and Ca²⁺, resulting in the selective concentration of Ni²⁺. The selective concentration of Ni²⁺ was not attained on the other adsorbents such as magadiite, montmorillonite, and mordenite.

In this thesis, I investigated the efficient synthesis of zeolites and layer silicates by the interzeolite conversion technique. It was found that a seed-assisted synthesis, OSDA-free synthesis and seed-assisted OSDA-free synthesis have the high potential in the interzeolite conversion. The finding obtained in my study is believed to give a lot of information concerning to zeolite synthesis to research in the zeolite chemistry. Through my study, I succeeded in efficient and low cost syntheses of zeolites and a new layer silicate by the interzeolite conversion method. Obtained information through my study will contribute to more efficient synthesis and syntheses of a novel zeolite or layer silicate.

List of publications

1. K. Honda, A. Yashiki, M. Itakura, Y. Ide, M. Sadakane, T. Sano, –Influence of seeding on FAU-*BEA interzeolite conversions” Micropor. Mesopor. Mater. 142 (2011) 161.
2. A. Yashiki, K. Honda, A. Fujimoto, S. Shibata, Y. Ide, M. Sadakane, T. Sano, –Hydrothermal conversion of FAU zeolite into LEV zeolite in the presence of non-calcined seed crystals” J. Cryst. Growth 325 (2011) 96.
3. T. Ikeda, Y. Oumi, K. Honda, T. Sano, K. Momma, F. Izumi, –Synthesis and crystal structure of a layered silicate HUS-1 with a halved sodalite-cage topology” Inorg. Chem. 50 (2011) 2294.
4. I. Goto, M. Itakura, S. Shibata, K. Honda, Y. Ide, M. Sadakane, T. Sano, –Transformation of LEV-type zeolite into less dense CHA-type zeolite”, Micropor. Mesopor. Mater. 158 (2012) 117.
5. K. Honda, M. Itakura, Y. Matsuura, A. Onda, Y. Ide, M. Sadakane, T. Sano, –Role of structural similarity between starting zeolite and product zeolite in the interzeolite conversion process”, J. Nanosci. Nanotechnol. 13 (2013) 3020.
6. K. Honda, Y. Ide, N. Tsunoji, M. Torii, M. Sadakane, T. Sano, –An efficient way to synthesize Hiroshima University Silicate-1 (HUS-1) and the selective adsorption property of Ni²⁺ from seawater”, Bull. Chem. Soc. Jpn. 87 (2014) 160.
7. K. Honda, A. Yashiki, M. Itakura, M. Sadakane, T. Sano, –Hydrothermal conversion of FAU and *BEA-type zeolites into MAZ-type zeolites in the presence of non-calcined seed crystals”, Micropor. Mesopor. Mater. 196 (2014) 254.

Presentations in international conference

1. K. Honda, A. Yashiki, M. Itakura, Y. Oumi, M. Sadakane, T. Sano, “Interzeolite conversion of FAU into *BEA zeolite by seeding”, 16th International Zeolite Conference joint with the 7th International Mesoporous Materials Symposium, P-060, 2010, July in Italy (Sorrent).
2. A. Yashiki, A. Fujimoto, S. Shibata, K. Honda, M. Itakura, Y. Ide, M. Sadakane, T. Sano, “Hydrothermal conversion of FAU zeolite in the absence of organic structure-directing agents”, 5th International FEZA Conference, SC-P-012-Mon-012, 2011, July in Spain (Valencia).
3. M. Itakura, I. Goto, S. Shibata, K. Honda, Y. Ide, M. Sadakane, T. Sano, “*BEA-MFI and LEV-CHA interzeolite conversion in the absence of organic structure-directing agent and seed crystal”, ZMPC2012 International Symposium on Zeolites and Microporous Crystals, P-018, 2012, July in Hiroshima.

Acknowledgements

I appreciate very much the support from my supervisor Prof. Dr. Tsuneji Sano. If there was not Prof. Sano's tutelage, I could not complete this doctoral thesis. I am deeply grateful to Prof. Sano's taking in me as a doctoral student into laboratory members again. I also express my gratitude for Prof. Sano's advice and forbearance when I was at odds with myself for balancing the academics with jobs.

I do hope Prof. Dr. Sano will give me further guidance and encouragement in the future.

I am extremely grateful to Prof. Masahiro Sadakane and Prof. Yusuke Ide for their valuable comments and suggestions.

I acknowledge Dr. T. Ikeda in National Institute of Advanced Industrial Science and Technology for the structure elucidation of HUS-1 with XRD measurement.

I am thankful for the Dr. Masaya Itakura's help. Dr. Itakura coached me as a senior of doctoral student.

I also gratefully acknowledge Prof. Yasunori Oumi for teaching me laboratorial techniques and work as well as for valuable suggestions.

I am grateful to all of Sano Laboratory's members especially, Dr. S. Sumiya, Dr. N. Ikawa, Mr. T. Inoue, Mr. Miyano, Mr. Ueda, Mr. Goto, Ms. A. Yashiki, Mr. I. Goto, Mr. Nao Tsunoji, Mr. Y. Furumoto, Ms. A. Fujimoto,; and peers as well: Mr. S. Shibata, Mr. Y. Harada, Mr. J. Fujiwara, Mr. K. Ota, and Ms. Y. Kubota for their help, cooperation and contributions to my study.

Hiroshima, March 2015
Koutaro Honda